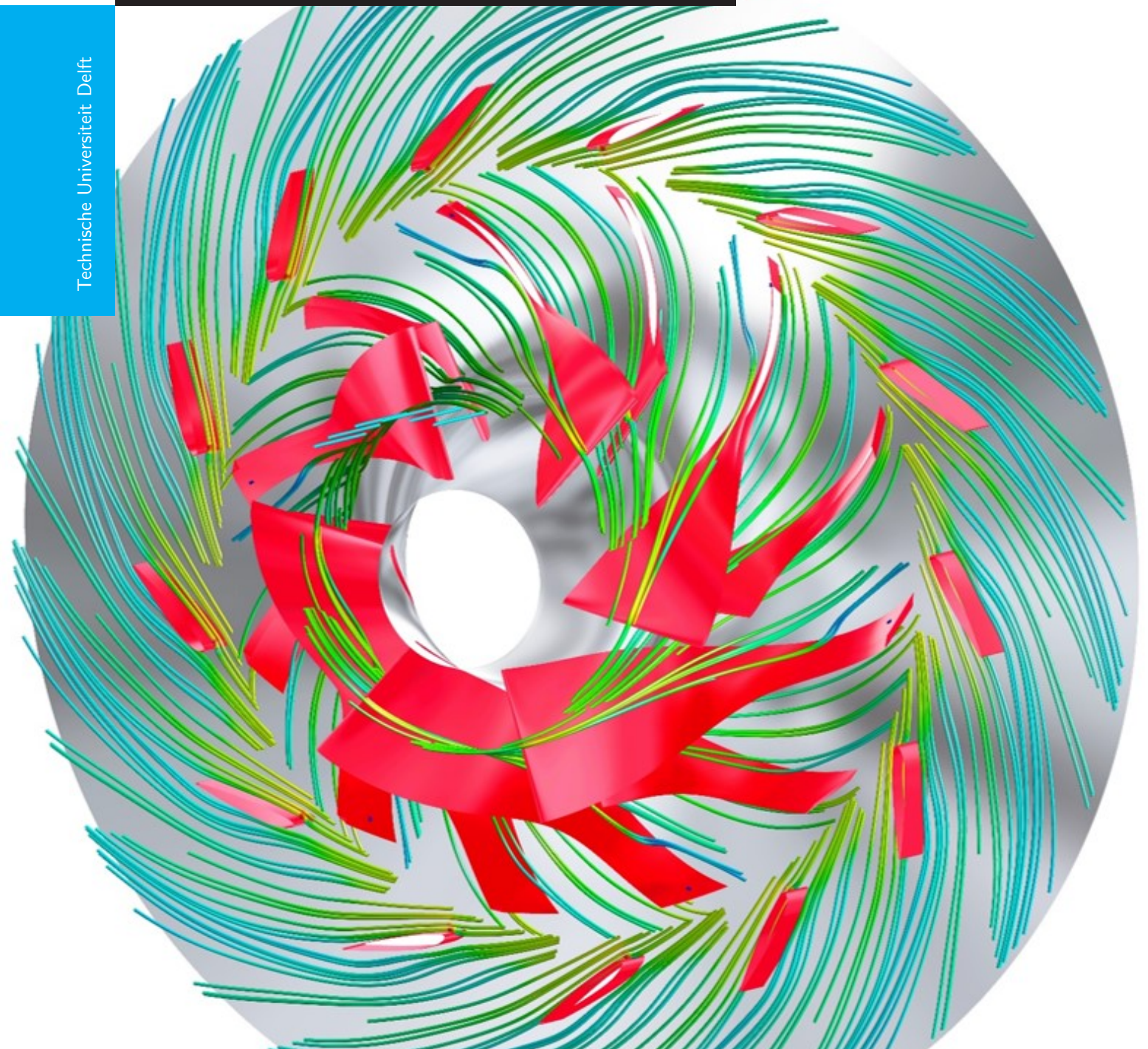


# Design Optimization of The MTT Radial Compressor

A.M. Wasim

Technische Universiteit Delft





# DESIGN OPTIMIZATION OF THE MTT RADIAL COMPRESSOR

by

**A.M. Wasim**

in partial fulfillment of the requirements for the degree of

**Master of Science**  
in Aerospace Engineering

at the Delft University of Technology,  
to be defended publicly on Wednesday July 19, 2017 at 14:00 Hrs.

Supervisor:	Dr. Ir. Matteo Pini,	TU Delft
Thesis committee:	Dr. Ir. Stefan Hickel,	TU Delft
	Dr. Ir. Richard P. Dwight ,	TU Delft
	Ir. Harish Ganesan,	MTT bv

*This thesis is confidential and cannot be made public until April 31, 2022.*

An electronic version of this thesis is available at <http://repository.tudelft.nl/>.



# ABSTRACT

For  $\mu$ CHP applications, micro gas turbines offer many potential advantages in comparison to other conversion technologies due to their compact size and high specific power, low vibration and noise, low maintenance requirements, low emissions and high-grade residual thermal energy.

The recuperated micro gas turbine developed by the Dutch company Micro Turbine Technology B.V. (MTT) utilises off-the-shelf turbocharger impeller for their micro gas turbines to reduce manufacturing cost. However, adopting the turbocharger impeller for micro gas turbine applications mostly results in operating the compressor at off-design conditions, thus reducing its performance.

Improvement in micro gas turbine performance can be achieved by suitable modification of turbocharger technology, especially considering that turbochargers usually employ centrifugal compressor with a vaneless diffuser to minimise production cost and maximise flow range, whereas micro gas turbines require higher efficiency and pressure ratio for a confined operating range. Thus, the main objective of this thesis is to determine a cost effective option to increase the performance of the MTT Compressor.

From the 1D meanline results, it was observed that the incidence at the inlet of the impeller played a significant role in reducing the performance of the MTT compressor. The adoption of turbocharger impeller for MTT compressor was the primary reason for the reduction in MTT compressor performance. However, the losses due to incidence were mitigated at the expense of pressure ratio by providing a positive pre-whirl at impeller inlet. Significant increase in performance of MTT compressor was observed by replacing the vaneless diffuser with a vaned diffuser.

Optimisation of MTT compressor with a vaneless diffuser (OCVLD) was performed to determine the significance of various geometrical parameters on MTT compressor performance. The blade angle at impeller inlet played a major role in reducing the performance of the MTT compressor followed with radius at inducer hub, radius at inducer tip and radius at impeller tip. Further increase in efficiency was observed by performing an optimisation of MTT compressor with a vaned diffuser (OCVD). However, incorporating optimised impeller design is not a cost effective option for MTT as a new compressor scroll has to be designed to accommodate the optimised impeller.

The most cost effective option to increase the performance of the MTT compressor is by incorporating pre-whirl and vaned diffuser with existing turbocharger impeller. It was observed that, approx. 2.2% increase in electrical efficiency for MTT CHP unit can be achieved by incorporating a positive pre-whirl of 25 [deg] and an airfoil shaped vaned diffuser.

*A.M. Wasim  
Delft, June 2017*



# ACKNOWLEDGEMENT

I would like to begin by praising and paying my humble gratitude to the God Almighty. Blessings bestowed upon me by God Almighty are countless.

The research conducted in this MSc. the thesis would not have been possible without the support and guidance of several individuals to whom I owe sincere gratitude and respect.

Firstly, I would like to show my profound gratitude and appreciation to my daily supervisor Dr. Matteo Pini for his guidance throughout the course of this thesis. I greatly appreciate his invaluable insights and support that kept me motivated throughout the thesis. I would like to thank Ir. Marco de Later and Ir. Harish Ganesan from MTT for sharing their thoughts and views throughout the course of this thesis.

I would also like to thank Dr. Stefan Hickel for his support and guidance.

I would like to thank my friends - Raheeba Muhammed, Syed Ibrahim, Saliha Abdul, Vignesh Subbaraj, Jaya Prakash, Karthik, Sandeep, Mohan, Balaji, Noor Nabi and Waqas Hayat. I would also like to thank my team lead at Alstom Ir. Robert Jakic who motivated me to join TU Delft.

Last, but certainly not the least, I would like to thank and show my utmost gratitude to my parents and my sister for their unconditional love, care and support. I dedicate this work to them.

*A.M. Wasim  
Delft, June 2017*



# CONTENTS

<b>List of Figures</b>	<b>ix</b>
<b>List of Tables</b>	<b>xiii</b>
<b>1 Introduction</b>	<b>1</b>
1.1 Energy Trends in Europe	1
1.2 Distributed Energy Generation	2
1.3 Micro CHP System	2
1.4 Micro Gas Turbines for Micro CHP System	5
1.5 Significance of Compressor Performance on MTT Micro CHP Unit	6
1.6 Thesis Objectives	6
1.7 Research Questions	7
1.8 Thesis Outline	7
<b>2 Mean Line Compressor Design</b>	<b>9</b>
2.1 Centrifugal Compressors	9
2.2 Flow Physics Within The Impeller	10
2.3 Flow Physics Across Diffuser	13
2.3.1 Flow Physics Across Vaneless Diffuser	13
2.3.2 Flow Physics Across Vaned Diffuser	14
2.4 Meanline Model for Centrifugal Compressors	15
2.4.1 Meanline Impeller Performance Estimation	15
2.4.2 Meanline Vaneless Diffuser Performance Estimation	21
2.4.3 Meanline Vaned Diffuser Performance Estimation	21
2.5 Overall Stage Predictions	22
2.5.1 Impeller Model	23
2.5.2 Vaneless Diffuser Model	24
2.5.3 Vaned Diffuser Model	25
2.6 Model Verification and Validation	25
<b>3 Mean Line Compressor Performance Optimization</b>	<b>31</b>
3.1 Introduction	31
3.2 Optimisation Problem Statement	32
3.3 Optimization Techniques	34
3.4 Results of The Optimisation	35
<b>4 3D Numerical Assessment of the Compressor with Vaneless Diffuser</b>	<b>39</b>
4.1 Introduction	39
4.2 Modelling of Computational Domain	40
4.2.1 Geometry	40
4.2.2 Grid Generation	40
4.2.3 Numerical Solver	41
4.2.4 Grid Sensitivity Analysis	42
4.3 Results	42
<b>5 Design and 3D Numerical Assessment of compressor with vaned Diffuser</b>	<b>47</b>
5.1 Introduction	47
5.2 Vaned Diffuser	48
5.3 Vaned Diffuser Design Parameters	49
5.4 Numerical Model	51
5.4.1 Geometry	51
5.4.2 Grid Generation	52

---

5.4.3	Solver . . . . .	52
5.5	Results . . . . .	52
5.5.1	Channel Shape Vaned Diffuser . . . . .	52
5.5.2	Airfoil Shaped Vaned Diffuser . . . . .	54
5.5.3	Low Solidity Airfoil Shaped Vaned Diffuser (LSVD) . . . . .	55
5.5.4	Effect of Pre-whirl on MTT Compressor Fluid-Dynamic Performance . . . . .	55
<b>6</b>	<b>Conclusions and Recommendations</b>	<b>57</b>
6.1	Recommendations . . . . .	57
	<b>Bibliography</b>	<b>59</b>

# LIST OF FIGURES

1.1	Gross Inland Energy Consumption in (%) of Total Energy Consumption . . . . .	1
1.2	CO <sub>2</sub> emissions trend between central and distributed energy generation . . . . .	2
1.3	CO <sub>2</sub> emissions trend between central and distributed energy generation . . . . .	3
1.4	Conventional generation versus cogeneration . . . . .	3
1.5	Comparison of overall ( $\eta_o$ ), electrical ( $\eta_{el}$ ) and thermal ( $\eta_{th}$ ) efficiency between cogeneration and conventional generation . . . . .	4
1.6	T-S Diagram of Ideal Brayton Cycle with Recuperation . . . . .	5
1.7	Schematic of MTT Recuperated Micro Gas Turbine CHP System . . . . .	5
1.8	Variation in Compressor Total to Total Efficiency and MTT CHP's Electrical Efficiency with Respect to Compressor Pressure Ratio . . . . .	6
1.9	Variation in Electrical Efficiency with Respect to Compressor Efficiency . . . . .	6
2.1	Main Components of Turbocharger Centrifugal Compressor . . . . .	9
2.2	Enthalpy Rise across a Compressor Stage . . . . .	10
2.3	Flow Physics Across Impeller . . . . .	11
2.4	Velocity Measurements by Eckardt in a Centrifugal Compressor with no Backsweep . . . . .	11
2.5	Impeller Passage with Measurement Planes . . . . .	12
2.6	Influence of Rossby Number on Secondary Flow Motion at Station 5 shown in Figure (2.5) . . . . .	12
2.7	Types of flow over a curved wall and over a rotating system . . . . .	13
2.8	Schematic of compressor with vaneless diffuser . . . . .	13
2.9	Variation of static pressure recovery for a vaneless diffuser . . . . .	13
2.10	Schematic of compressor with vaned diffuser . . . . .	13
2.11	Mean static pressure contours in a vaned diffuser (Normalized by $\rho U_2^2$ ) . . . . .	14
2.12	Overall Stagnation PR for Same Impeller Operating with Vaned Diffuser of Different Axial Width . . . . .	14
2.13	Streamlines pattern in an impeller for inviscid flow: (a) fully attached flow, no backsweep; (b) separated flow, no backsweep; (c) separated flow, with backsweep . . . . .	16
2.14	Meridional View of the Centrifugal Compressor . . . . .	22
2.15	Flow Chart of the Compressor Performance Analysis . . . . .	23
2.16	Performance of MTT Compressor for different RPM varying from 220k up to 240k . . . . .	25
2.17	Velocity Triangles at impeller inlet for 220k and 240k RPM . . . . .	26
2.18	Comparison of the Stage Total-to-Total Pressure Ratio between Experimental and Numerical Results at 220k, 230k, and 240k rpm for Two different Impeller Design with and without Pre-Whirl . . . . .	26
2.19	Comparison of the Stage Exit Total Temperature between Experimental and Numerical Results at 220k, 230k, and 240k rpm for Two different Impeller Design with and without Pre-Whirl . . . . .	27
2.20	Meridional Shape of Impellers used for Experimental and Numerical Analysis . . . . .	27
2.21	Velocity Triangle at Impeller Hub with a Positive and Negative Pre-Whirl of 25 [deg] for MTT Compressor at 240k RPM . . . . .	28
2.22	Variation in Total-to-Total Efficiency of MTT Compressor with Positive Pre-Whirl at 240k RPM . . . . .	28
2.23	H-S Diagram of an Ideal MTT Compressor with and without Pre-Whirl . . . . .	28
2.24	Variation in Total-to-Total Pressure Ratio of MTT Compressor with Positive Pre-Whirl at 240k RPM . . . . .	28
2.25	Variation of $\Pi_{TT}$ by either increasing impeller tip diameter or by decreasing backsweep for MTT compressor with 25 [deg] positive pre-whirl . . . . .	29
2.26	Variation of $\eta_{TT}$ by either increasing impeller tip diameter or by decreasing backsweep for MTT compressor with 25 [deg] positive pre-whirl . . . . .	29
2.27	The schematic of Channel Shaped Vaned Diffuser . . . . .	30
2.28	Variation in MTT compressor performance with different Divergence Angle ( $\theta_c$ for Vaned Diffuser) . . . . .	30

2.29 Efficiency of MTT compressor with and without pre-whirl; with and without vaned diffuser ( $\theta_c = 8$ [deg]) . . . . .	30
3.1 MTT Compressor Performance Map . . . . .	31
3.2 Variation in Different Loss Components for MTT Compressor and Optimized Compressor with Vaneless Diffuser . . . . .	35
3.3 Meridional Shape of MTT Impeller and Optimized Impeller . . . . .	36
3.4 Comparison of $\eta_{TT}$ and $\Pi_{TT}$ between MTT Compressor and Optimized Compressor . . . . .	36
3.5 Optimised Compressor's Performance Map . . . . .	36
3.6 Variation in Different Loss Components for Optimized Compressor with Vaned Diffuser (OCVD) and Optimized Compressor with vane-Less Diffuser (OCVLD) . . . . .	37
3.7 Variation in $\eta_{TT}$ and $\Pi_{TT}$ for OCVD and OCVLD Design . . . . .	37
4.1 MTT Impeller . . . . .	40
4.2 MTT Vaneless Diffuser . . . . .	40
4.3 Computational Domain . . . . .	40
4.4 MTT Impeller with C-Grid and H-Grid Topology . . . . .	41
4.5 MTT Impeller Leading Edge with C-Grid Topology . . . . .	41
4.6 RMS Residuals trend for Mass and Momentum observed during 3D CFD analysis of MTT compressor . . . . .	41
4.7 Variation of $Y^+$ along the Normalised Stream-wise Length of the Impeller Blade [Both Full and Splitter] . . . . .	41
4.8 Variation in $\Pi_{TT}$ with respect to Grid Size for MTT Compressor . . . . .	42
4.9 Variation in $\eta_{TT}$ with respect to Grid Size for MTT Compressor . . . . .	42
4.10 Velocity Triangle at the Leading Edge of Inducer Shroud . . . . .	42
4.11 Blade-to-Blade Relative Mach Number contour of MTT Impeller near Shroud . . . . .	42
4.12 Blade-to-Blade Relative Mach Number contour for MTT Compressor near Shroud for different Positive Pre-whirl Angles at Inlet . . . . .	43
4.13 Variation in Total-to-Total Pressure Ratio of MTT Compressor with Positive Pre-Whirl at 240k RPM . . . . .	43
4.14 Variation in Total-to-Total Efficiency of MTT Compressor with Positive Pre-Whirl at 240k RPM . . . . .	43
4.15 Comparison of the Total-to-Total Pressure Ratio between Experimental, 1D and 3D Results at 240k rpm for MTT Compressor with and without Pre-Whirl . . . . .	44
4.16 Comparison of the Exit Total-to-Total Temperature between Experimental, 1D and 3D Results at 240k rpm for MTT Compressor with and without Pre-Whirl . . . . .	44
4.17 Comparison of MTT Blade Design with Optimized Blade Design . . . . .	45
4.18 Blade-to-Blade Relative Mach Number Contour of Optimized Impeller near Shroud . . . . .	45
4.19 Comparison of $\Pi_{TT}$ between MTT Compressor without Pre-whirl, MTT Compressor with Pre-Whirl and Optimized Compressor . . . . .	45
4.20 Comparison of $\eta_{TT}$ between MTT Compressor without Pre-whirl, MTT Compressor with Pre-Whirl and Optimized Compressor . . . . .	45
5.1 Comparison of $\eta_{TT}$ between MTT Compressor with Vaneless Diffuser and without Diffuser . . . . .	47
5.2 Flow Path Traces Across MTT Vaneless Diffuser . . . . .	48
5.3 The Geometry and Nomenclature of Vaned Diffuser . . . . .	48
5.4 MTT Impeller with 13 Vanes Airfoil Shaped Vaned Diffuser . . . . .	49
5.5 MTT Impeller with 20 Vanes Airfoil Shaped Low-Solidity Vaned Diffuser . . . . .	49
5.6 Variation in $\eta_{TT}$ for MTT Compressor with Vaned Diffuser Analyzed using One-Dimensional Performance Prediction Tool . . . . .	50
5.7 Variation in Velocity Triangle at Vaned Diffuser Inlet for Two Different Inlet Conditions . . . . .	51
5.8 MTT Impeller with 20 Vanes Channel Diffuser . . . . .	51
5.9 Grid Along Channel Diffuser for MTT Compressor . . . . .	52
5.10 Grid Along the Leading Edge of Airfoil Shaped Vaned Diffuser . . . . .	52
5.11 Mach Number Contour Across 13 Vane Channel Diffuser with Divergence Angle of 11 [deg] at Mid-Span . . . . .	53
5.12 Mach Number Contour Across 20 Vane Channel Diffuser with Divergence Angle of 11 [deg] at Mid-Span . . . . .	53

---

5.13 Mach Number Contour at Mid-Span Across 13 Vanes Channel Diffuser with divergence angle of 15 [deg] . . . . .	53
5.14 Mach Number Contour at Mid-Span Across 13 Vanes Channel Diffuser with divergence angle of 18 [deg] . . . . .	53
5.15 Mach Number Contour at Mid-Span Across 13 Vanes Channel Diffuser with divergence angle of 21 [deg] . . . . .	53
5.16 Performance of MTT Compressor for Five Different Channel Diffuser Configurations . . . . .	54
5.17 Performance of MTT Compressor for Five Different Channel Diffuser Configurations . . . . .	54
5.18 Mach Number Contour Across 13 Vane Channel Diffuser at Mid-Span . . . . .	54
5.19 Comparison of MTT Compressor Performance with Channel Diffuser and with Airfoil Shaped Vaned Diffuser . . . . .	54
5.20 Mach Number Contour Across 13 Airfoil Shaped Low Solidity Vaned Diffuser at Mid-Span . . . . .	55
5.21 Mach Number Contour Across 20 Airfoil Shaped Low Solidity Vaned Diffuser at Mid-Span . . . . .	55
5.22 Comparison of MTT Compressor's Performance with Different Diffuser Configurations . . . . .	55
5.23 Comparison of MTT Compressor's Performance with Vaneless Diffuser and with Airfoil Shaped Vaned Diffuser for 0 [deg] Pre-whirl and 25 [deg] Pre-whirl . . . . .	55



# LIST OF TABLES

1.1	Performance Characteristics for Different Micro Cogeneration Conversion Technologies . . . . .	5
2.1	Flow Properties and Geometrical Parameters used to predict MTT impeller performance . . . . .	24
2.2	Inlet Flow Properties at which Numerical and Experimental Results were Performed for two impeller without pre-whirl and for one impeller with pre-whirl . . . . .	27
3.1	The allowable range for the design variables during the optimisation . . . . .	34
3.2	Initial Candidate Point along with their Bounds . . . . .	35
3.3	Optimal Candidate Point for Stochastic Algorithm and Gradient Based Algorithm . . . . .	35
3.4	Initial and Optimal Candidate Point for compressor with vaned diffuser . . . . .	37
4.1	Geometrical Parameter of MTT Compressor . . . . .	39
4.2	Boundary Conditions used to Evaluate the Performance of MTT Compressor . . . . .	40
4.3	Boundary Conditions used during 1D, 3D and Experimental Analysis to determine MTT Compressor's Performance . . . . .	44
5.1	Performance and Geometrical Characteristics of Different Diffuser Categories . . . . .	49
5.2	Geometrical Parameter of MTT Vaned Diffuser . . . . .	52



# NOMENCLATURE

## Greek Symbols

$\alpha$	Flow Angle	[Deg]
$\beta$	Blade Angle	[Deg]
$\eta$	Efficiency	[%]
$\gamma$	Heat Capacity Ratio	[-]
$\lambda$	Impeller Distortion Factor	[-]
$\lambda_r$	Ratio of Impeller Shroud to Tip Radius	[-]
$\mu$	Adiabatic Head Coefficient or Molecular Viscosity	
$\nu_r$	Ratio of Diffuser Inlet to Exit Radius	[-]
$\omega$	Rotation Speed	[ms <sup>-1</sup> ]
$\phi$	Flow Coefficient	[-]
$\rho$	Density	[kg/m <sup>3</sup> ]
$\sigma$	Slip Factor	[-]
$\theta_c$	Divergence Angle	[deg]
$\nu$	Specific Volume	[m <sup>3</sup> /kg]

## Latin Symbols

$\dot{m}$	Mass Flow Rate	[kg/s]
$A$	Area	[m <sup>2</sup> ]
$a$	Speed of Sound	m/s
$A_R$	Area Ratio	[-]
$B$	Area Blockage Factor	[-]
$b$	Hub to Shroud Passage Width	[m]
$c_f$	Skin Friction Coefficient	[-]
$C_M$	Disk Torque Coefficient	[-]
$C_r$	Throat Contraction Ratio	[-]
$C_p$	Coefficient of Pressure	[KJ/kg K]
$d$	Diameter	[m]
$d_H$	Hydraulic Diameter	[m]
$D_{eq}$	Equivalent Diffusion Factor	[-]
$E$	Diffusion Efficiency	[-]

$f_c$	Head Loss Correction Factor	[-]
$h$	Enthalpy	[kJ/kg]
$H_{ad}$	Adiabatic Head	[kJ/kg]
$h_{th}$	Blade to Blade throat Width	[m]
$I$	Work Input Coefficients	[-]
$K$	Clearance Gap Swirl Parameter	[-]
$L_B$	Length of Blade	[m]
$M$	Mach Number	[-]
$N$	Rotations per minute (RPM)	[-]
$N_s$	Specific Speed	[-]
$P$	Pressure	[bar]
$q$	Adiabatic Head Loss Coefficient	[-]
$R$	Rothalpy	[kJ/kg]
$r$	Radius	[m]
$Re$	Reynolds Number	[-]
$s$	Clearance Gap between Impeller and Diffuser	[m]
$T$	Temperature	[K]
$U$	Blade Speed	[m/s]
$V$	Absolute Velocity	[m/s]
$W$	Relative Velocity	[m/s]
$w$	Specific Work	[kJ/kg]
$z$	Effective Number of Blade = $z_{FB} + z_{SB}L_{SB}/L_B$	[-]
$z_{FB}$	Number of Full-Length Blades	[-]
$z_{SB}$	Number of Splitter Blades	[-]

### Superscripts

'	Values Related to Rotating Frame of Reference
*	Sonic Flow Condition
$d$	Diffuser
$i$	Impeller

### Subscripts

01	Total Properties at Impeller Inlet
02	Total Properties at Impeller Tip
03	Total Properties At Vaneless Diffuser Exit
04	Total Properties At Vaned Diffuser Exit

---

1	Static Properties at Impeller Inlet
2	Static Properties at Impeller Tip
3	Static Properties At Vaneless Diffuser Exit
4	Static Properties At Vaned Diffuser Exit
<i>B</i>	Blade Parameter
<i>BL</i>	Blade Loading
<i>CH</i>	Chocking
<i>DF</i>	Disc Friction Parameter
<i>df</i>	Diffusion
<i>DIF</i>	Diffusion
<i>HS</i>	Hub to Shroud
<i>inc</i>	Incidence
<i>L</i>	Leakage Parameter
<i>m</i>	Axial Component
<i>R</i>	Recirculation Parameter
<i>SEP</i>	Seperation
<i>SF</i>	Skin Friction
<i>sh</i>	Shock
<i>th</i>	Throat
<i>u1</i>	Tangential Component at Impeller Inlet
<i>el</i>	Electrical
<i>o</i>	Overall
<i>th</i>	Thermal



# 1

## INTRODUCTION

*This chapter provides an overview on the need for micro-cogeneration systems, the significance of micro gas turbine for micro-cogeneration systems and implications of micro compressor performance on cogeneration cycle performance. The motivation and scope for this work along with the thesis outline are also presented.*

### 1.1. ENERGY TRENDS IN EUROPE

Fossil fuels (i.e., coal, oil and natural gas) are of great importance due to its ability to provide a significant amount of energy per unit mass. Coal is the most plentiful fuel in the fossil family and its usage for household purposes dates back to thousands of years. Burning of coal for electricity is relatively a newcomer in a long history of this fossil fuel. First of such occurrence took place in the 1880s. Commercial exploitation of oil to light lamps commenced in 19<sup>th</sup> century. Usage of natural gas for electricity generation was first made viable in 1940.

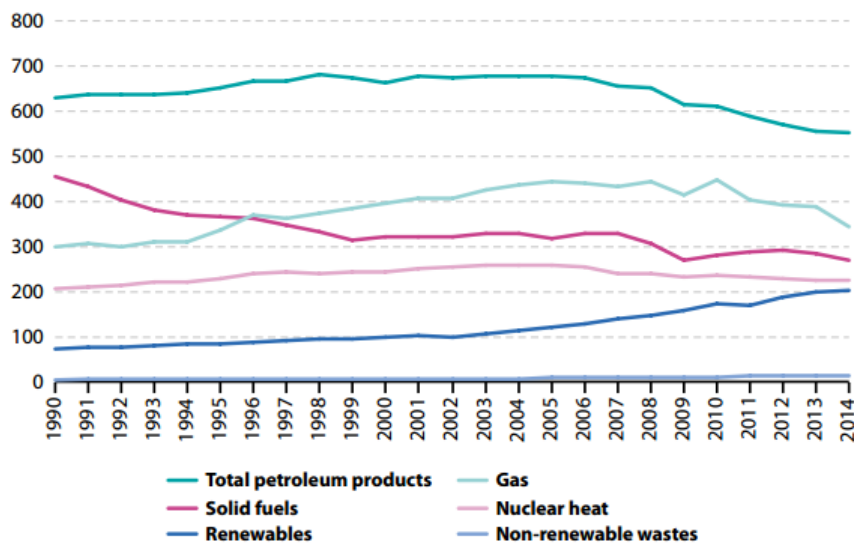


Figure 1.1: Gross Inland Energy Consumption in (%) of Total Energy Consumption [1]

Figure 1.1 highlights the percentage of energy consumption from various energy sources between 1990 to 2014 by the European Union. From figure 1.1, we can observe a significant reduction in usage of fossil fuels. The scarcity of fossil fuels and its adverse effect on climate are the primary reasons for such trend. The European union is facing unprecedented challenges to limit climate change and to overcome the economic crisis due to its increased dependence on energy imports. One of the valuable means to address these challenges is to increase the efficiency of the energy production.

Increasing energy production efficiency will increase the union's security by reducing primary energy consumption and decreasing energy imports. It will also reduce the green house gas emissions in a cost-effective

way, thus mitigating the climate change. Shifting to a more energy efficient economy will assist the European Union in saving 20% of its primary energy consumption by 2020 [2]. Undoubtedly, one of the efficient ways of producing energy is distributed energy generation.

## 1.2. DISTRIBUTED ENERGY GENERATION

Conventionally, power plants have been large, centralised units transmitting electrical and heat energy over long distance. The transmission losses and distribution cost of electrical and heat energy is over 30% of the total energy cost [3]. To minimise the losses and cost, production of energy commenced at or near the point of use, irrespective of size, fuel and technology. It is known as "Distributed Energy Generation". It is also termed as "Embedded Generation", "Dispersed Generation" and "Decentralised Generation".

The benefits of distributed energy generation are multiple and can be divided into three categories. From an environmental point of view, distributed energy systems increase system efficiency and reduce emissions. From an operational point of view, distributed energy systems reduce transmission and distribution losses, power fluctuation and increase power quality. From an economical point of view, distributed energy systems have a positive influence on energy prices due to its location flexibility [4].

$$HRP = \frac{\text{Energy produced as Heat}}{\text{Energy produced as Electricity}} \quad (1.1)$$

Figure 1.2 and 1.3 summarizes the variation in CO<sub>2</sub> emissions and cost with respect to Heat to Power Ratio (HPR) (Equation (1.1)); between centralized and distributed energy systems respectively. There is significant reduction in CO<sub>2</sub> emissions and cost for distributed energy systems, when compared to centralized energy system as shown in Figure 1.2 and 1.3.

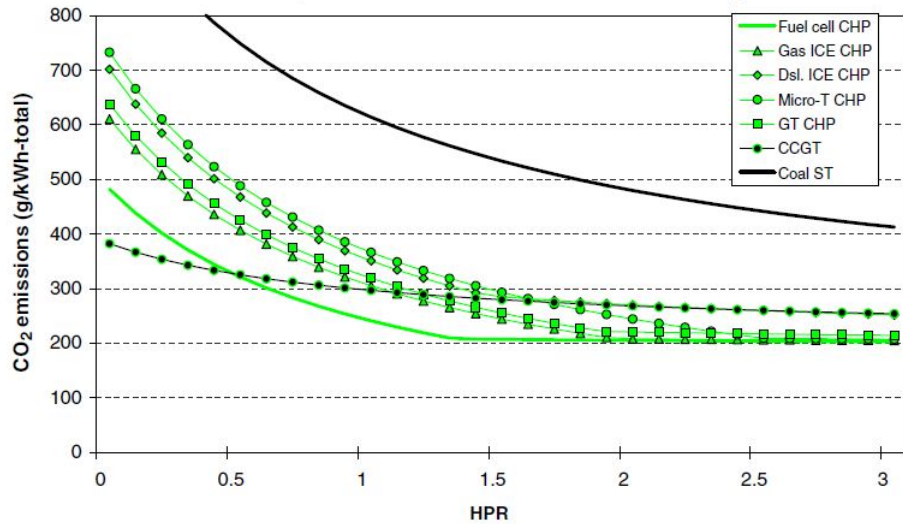


Figure 1.2: CO<sub>2</sub> emissions trend between central and distributed energy generation [5]

## 1.3. MICRO CHP SYSTEM

Combined heat and power plants (CHP) produce electricity from heat that is generated from a central process. There are three main types of CHP based on their operation and size. They are Industrial CHP, Residential CHP and Micro-CHP. As per European Union Directive, Micro-CHP means a CHP unit with a maximum capacity below 50 KW<sub>el</sub> [6]. Unlike Industrial and Residential CHP, Micro-CHP produces energy at a higher efficiency and near the point of use.

Figure 1.4 summarises the magnitude of energy input and losses associated with conventional and co-generation cycle to meet customer needs. For a conventional system, 3.9 units of energy input are required to meet customer's requirement, whereas for a micro-cogeneration system just 2.5 units of energy input is sufficient to satisfy the customer's requirement.

The overall ( $\eta_o$ ), electrical ( $\eta_{el}$ ) and thermal ( $\eta_{th}$ ) efficiency is defined as:

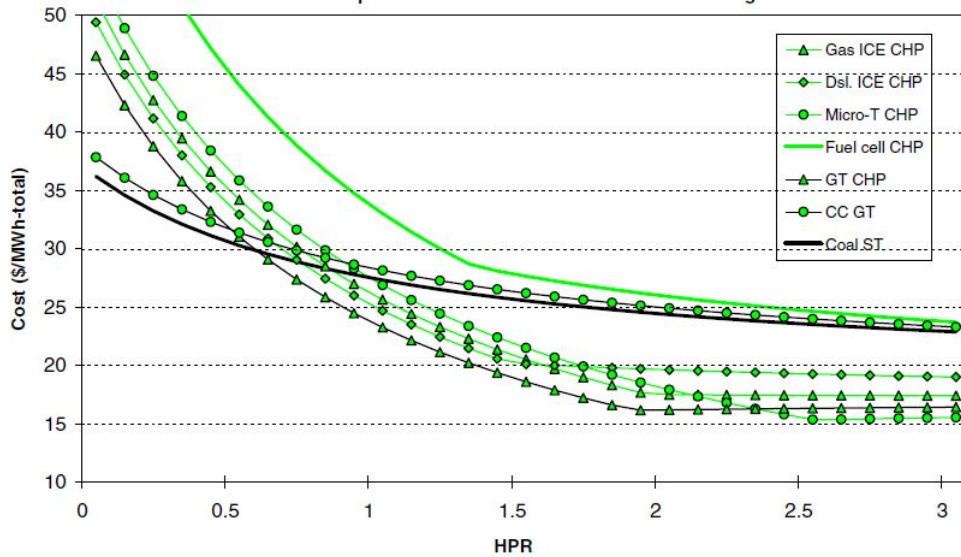


Figure 1.3: CO<sub>2</sub> emissions trend between central and distributed energy generation [5]

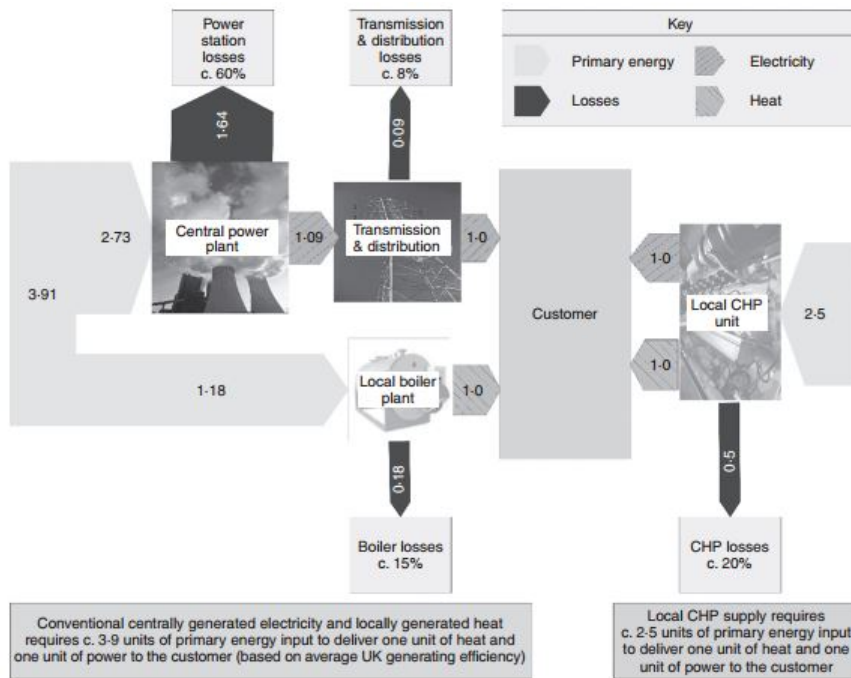


Figure 1.4: Conventional generation versus cogeneration [7]

$$\eta_o = \frac{\text{Electrical Energy} + \text{Thermal Energy}}{\text{Energy Input}} \tag{1.2}$$

$$\eta_{el} = \frac{\text{Electrical Energy}}{\text{Energy Input}} \tag{1.3}$$

$$\eta_{th} = \frac{\text{Thermal Energy}}{\text{Energy Input}} \tag{1.4}$$

Figure 1.5 distinguishes the proportion of overall, electrical and thermal efficiency for cogeneration and conventional generation. The overall efficiency for conventional cycle is 51.3%, whereas for cogeneration its 80%. Thus the micro CHP is 55.9% more efficient than conventional generation.

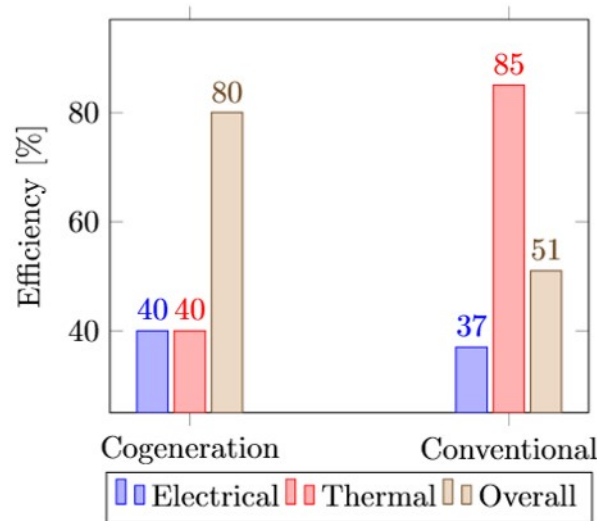


Figure 1.5: Comparison of overall ( $\eta_o$ ), electrical ( $\eta_{el}$ ) and thermal ( $\eta_{th}$ ) efficiency between cogeneration and conventional generation. Data taken from [7]

Micro cogeneration systems usually consists of four basic elements, namely a prime mover, an electricity generator, a heat recovery system and a control system. The prime mover is responsible for converting the chemical energy stored within fuel into useful form of energy by driving the electricity generator. The heat recovery system is responsible for recovering the residual thermal energy available in the system and distributing it to the surroundings. The control system is responsible for safe operation of the micro CHP unit by physically aggregating the loads and energy production. The five main conversion technologies applied to micro CHP system are reciprocating engines, stirling engines, fuel cells, Rankine cycle systems and micro gas turbines.

**Reciprocating Engine** Reciprocating engines are commonly divided into Otto engines and diesel engines. Otto engines utilise a spark plug to ignite a pre-mixed charge after compression in the cylinder, whereas in diesel engines the fuel is injected at high pressure to self-ignite the compressed air in the cylinder. For size ranging from 1-5 kW electric power output, reciprocating engines are the most fuel efficient engines [8].

**Stirling Engine** Unlike reciprocating engines, Stirling engines are piston driven machines with an external thermal energy source. Due to the external combustion process, Stirling engines are potentially more efficient, cleaner and quieter than internal combustion engines.

**Fuel Cell** Fuel cells are electro-chemical devices which convert the chemical energy stored within the fuel directly into electricity and heat without involving the process of combustion. There are various types of fuel cell technology with different designs; however, they all share the characteristics of high efficiency, no moving parts, quiet operation and low or zero emissions at point of use [9].

**Rankine Cycle System** Among all the technologies current developed for the micro-cogeneration system, ranking technology is arguably one of the most advanced concepts. The most familiar Rankine power plant utilises steam turbines for industrial CHP applications with power output up to several  $MW_{el}$ . Application of steam power plant for applications up to  $KW_{el}$  is highly inefficient. In order to overcome this drawback, Organic Rankine Cycle (ORC) systems were introduced. ORC systems use organic fluid with favourable thermodynamic properties, resulting in high overall efficiency and very high turbine efficiency when compared to steam Rankine cycle.

The performance characteristics for different micro cogeneration prime mover technologies is listed in table 1.1. Micro gas turbines, which will be discussed in detail in section 1.4, is also listed in the table for comparison purpose. As Stirling engine system, fuel cell system and Rankine cycle system are yet in research and development phase, reciprocating engines and micro gas turbines are commercially viable option as

prime mover for micro-CHP units. Due to low emission and noise levels, micro gas turbines are preferred over reciprocating engines for micro-CHP units.

Table 1.1: Performance Characteristics for Different Micro Cogeneration Conversion Technologies [4]

	Reciprocating Engines	Stirling Engines	Fuel Cell	Rankine Cycle Engines	Micro Gas Turbines
$\eta_o$ [%]	85-90	80-90	80-85	80-90	70-90
$\eta_{el}$ [%]	20-25	10-25	25-33	8-15	14-23
Emissions	High	very low	almost zero	N.a.	Low
Noise level	High	Moderate	Low	Moderate	Low/Moderate
Fuel flexibility	Good	High	Good	Very High	Good

## 1.4. MICRO GAS TURBINES FOR MICRO CHP SYSTEM

Micro gas turbines are small-scale gas turbines operating on Brayton cycle. The temperature-entropy diagram of an ideal recuperated Brayton cycle is shown in Figure (1.6). Unlike their bigger counterparts, micro gas turbines have increased internal losses, due to relatively higher tip clearance, and high viscous effects because of low Reynolds numbers. Micro gas turbines are a natural option as the prime mover for micro-CHP applications due to its compact size; high specific power; low vibration and noise; a small number of moving parts and high fuel flexibility. Figure (1.7) shows a schematic of a recuperated micro gas turbine CHP unit of Micro Turbine Technologies (MTT). MTT is an innovative company developing advanced micro gas turbines for micro-CHP and automobile applications. The main components of MTT recuperated micro gas turbines are the compressor, the recuperator, the combustor, the turbine, the heat recovery unit and the generator.

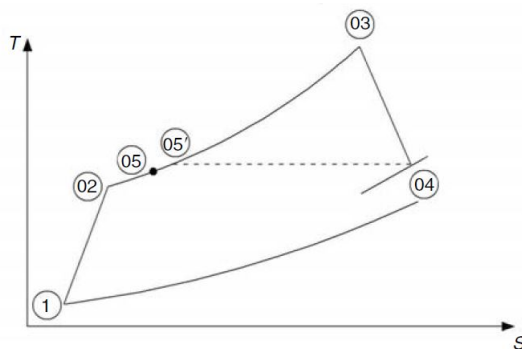


Figure 1.6: T-S Diagram of Ideal Brayton Cycle with Recuperation [10]

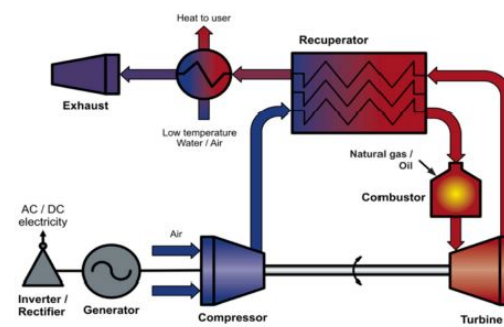


Figure 1.7: Schematic of MTT Recuperated Micro Gas Turbine CHP System [11]

**Compressor** MTT CHP unit utilises an automotive turbocharger compressor to compress the atmospheric air to a pressure ratio of 3.  $\approx 8.5$  KW of power is supplied to the compressor in order to achieve the mentioned work done on the fluid. The main components of the compressor are the unshrouded impeller, vaneless diffuser and volute.

**Recuperator** In order to meet MTT CHP units' thermal efficiency target [12], recuperator effectiveness must be above 85% with an acceptable pressure loss of just 4%. Since primary-surface (PS) recuperator offer the most favourable combination of effectiveness and specific weight, they are incorporated in MTT CHP unit. The PS recuperator for MTT CHP unit is made out of stainless steel.

**Turbine** MTT CHP unit utilises an automotive turbocharger turbine to expand the gas from 3 bar total pressure to atmospheric pressure. The current turbine design is capable of extracting  $\approx 15.0$  KW of energy from the working fluid. The main components of the turbine are volute, unshrouded turbine impeller and diffuser.

**Combustor** Can type combustion chamber is utilised by MTT CHP unit to meet the energy requirements. Meticulous design of the combustor resulted in stable combustion with low emission levels. The main components of MTT combustor are the fuel injector, swirler, ignitor, combustor casing and liner. MTT strive towards green energy resulted in developing advanced combustion techniques like Premixed combustion with braided burner. The mentioned technique is still in R&D phase.

## 1.5. SIGNIFICANCE OF COMPRESSOR PERFORMANCE ON MTT MICRO CHP UNIT

Extensive R&D on an automotive turbocharger for past seventy years has stalled the efficiency levels of compressor and turbine. Nevertheless, improvement in micro gas turbine performance can be achieved by suitable modification of turbocharger technology, especially considering that turbochargers usually employ centrifugal compressor with a vaneless diffuser to minimise production cost and maximise flow range, whereas micro gas turbines require higher efficiency and pressure ratio for a confined operating range.

A cycle study of the MTT recuperated micro gas turbine was performed to determine the significance of compressor performance on the system performance. The input data for modelling the components of the CHP cycle were taken from the experimental results. It was observed that 1% increase in compressor efficiency resulted in increasing the electrical efficiency by  $\approx 0.4\%$ . Figure 1.8 and 1.9 shows the significance of compressor efficiency on compressor pressure ratio and on the electrical efficiency of MTT CHP cycle. In conclusion, increasing the performance of MTT compressor is indeed pivotal in increasing the overall performance of the MTT CHP system.

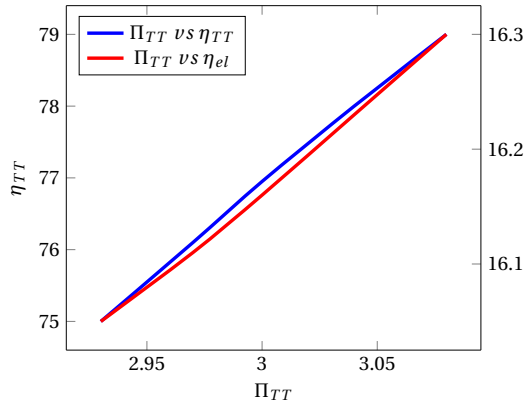


Figure 1.8: Variation in Compressor Total to Total Efficiency and MTT CHP's Electrical Efficiency with Respect to Compressor Pressure Ratio

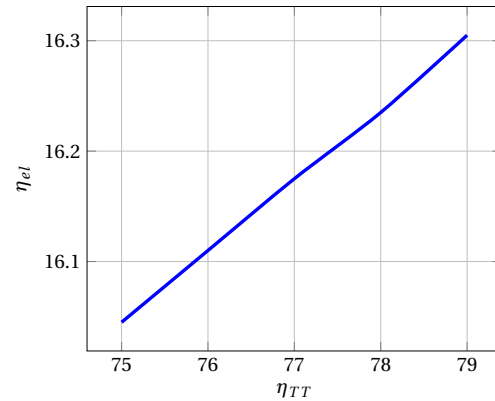


Figure 1.9: Variation in Electrical Efficiency with Respect to Compressor Efficiency

## 1.6. THESIS OBJECTIVES

Compressor designed for automotive applications exhibits robust performance for different engine operating conditions. Adopting such compressor for micro gas turbine applications mostly results in operating at off-design conditions, thus reducing the performance of the compressor. Similar scenario is encountered with centrifugal compressor studied in this work, since a turbocharger compressor is adopted for MTT recuperated micro gas turbine. Thus, the objectives of this thesis are

1. To provide a better understanding of the compressor flow structure and loss mechanisms, allowing to identify various design aspects whose improvement can lead to increase the compressor performance.
2. To develop an optimisation methodology, which allows investigating the significance of various geometrical parameters of the compressor on its performance.
3. To analyse and quantify the influence of pre-whirl vanes on compressor performance.
4. To analyse and quantify the influence of vanned diffuser and the vane shape on the compressor performance.
5. To recommend a cost effective option to increase the performance of the MTT Compressor.

## 1.7. RESEARCH QUESTIONS

Based on the objectives that have been set for this work, it can be said that this thesis will provide the insight on the important geometric parameters that can be optimised to improve the performance of the compressor and also about the importance of pre-whirl and vaned diffuser on compressor performance. Therefore, the research questions that will be answered by this thesis can be stated as follows:

- What are the important geometric parameters that need to be modified in order to enhance the performance of the MTT Compressor?
- What is the cost effective option to enhance the performance of the MTT compressor?

## 1.8. THESIS OUTLINE

This thesis is structured as follows. Chapter (2) presents the methodology for a one-dimensional performance prediction of centrifugal compressors, operating with fluids obeying to the ideal gas law. This approach sequentially evaluates the flow properties in the impeller, vaneless diffuser, and the vaned diffuser. It allows to estimate the source of the losses within a compressor. The numerical results computed by this tool have been validated against the experimental data provided by MTT. In Chapter (3) the optimisation of the impeller has been performed by coupling a gradient-based algorithm and stochastic algorithm with 1-D performance prediction tool. Chapter (4) presents the numerical study performed with a commercial CFD code which solves the three-dimensional (3D) Reynolds-averaged Navier-Stokes (RANS) equations. Steady-state simulations have been carried to approximate the real, time-dependent flow physics with satisfactory results and shorter computational time. The results of the CFD computations have been validated against the experimental data provided by MTT. Chapter (5) illustrates the influence of the vaned diffuser on the MTT compressor's performance. A brief description of the three main categories of vaned diffusers (i.e., Channel Diffuser, Airfoil Shaped Vaned Diffuser and Low Solidity Vaned Diffuser) along with the most important design parameters for the vaned diffuser follows. Finally, the numerical study performed with a commercial CFD code for MTT compressor with vaned diffuser is presented.



# 2

## MEAN LINE COMPRESSOR DESIGN

*This chapter presents fundamental design and operation of micro gas turbine compressor along with the one-dimensional methodology to determine its design and off-design performance. The followed methodology is tailor-made for operating fluids obeying the ideal gas law. The methodology evaluates the flow properties and estimates the source for entropy generation across compressor components namely, the unshrouded impeller, the vaneless diffuser and the vaned diffuser.*

### 2.1. CENTRIFUGAL COMPRESSORS

Centrifugal compressors produce a sufficiently large rise in pressure and density across each stage, hence are used in situations where the specific speed ( $N_s$ ) requirements are between 0.7 – 1 and the pressure rise is high. The specific speed of the centrifugal compressor is calculated using Equation (2.1). Centrifugal compressors are generally made of four different components namely, Stationary Inlet Casing, Rotating Impeller, Stationary Diffuser and Volute. Occasionally inlet guide vanes are used to increase the operational range of the compressor.

$$\text{Specific Speed, } N_s = \frac{\omega \sqrt{\dot{m}/\rho_1}}{H_{ad}^{3/4}} \quad (2.1)$$
$$\text{Adiabatic Head, } H_{ad} = C_p(T_{02} - T_{01})$$

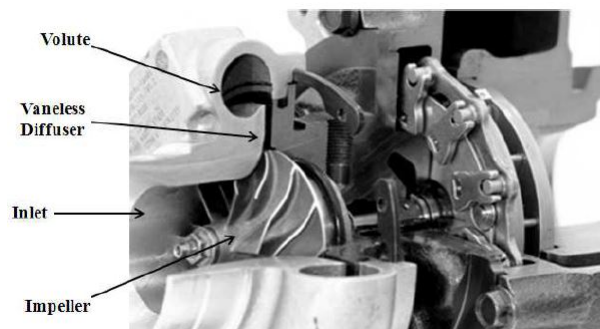


Figure 2.1: Main Components of Turbocharger Centrifugal Compressor [13]

The stationary inlet casing directs the flow axially into the impeller. The enthalpy of the working fluid is increased due to difference in the blade speed and due to the deceleration of the relative velocity across the impeller. At the impeller exit, the working fluid still contains a substantial amount of kinetic energy, which can be recovered through diffusion process using either vaneless or vaned diffuser. A small amount of further diffusion takes place across the volute. Figure (2.1) shows the main components of centrifugal compressor

with inlet, impeller, vaneless diffuser and volute. The work done on the working fluid can be written in terms of kinetic energy as shown in Equation (2.2). Equation (2.2) can also be written in terms of change in total enthalpy as shown in Equation (2.3). Equating right hand side of Equation (2.2) and (2.3) results in Rothalpy Equation (2.4), which remains constant across the compressor wheel.

$$w = \frac{1}{2}(V_2^2 - V_1^2) + \frac{1}{2}(U_2^2 - U_1^2) + \frac{1}{2}(W_1^2 - W_2^2) \quad (2.2)$$

$$w = h_{02} - h_{01} = h_2 - h_1 + \frac{1}{2}(V_2^2 - V_1^2) \quad (2.3)$$

$$h_1 + \frac{1}{2}(W_1^2 - U_1^2) = h_2 + \frac{1}{2}(W_2^2 - U_2^2) \quad (2.4)$$

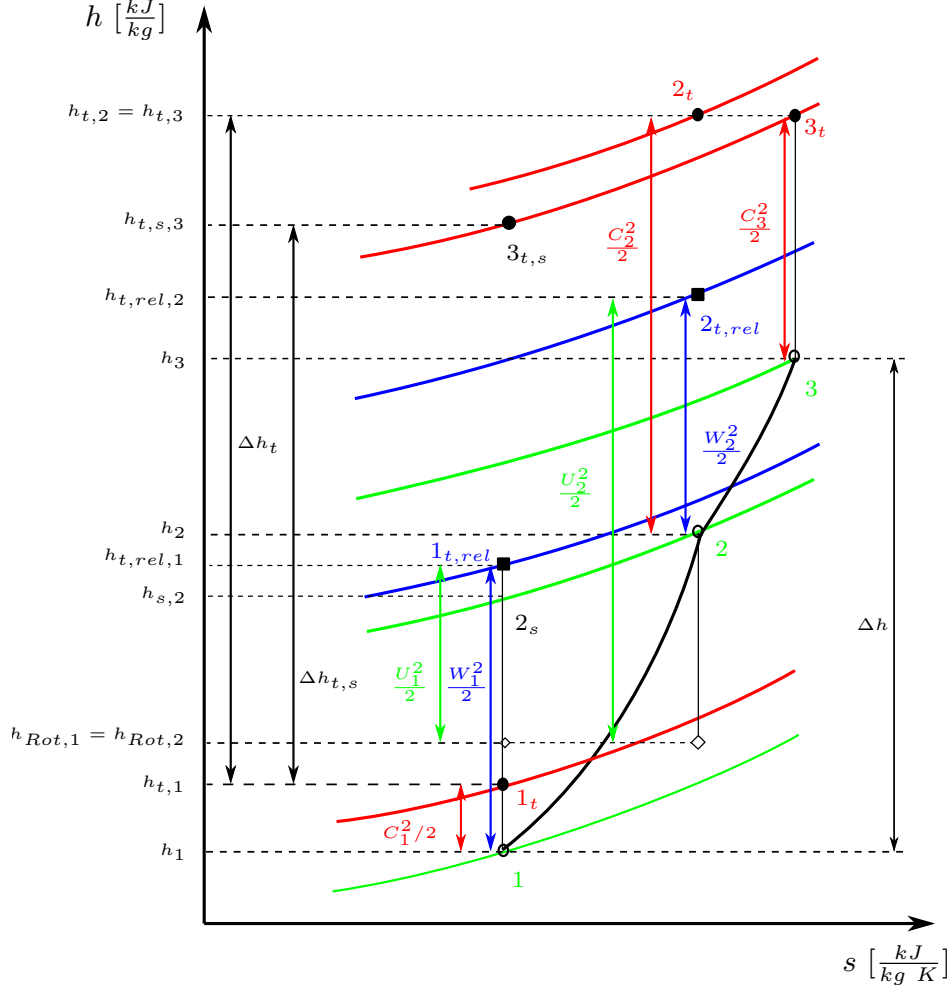


Figure 2.2: Enthalpy Rise across a Compressor Stage

For centrifugal compressors, the term  $\frac{1}{2}(U_2^2 - U_1^2)$  in Equation (2.2) contributes primarily to the increase in static enthalpy and pressure of working fluid. This is the primary reason for centrifugal compressors exhibiting higher efficiency even in the case of poor aerodynamic behavior due to largely separated flow. The steps in which enthalpy changes across the compressor is shown in Figure (2.2). The flow physics across the compressor along with the factors affecting its performance will be discussed in Section (2.2) and (2.3).

## 2.2. FLOW PHYSICS WITHIN THE IMPELLER

Due to the adverse pressure gradient, the flow field emerging across an impeller is very complex, three-dimensional, and turbulent; all due to the influence of blade curvature and rotation. Figure (2.3) illustrates

the flow physics observed in an unshrouded centrifugal compressor impeller. During the initial phase of centrifugal compressor development, Dean [14] discussed the existence of jet and wake flow pattern between two blades of the impeller. The unsteadiness observed downstream of the impeller and the constant pressure across part of each passage near the shroud was the preliminary reason for such a conclusion from Dean. Dean's conclusion was backed by extensive laser anemometry measurements performed by Eckart [15], though there was some inaccuracy in Dean's model.

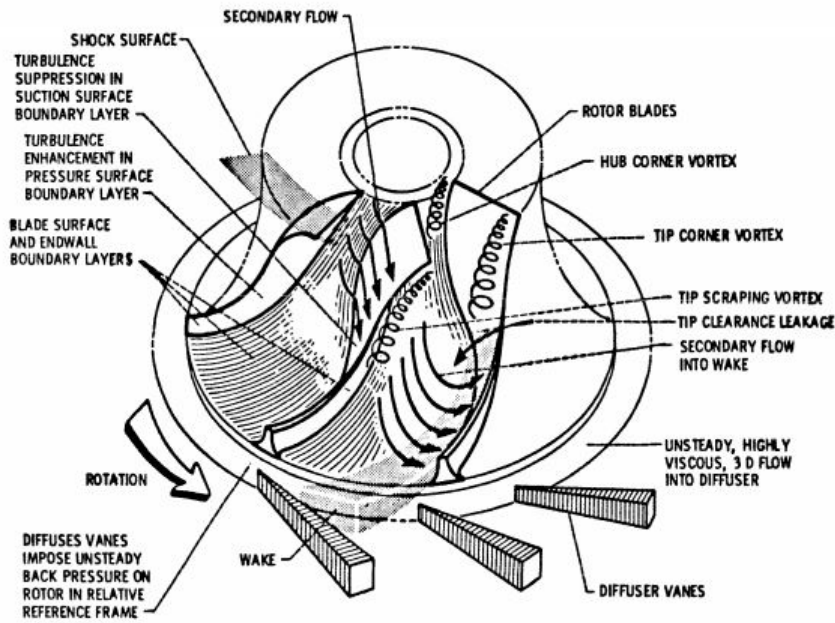


Figure 2.3: Flow Physics Across Impeller [16]

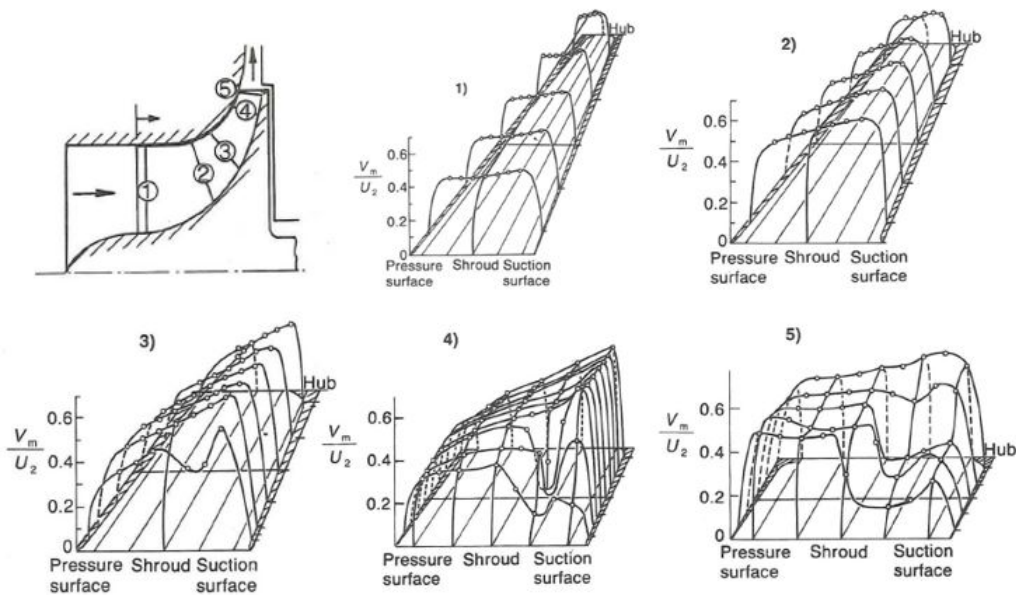


Figure 2.4: Velocity Measurements by Eckardt in a Centrifugal Compressor with no Backsweep [17]

Eckart measured flow velocities, directions, and fluctuations across impeller of a centrifugal compressor running at a tip speed of 400m/s. Velocity measurements were taken at five different planes along the stream-

wise direction of the impeller. The same is shown in the Figure (2.4). It can be observed that there is no irregularity pattern at plane 1 and plane 2. At plane 3, flow irregularity commences and propagates towards the hub, when flow continues towards plane 4. The separation grows and flattens as the flow continues to the outlet plane 5. The flow separation from the shroud is not surprising due to the acceleration of the flow along the convex surface and deceleration of the flow with separation along the concave surface. Varying the shroud curvature radius smoothly is an important design criterion to delay the flow separation along the shroud surface.

**Secondary Flow** The flow that is perpendicular to primary flow is termed as a secondary flow. In a centrifugal impeller, the meridional plane curvature and blade to blade curvature produces secondary flows. Secondary flow moves low stagnation fluid to regions where static pressure is low. Low stagnation fluids are those in boundary layers or in regions of a wake.

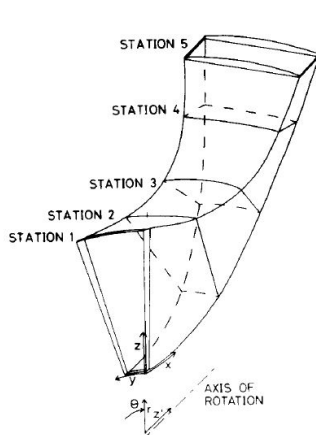


Figure 2.5: Impeller Passage with Measurement Planes [18]

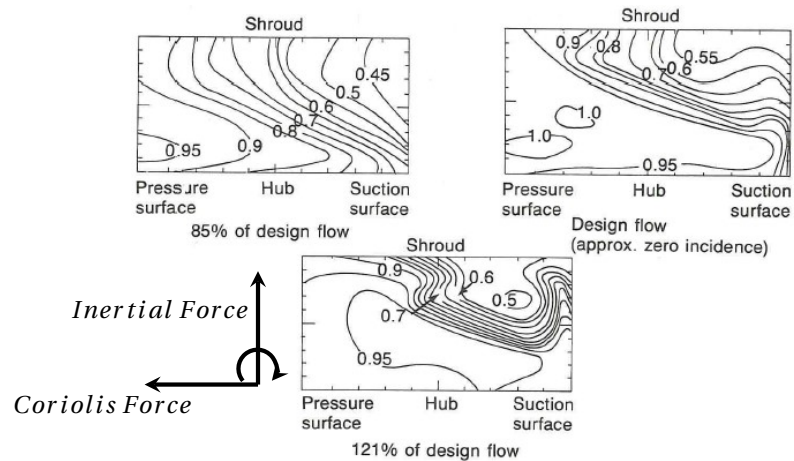


Figure 2.6: Influence of Rossby Number on Secondary Flow Motion at Station 5 shown in Figure (2.5) [18]

For a centrifugal compressor, the movement of secondary flows can be better predicted using Rossby number. Rossby number is the ratio of inertial force to Coriolis force. In the case of a high Rossby number, secondary flows are drawn towards the shroud due to the domination of the inertial term. When the Rossby number is low, Coriolis term domination leads to the motion of the secondary flows towards the suction surface of the impeller blade. The influence of Rossby number on motion of wake can be seen in Figure (2.6). The wake is located at the suction surface at 85% of the design flow due to the domination of Coriolis force whereas for 121% of the design flow the wake is located on the shroud due to the domination of the inertial force.

**Boundary Layer Stability** The flow over curved surface affects the stability of the flow, leading to a transition from laminar to turbulent boundary layer structure. The flow over the impeller blades produces an effect analogous to the effect of flow over the curved wall. Stable and unstable flow over the curved wall and the rotational system are shown in Figure (2.7). In the case of centrifugal impeller, all four cases are present [19]. The effect of rotation stabilizes the flow over the suction surface; suppresses the turbulence in the boundary layer and reduces the ability to resist deceleration. Similar behavior can be observed for flows over the convex wall, such as the shroud. It can be observed in Figure (2.3), separation begins on the shroud, thus the meticulous design of shroud will result in achieving the flow stability. Nevertheless, flow separation is likely for flows over the curved wall and over the suction surface of the rotational system due to the stabilization of turbulence in the boundary layer.

**Viscous Effects** The term viscous effects represents the shear stress generated due to turbulence. Viscous effects have three major influences on the flow over a compressor. They are,

1. Viscous effects put a limit on the pressure rise achieved in a compressor. Attempts to exceed this limit leads to a flow instability and the rotating surge or stall.

2. Viscous effects lead to blockage, reduction in effective flow area in the compressor. Blockage affects the work input on fluid and has an enormous effect on the mass flow capacity.
3. Viscous effects in shear layers are primarily responsible for loss generation apart from losses generated due to shock waves.

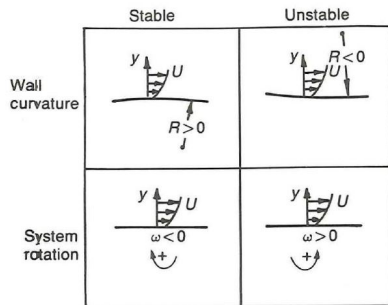


Figure 2.7: Types of flow over a curved wall and over a rotating system [19]

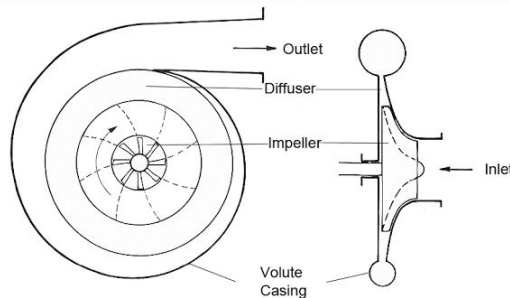


Figure 2.8: Schematic of compressor with vaneless diffuser

### 2.3. FLOW PHYSICS ACROSS DIFFUSER

Flow leaves the impeller of the centrifugal compressor with a high absolute velocity and at large angle with respect to radial direction. This flow needs to be decelerated in order to achieve a reasonable static pressure rise and Total-to-Static efficiency of the compressor, and this is the role of the diffuser. There are broadly two types of diffusers, namely the vaneless diffuser and the vaned diffuser.

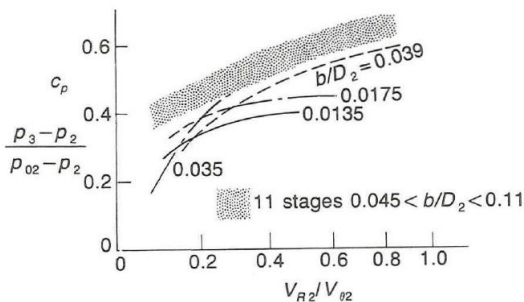


Figure 2.9: Variation of static pressure recovery for a vaneless diffuser [20]

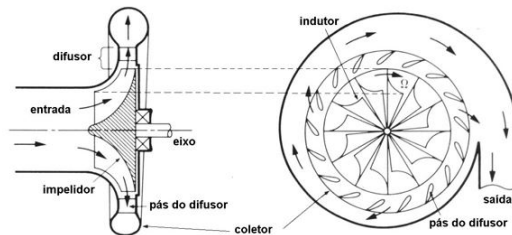


Figure 2.10: Schematic of compressor with vaned diffuser

#### 2.3.1. FLOW PHYSICS ACROSS VANELESS DIFFUSER

The vaneless diffusers are used for applications where wide operating range or low cost are of prime concern. Although the design of vaneless diffuser is simple, the aerodynamic behavior is complicated due to the influence of viscous stresses along the long flow path between inlet and outlet. The geometrical variables required to design a vaneless diffuser are diameter ratios from the inlet to outlet and ratio of inlet axial width to the inlet diameter. In the case of a variable width diffuser, an additional ratio or angle is required. A schematic of compressor with vaneless diffuser is shown in Figure (2.8).

Decreasing the axial width of the diffuser from the inlet to outlet has a direct effect on the radial velocity and indirect effect on the tangential velocity. The radial velocity decreases more slowly than the tangential velocity resulting in reducing the absolute flow angle across the diffuser. The reduction in absolute flow angle reduces the distance traveled by flow path from the inlet to the outlet. The losses in the vaneless diffuser are reduced due to the shorter flow path. Nevertheless, a major drawback for contracting diffuser is the increased frictional effects at walls.

The performance of the vaneless diffuser falls off as the absolute Mach number at the inlet is increased. Increasing the absolute Mach number at the diffuser inlet increases the inlet flow angle with respect to radial direction, thus increasing the distance traced by the flow path from the inlet to the outlet. Rogers (1980) shows that increasing the impeller exit Mach number  $U_2/a_0$  from 0.65 to 1.01, decreases the pressure coefficient

across diffuser by 0.1. Figure (2.9) summarizes the variation in static pressure recovery for a vaneless diffuser with respect to inlet  $V_{R2}/V_{\theta 2}$ , for different width to diameter ratio.

The static pressure across the vaneless diffuser continues to increase, as the diameter ratio of the vaneless diffuser increases but at a progressively slower rate. The total pressure across the vaneless diffuser continues to fall with increased diameter ratio, due to losses. Thus it is preferable to limit the diameter ratio to a value less than two and attempt to achieve the additional pressure rise through the use of the volute.

### 2.3.2. FLOW PHYSICS ACROSS VANED DIFFUSER

The vaned diffuser is used for applications where compressor efficiency is of prime concern. Vaned diffuser increases the efficiency of the compressor at the expense of reduced operating range. The addition of vanes in vaneless diffuser reduces the unsteadiness in the flow due to rapid mixing, which results in increased compressor performance. Vaned diffusers can be categorized for instance with solidity (Conventional Vaned Diffuser - CVD, Low Solidity Vaned Diffuser - LSVD) or with vane profile (circular arc or flat plate). Different factors affecting the operating range of the compressor and vaned diffuser performance will be discussed in this Section. Figure (2.10) shows the schematic of conventional vaned diffuser with vaneless and semi-vaneless space.

**Vaneless Space** Vaneless space is the radial gap between the impeller and the diffuser. A vaneless space ratio ( $r_3/r_2$ ) of 1.05 has to be maintained in order to reduce compressors' vibrations and noise generation. Maintaining a radius ratio of 1.05 also assists in reducing the overall size of the machine. Nevertheless, for compressors with the supersonic flow at impeller exit, the vaneless space ratio is usually increased so that the flow is subsonic at the leading edge of the vane. Increasing the vaneless space ratio beyond 1.25 is not recommended because the vaneless diffusion process is less efficient.

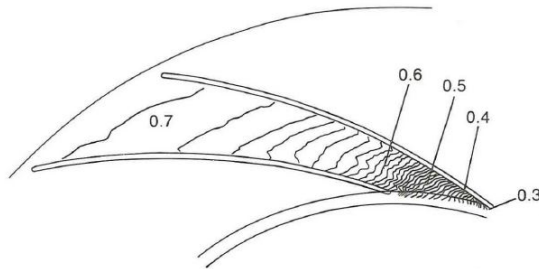


Figure 2.11: Mean static pressure contours in a vaned diffuser (Normalized by  $\rho U_2^2$ ) [21]

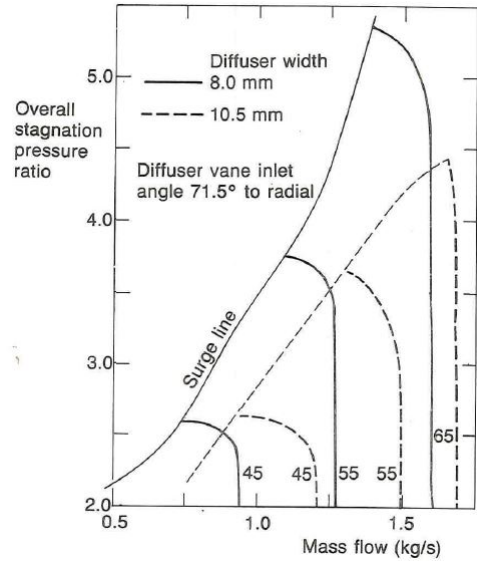


Figure 2.12: Overall Stagnation PR for Same Impeller Operating with Vaned Diffuser of Different Axial Width [22]

**Semi-Vaneless Space** Semi-vaneless space is the space between the leading edge of the vane and the throat of the vaned diffuser. The unsteadiness in the flow from impeller tip is removed from the semi-vaneless space due to mixing, thus causing a rapid increase in static pressure as shown in Figure (2.11). Semi-vaneless space also plays a significant role in generating losses and creation of blockage. A high pressure rise upstream of the diffuser throat gives high blockage, resulting in reduced pressure recovery downstream as shown in Figure (2.11).

Thus from above discussion, we can conclude that the single most important step in the design of vaned diffuser is the correct prediction of the throat area for a given impeller design. This design step is termed as component matching, i.e., matching the flow coefficient at the inlet of the vaned diffuser to the flow coefficient at the exit of the impeller.

**Component Matching** The rise in pressure and density across an impeller is sufficiently large that it has to be considered during the design of vaned diffuser, else a serious loss in vaned diffuser's pressure recovery, flow capacity, and efficiency is inevitable. Under-prediction of impeller exit pressure and density will result in designing a vaned diffuser with a larger throat area and with vanes inclined at a smaller angle to radial than in an actual case. This mismatch in design might lead to a stall in vanes. For a matched vaned diffuser, a similar trend is observed when the compressor operates at mass flow rates lower than its design mass flow rate as shown in Figure (2.12). The mentioned design and trend is reversed (choking), when flow parameters at the impeller exit are over predicted.

## 2.4. MEANLINE MODEL FOR CENTRIFUGAL COMPRESSORS

Three-Dimensional (3D) computational fluid dynamic (CFD) codes are capable of analyzing the flow through the centrifugal compressor in great detail. It can be imagined that the need for mean line performance prediction methods can be superseded due to the advancement and sophistication of CFD codes. Nevertheless, incorporating CFD techniques during preliminary design phase will be cumbersome. Thus, meanline methods continues to play a vital role is design and application of centrifugal compressor.

For the current work, development of a meanline tool will assist in determining the design flaws of existing MTT compressor. The meanline tool can also be utilized for optimizing the performance of the compressor. The description of the meanline tool developed in this project is given hereinafter.

### 2.4.1. MEANLINE IMPELLER PERFORMANCE ESTIMATION

The impeller is the most critical and geometrically complex component of the centrifugal compressor. A rotating impeller imparts energy to working fluid resulting in increasing its pressure, velocity, and enthalpy. Section (2.2) described the flow physics and the losses encountered by impeller during operation. In order to capture the performance of the impeller in close accordance with experiment results, 16 non-dimensional losses were computed as a function of the geometrical dimensions, relative velocities and Reynolds number.

The losses occurred across the blade passage are imposed at the impeller tip. This leads to a deterioration in prediction accuracy, as this approach is strictly correct only for incompressible flows. Nevertheless, reasonable prediction accuracy can be achieved by incorporating a head loss multiplying factor  $f_c$  (Equation (2.6) [23]), while calculating losses across impeller. The adiabatic head coefficient of the centrifugal compressor is defined as the ratio of the amount of energy required to elevate the pressure of the working fluid to the square of the blade speed at the impeller tip. The adiabatic head coefficient at impeller tip is given as,

$$\mu = I_B - f_c \Sigma \Delta q \quad (2.5)$$

$$\text{Head loss correction factor, } f_c = \frac{2T'_{T2}}{T'_{T1} + T'_{T2}} \frac{2(P'_{T1} - P_1)}{\rho_1 W_1^2} \quad (2.6)$$

### CALCULATION OF THE IMPELLER WORK INPUT

The general form of impeller work input equation is written as,

$$(\mu/\eta_{ad}) = \Delta H/U_2^2 = I_B + I_{DF} + I_L + I_R \quad (2.7)$$

The  $I_B$  represents the contribution of work input from blades. The right-hand terms namely, windage and disk friction ( $I_{DF}$ ), seal leakage ( $I_L$ ), and recirculation ( $I_R$ ) are the losses which have to be compensated by the work input term ( $I_B$ ) to achieve required pressure rise across the impeller.

The blade work input coefficient can be written as

$$I_B = \sigma (1 - \lambda \phi_2 \cot \beta_2) - U_1 C_{u1} / U_2^2 \quad (2.8)$$

Where  $\phi_2 = \dot{m}/(\rho_2 A_2 U_2)$ ,  $\sigma$  is slip factor and  $\lambda$  is impeller tip distortion factor, shown in Equation (2.9) and (2.10) respectively.

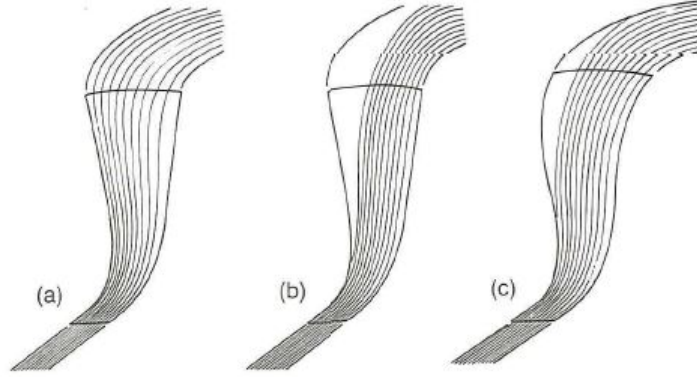


Figure 2.13: Streamlines pattern in an impeller for inviscid flow: (a) fully attached flow, no backsweep; (b) separated flow, no backsweep; (c) separated flow, with backsweep [24]

**Slip Factor** Due to the rotation of the impeller, the pressure is higher on the pressure side of the blade and lower on the suction side. Nevertheless, to satisfy the Kutta-Joukowski condition the pressure difference must be zero at the trailing edge. To satisfy this condition, reduction in pressure differences has to be gradual, beginning somewhere upstream of the trailing edge. Since there is no longer sufficient force available at the suction surface of the trailing edge, the average force is turned back to give a slip velocity in the opposite sense to the impeller rotation. This phenomenon is termed as the slip. Slip is fundamentally an inviscid flow effect and can be calculated using inviscid methods for blade-to-blade flow. Wiesner expression for slip factor, Equation (2.9), gave the most satisfactory agreement and in absence of anything better, this is the best expression to use [19]. Figure (2.13) shows the streamline pattern for attached flow; separated flow without back sweep; separated flow with a back sweep in an impeller.

$$\sigma = 1 - \frac{\pi}{N}(\cos \beta_2) \quad (2.9)$$

**Impeller Distortion Factor** The impeller distortion factor ( $\lambda$ ) is a key parameter in the blade input equation. Literature from Aungier offers specific empirical relation (Equation (2.10) [23]) to estimate this parameter.

$$\lambda = \frac{1}{(1 - B_2)} \quad (2.10)$$

**Impeller Blockage Factor** As explained in Section (2.2), Blockage in impeller plays a significant role in reducing the work input on the fluid. Meticulous formulation of blockage factor is necessary to estimate this parameter in close agreement with experimental results. Aungier formulated an empirical relation for impeller blockage factor, Equation ((2.11)[23]).

$$B_2 = (\Delta q_{SF} + \Delta q_{HS}) \frac{U_2^2}{W_2^2} + \left[ 0.3 + \frac{b_2^2}{L_B^2} \right] \frac{A_R^2 v_1 b_2}{v_2 L_B} + \frac{s_{CL}}{2b_2} \quad (2.11)$$

Passage area ratio  $A_R$  is defined as,

$$A_R = \frac{A_2 \sin \beta_2}{A_1 \sin \beta_{th}} \quad (2.12)$$

**Impeller Disk Friction** Literature from Daily and Neca [25] [26] are the best available sources for estimating windage and disk friction losses. The considered four are for different flow regimes, namely:

**Laminar, merged boundary layer** The disk torque coefficient for this regime can be calculated using Equation (2.13) [27]

$$C_{M1} = \frac{2\pi}{(s/r)Re} \quad (2.13)$$

**Laminar, separated boundary layer** The disk friction coefficient for this regime can be calculated using equation (2.14) [27]

$$C_{M2} = \frac{3.7(s/r)^{0.1}}{\sqrt{Re}} \quad (2.14)$$

**Turbulent, merged boundary layer** The disk friction coefficient for this regime can be calculated using equation (2.15) [27]

$$C_{M3} = \frac{0.08}{(s/r)^{1/6} Re^{1/4}} \quad (2.15)$$

**Turbulent, separated boundary layer** The disk friction coefficient for this regime can be calculated using equation (2.16) [27]

$$C_{M4} = \frac{0.102(s/r)^{0.1}}{Re^{0.2}} \quad (2.16)$$

The largest of all four torque coefficients corresponds to the correct flow regime encountered in the impeller.  $Re$  is the Reynolds number defined by  $Re = (\rho\omega r^2)/\mu$ . Aungier applied empirical corrections to these ideal disk torque coefficients for centrifugal compressor impeller. Denoting the torque coefficient calculated by Daily and Nece as  $C_{M0}$ , the corrected value is given by Equation 2.17. Aungier observed that Equation (2.17) [23], resulted in very accurate work input predictions even for ultra low flow coefficient stages where leakage, windage and disk friction play a very dominant role.

$$C_M = C_{M0} \frac{(1 - K)^2}{(1 - K_0)^2} \quad (2.17)$$

$$K = K_0 + C_q(1.75K_F - 0.316)r_2/s \quad (2.18)$$

$$K_0 = \frac{0.46}{1 + 2s/d} \quad (2.19)$$

$$C_q = \frac{\dot{m}_L(\rho r_2 U_2 / \mu)^{1/5}}{2\pi\rho r_2^2 U_2} \quad (2.20)$$

The torque is calculated for each side of the disk. The disk and cover side values are adjusted with a constant 0.8, which is an "experience factor" selected from numerous experimental stage work input curves [23].

$$C_{MD} = 0.8C_M \quad (2.21)$$

$$C_{MC} = 0.8C_M \frac{L[1 - (d_1 s/d_2)^5]}{r_2 - r_1} \quad (2.22)$$

The power consumed due to disk friction and windage can be calculated using Equation (2.23) [23].  $C_{MC}$  is zero for open impellers assuming half of the clearance gap leakage flow is re-energized by the impeller after re-entraining into the blade passage flow.

$$I_{DF} = \frac{(C_{MD} + C_{MC})\rho_2 U_2 r_2^2}{2\dot{m}} \quad (2.23)$$

**Impeller Seal Leakage** Prediction of work input for impeller requires consideration of seal leakage loss. The leakage loss for unshrouded impeller can be calculated using Equation (2.24) [23].

$$I_L = \frac{\dot{m}_{CL} U_{CL}}{2U_2 \dot{m}} \quad (2.24)$$

Leakage mass flow rate  $\dot{m}_{CL}$  and Leakage velocity  $U_{CL}$  can be calculated using Equation (2.25) and (2.26) respectively [23].

$$\dot{m}_{CL} = \rho z s L U_{CL} \quad (2.25)$$

$$U_{CL} = 0.816 \sqrt{(2\Delta P_{CL} / \rho_2)} \quad (2.26)$$

The average pressure difference across the gap ( $\Delta P_{CL}$ ) can be calculated using Equation (2.27). Average radius across impeller ( $\bar{r}$ ) and average blade height across impeller ( $\bar{b}$ ) can be calculated from Equation (2.28) and (2.29) respectively [23].

$$\Delta P_{CL} = \frac{\dot{m}(r_2 C_{u2} - r_1 C_{u1})}{z \bar{r} \bar{b} L} \quad (2.27)$$

$$\bar{r} = \frac{(r_1 + r_2)}{2} \quad (2.28)$$

$$\bar{b} = \frac{(b_1 + b_2)}{2} \quad (2.29)$$

**Impeller Recirculation** Few impellers exhibit pronounced decrease in work input at low mass flow rates, this sort of behaviour is believed to be associated with recirculation of flow back into the impeller tip. Diffusion factor is calculated using Equation (2.30). The average blade loading difference is calculated using Equation (2.32). Lieblein [28] observed that blade stall occurs for impellers with diffusion factor greater than 2. Thus, a recirculation loss is calculated for impellers with diffusion factor above 2 using Equation (2.33) [23].

$$D_{eq} = \frac{W_{max}}{W_2} \quad (2.30)$$

$$W_{max} = (W_1 + W_2 + \Delta W) / 2 \quad (2.31)$$

$$\Delta W = \frac{2\pi d_2 u_2 I_B}{z L_B} \quad (2.32)$$

$$I_R = (D_{eq} / 2 - 1) [W_{u2} / C_{m2} - 2 \cot \beta_2] \quad (2.33)$$

#### CALCULATION OF THE IMPELLER INTERNAL LOSSES

Meticulous modeling of impeller internal losses is necessary to predict the performance of centrifugal compressor in close agreement with the experimental results. Ten losses that affect the performance of the impeller have been discussed in this section.

**Incidence Loss** Incidence loss can be calculated for hub, mean and shroud using (Equation (2.34) [23]). The overall incidence loss is combined using the weighted average of losses at the hub, shroud and mean surface. The mean surface is weighted ten times as high as the hub and shroud values.

$$\Delta q_{inc} = 0.4 \frac{\left( W_1 - \frac{C_{m1}}{\sin \beta_1} \right)^2}{U_2^2} \quad (2.34)$$

**Entrance Diffusion Loss** The flow adjustment from leading edge to throat has a significant effect on the performance of the impeller. An entrance diffusion loss is computed using Equation (2.35) [23] to address this phenomenon.

$$\Delta q_{DIF} = 0.4 \frac{(W_1 - W_{th})^2}{U_2^2} - \Delta q_{inc} \quad (2.35)$$

$$W_{th} = \frac{C_r}{\sin \beta_{th}} \quad (2.36)$$

**Choking Loss** The blockage in the impeller contracts the impeller throat area resulting in choking. As choking occurs at any radius, the streamlines are forced into regions of higher or lower radii where the throats has not choked. The losses associated due to the mentioned behaviour can be modeled using Equation (2.39) [23]. The contraction ratio of the impeller throat due to the blockage can be calculated using Equation (2.37) [23].

$$C_r = \frac{A_1 \sin \beta_1}{A_{th}} \quad (2.37)$$

$$x = 10 \left( 1.1 - \frac{A_{th}^*}{C_r A_{th}} \right) \quad (2.38)$$

$$\Delta q_{CH} = \frac{\left(\frac{W_1}{U_2}\right)^2 (0.05x + x^7)}{2} \quad (2.39)$$

**Shock Loss** Formation of shock on the impeller results in boundary layer separation, forming a huge wake downstream of the shock. The losses encountered due to the formation of shock can be modeled using Equation (2.40) [29].

$$\Delta q_{sh} = 1 - \left( \frac{W_{th}}{W_1} \right)^2 - \frac{2}{(\gamma - 1) M_{r1}^2} \left[ \left( \frac{P_{th}}{P_1} \right)^{\frac{\gamma-1}{\gamma}} - 1 \right] \quad (2.40)$$

**Skin Friction Loss** The loss generated due to the flow of viscous fluid over the impeller surface is termed as skin friction loss or wall friction loss. This loss can be modelled using Equation ((2.41) [23]).

$$\Delta q_{SF} = \frac{2c_f \left( \frac{\bar{W}}{U_2} \right)^2 L_B}{d_H} \quad (2.41)$$

$$\bar{W} = \frac{W_1^2 + W_2^2}{2} \quad (2.42)$$

**Skin Friction Coefficient** Skin friction coefficients are correlated as a function of Reynolds number ( $Re$ ). Reynolds Number for an impeller can be calculated using Equation (2.43).

$$Re = \frac{\rho W d_H}{\mu} \quad (2.43)$$

where  $d_H$  represents the Hydraulic diameter of the impeller, which can be calculated using Equation (2.44) [30]).

$$d_H = \frac{\frac{\pi}{2} \cos(\theta_{m1}) (D_{1shroud}^2 - D_{1hub}^2)}{\pi \cos(\theta_{m1}) (D_{1tip} + D_{1hub}) + 2z(D_{1tip} - D_{1hub})} + \frac{\pi D_2 b_2 \cos(\theta_2)}{\pi D_2 \cos(\theta_2) + z b_2} \quad (2.44)$$

Two well-defined models are used to determine the skin friction coefficient. For  $Re < 2000$ , Equation (2.45) is used to calculate the skin friction coefficient as the flow is laminar. For  $Re > 2000$ , Equation (2.46) is used to calculate the skin friction coefficient as the flow is turbulent [27].

$$c_f = 16/Re \quad (2.45)$$

$$\frac{1}{\sqrt{4c_f}} = -2 \log_{10} \left[ \frac{e}{3.71d} \right] \quad (2.46)$$

**Blade Loading Loss** The blade-to-blade pressure gradient produces secondary flows, which potentially leads to a stall. This loss phenomenon is termed as Blade loading loss, which can be determined using Equation (2.47) [23].

$$\Delta q_{BL} = \frac{\left( \frac{\Delta W}{U_2} \right)^2}{48} \quad (2.47)$$

**Hub to Shroud Loading Loss** The losses associated due to pressure gradient along hub to shroud direction can be determined using Equation (2.48) [23].

$$\Delta q_{HS} = \frac{\left( \frac{\bar{k}\bar{b}\bar{W}}{U_2} \right)^2}{12} \quad (2.48)$$

$$\bar{k} = \frac{\alpha_{c2} - \alpha_{c1}}{L} \quad (2.49)$$

$$\bar{b} = \frac{b_1 - b_2}{2} \quad (2.50)$$

$$\bar{W} = \frac{W_1 + W_2}{2} \quad (2.51)$$

**Discharge Profile Distortion Loss** The losses associated due to mixing of distorted meridional velocities can be evaluated using Equation (2.52) [23].

$$\Delta q_\lambda = 0.5(\lambda - 1)^2 \phi_2^2 \quad (2.52)$$

**Clearance Loss** The leakage of flows from compressor exit through the clearance gaps between impeller disk and shaft is accounted using Equation (2.53). The pressure difference across the gap ( $\Delta P_{CL}$ ) and the clearance gap leakage mass flow rate ( $\dot{m}_{CL}$ ) is calculated using Equation (2.27) and (2.25) respectively [23].

$$\Delta q_{CL} = \frac{\dot{m}_{CL} \Delta P_{CL}}{\dot{m} \rho U_2^2} \quad (2.53)$$

**Wake Mixing Loss** The losses associated due to the mixing of free stream flow with blade wake flow is termed as wake mixing loss. Wake mixing loss is calculated using Equation (2.54) [23].

$$\Delta q_{MIX} = 0.5 \left[ \frac{(W_{SEP} - W_{OUT})}{U_2} \right]^2 \quad (2.54)$$

$$W_{SEP} = W_2; D_{eq} \leq 2 \quad (2.55)$$

If  $D_{eq}$  is greater than two, flow separation will occur inside the blade passage, thus free stream velocity can be  $W_{SEP}$  is calculated using Equation (2.56).

$$W_{SEP} = \frac{W_2 D_{eq}}{2}; D_{eq} > 2 \quad (2.56)$$

$$W_{OUT}^2 = \left[ \frac{C_{m2} A_2}{\pi d_2 b_2} \right]^2 + W_u^2 \quad (2.57)$$

### 2.4.2. MEANLINE VANELESS DIFFUSER PERFORMANCE ESTIMATION

The vaneless diffuser is the simplest component in a centrifugal compressor, where the working fluid is decelerated to gain static pressure. The non-dimensional loss parameters for the vaneless diffuser is converted into total pressure loss using Equation (2.58) [29].

$$\Delta P_{03} = (P_{02} - P_2)\Sigma\Delta q \quad (2.58)$$

The actual total pressure at vaneless diffuser exit is the difference between the ideal total pressure at vaneless diffuser exit and the total pressure loss. The actual total pressure at the vaneless diffuser exit is calculated using Equation (2.59).

$$P_{03actual} = P_{03ideal} - \Delta P_{03} \quad (2.59)$$

**Skin Friction Loss** Losses associated due to skin friction in vaneless diffuser is determined using Equation (2.60) [27].

$$\Delta q_{sf} = 4c_f \left( \frac{\bar{C}}{C_2} \right)^2 \frac{(r_3 - r_2)}{d_H} \quad (2.60)$$

$\bar{C}$  is the average absolute velocity across vaneless diffuser and is calculated using Equation (2.61). Hydraulic diameter for vaneless diffuser is determined using Equation (2.62).

$$\bar{C} = \frac{C_2^2 + C_3^2}{2} \quad (2.61)$$

$$d_H = 0.5 \left( \frac{2r_2}{b_2} + \frac{2r_3}{b_3} \right) \quad (2.62)$$

**Diffusion Loss** The losses during diffusion process can be estimated using Equation (2.63) [29]. This equation utilizes a correlation for momentum thickness with diffusion ratio as the driving parameter.

$$\Delta q_{df} = -2(1 - E) \left( \frac{C_3 - C_2}{\rho_2 C_2} \right) \quad (2.63)$$

$E$  is the diffusion efficiency which can be calculated using Equation (2.64) [27].  $D_m$  is Equation (2.64) is the divergence parameter is an empirical factor, derived from comparison between predicted and measured loss data for various compressor stages.

$$\begin{aligned} E &= 1; D \leq 0 \\ E &= 1 - 0.2(D/D_m)^2; 0 < D < D_m \\ E &= 0.8\sqrt{(D_m/D)}; D \geq D_m \\ D &= b_2 \left( \frac{\frac{r_2 b_2}{r_3 b_3} - 1}{L} \right) \\ D_m &= 0.4(b_1/L)^{0.35} \sin \alpha_2 \end{aligned} \quad (2.64)$$

### 2.4.3. MEANLINE VANED DIFFUSER PERFORMANCE ESTIMATION

The losses in the vaned diffuser can be categorized as losses in vaneless space and losses in vaned space. The losses in vaneless space can be predicted using equations mentioned in Paragraph (2.4.2). The non-dimensional loss parameters are converted into total pressure loss as described mathematically using (Equation (2.65) [29]). The inlet conditions to vaned diffuser are equal to the *actual* exit conditions of vaneless space.

$$\Delta P_{04} = (P_{03} - P_3)\Sigma\Delta q \quad (2.65)$$

**Skin Friction Loss** Losses due to friction of viscous fluid across vaned diffuser can be estimated using Equation (2.66) [29].  $2\delta/d_H$  is the boundary layer approximation which can be calculated using Equation (2.67) [27].

$$\Delta q_{sf} = 4c_f \left( \frac{\bar{C}}{C_3} \right)^2 \frac{L_B/d_H}{(2\delta/d_H)^{0.25}} \quad (2.66)$$

$$\frac{2\delta}{d_H} = \frac{5.142c_f L_B}{d_H} \quad (2.67)$$

**Blockage Loss** Losses due to blockage for a vaned diffuser can be evaluated using Equation (2.68) [27].

$$\Delta q_{ex} = \left[ \frac{(\lambda - 1)c_{r4}}{C_4} \right]^2 \quad (2.68)$$

**Wake Mixing Loss** The losses associated due to mixing of wake from vanes with main stream flow can be estimated using Equation (2.69) [27].

$$\begin{aligned} C_{SEP} &= \frac{C_3}{1 + 2C_\theta} \\ C_\theta &= 2\theta_c/11.0 \\ C_{m,wake} &= \sqrt{(C_{SEP}^2 - C_{U4}^2)} \\ C_{m,mix} &= \frac{A_4 C_{m4}}{2\pi r_4 b_4} \\ \Delta_{mix} &= \left[ \frac{C_{m,wake} - C_{m,mix}}{C_3} \right]^2 \end{aligned} \quad (2.69)$$

## 2.5. OVERALL STAGE PREDICTIONS

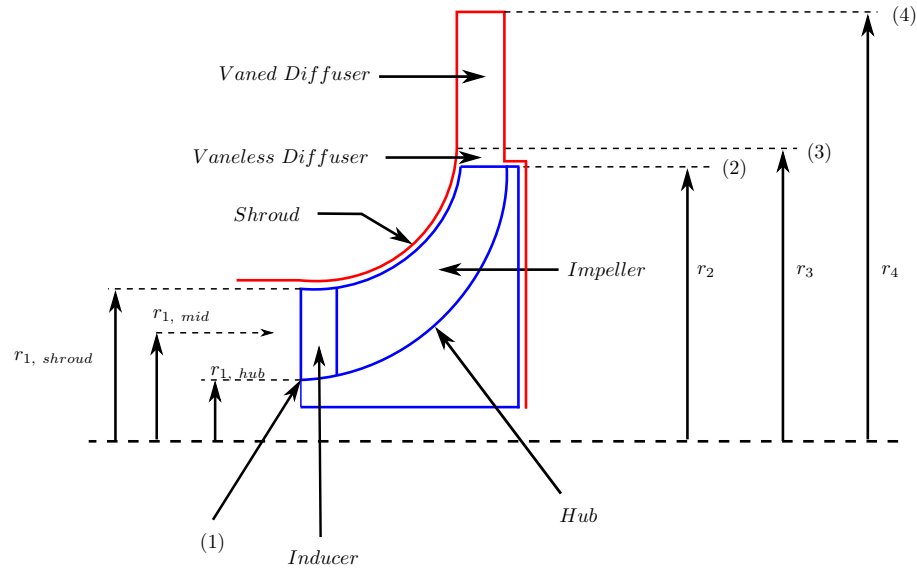


Figure 2.14: Meridional View of the Centrifugal Compressor

The analysis begins with the definition of the ambient conditions and the geometrical parameters of each compressor component. Turbomachinery relations were used to determine the ideal flow properties across the impeller. The actual flow properties across the impeller are determined by estimating the losses across the impeller, which are then fixed as the inlet conditions for the vaneless diffuser. Conservation of mass; momentum and energy, the equation of state are solved to determine the ideal flow properties across the

vaneless and the vaned diffuser. Evaluating losses across the vaneless and the vaned diffuser will assist in determining the actual flow properties across these components. Section (2.5.1), (2.5.2), and (2.5.3) will elaborate the overall stage prediction method in detail. Figure (2.14) shows the meridional view of the centrifugal compressor along with the labels for various stations. Figure (2.15) illustrates the schematic of procedures followed to predict the overall stage performance of the MTT compressor.

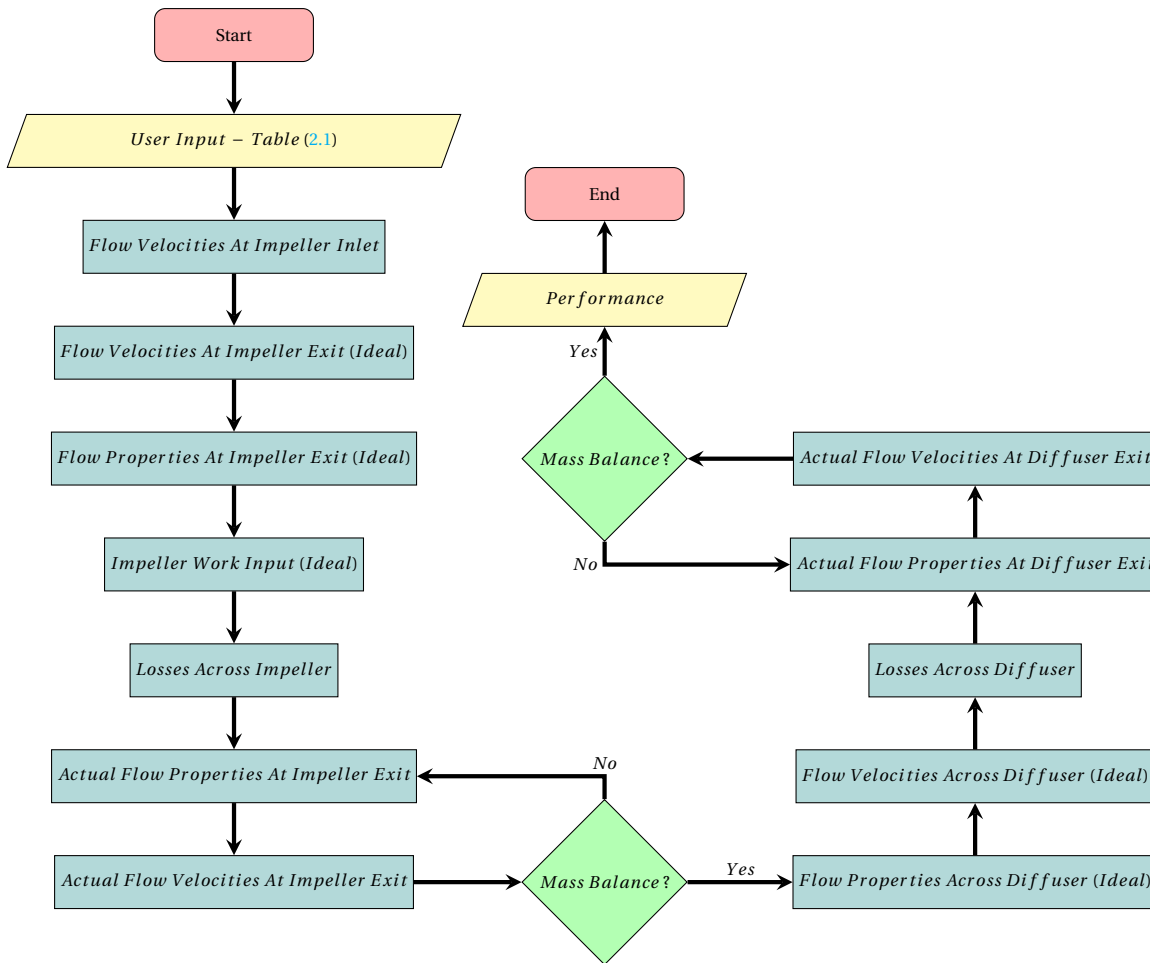


Figure 2.15: Flow Chart of the Compressor Performance Analysis

### 2.5.1. IMPELLER MODEL

The performance prediction of the impeller begins with the definition of the total flow properties at the inlet of the impeller and the geometrical parameters of the impeller. Table (2.1) illustrates the total flow properties at the inlet and the geometrical parameters of MTT impeller to evaluate its performance. The Static flow properties at the inlet (station - 1) of the impeller are then determined by solving the equation of state (2.70), continuity equation (2.71), and stagnation enthalpy equation (2.72) in an iterative fashion until convergence is achieved.

$$P_1 = \rho_1 R T_1 \quad (2.70)$$

$$\dot{m}_1 = \rho_1 A_1 C_{m1} \quad (2.71)$$

$$H_{01} = h_1 + \frac{C_{m1}^2}{2} \quad (2.72)$$

The flow and blade velocities at the inlet (station - 1) of the impeller (i.e., the inducer), are determined using turbomachinery relations derived from velocity triangles. Turbomachinery relations derived from H-S

diagram (2.2) are evaluated to determine the ideal flow properties at the outlet (station - 2) of the impeller. Equations illustrated under Section (2.4.1) are utilized to determine the actual flow properties and the geometrical parameters at the outlet of the impeller.

Table 2.1: Flow Properties and Geometrical Parameters used to predict MTT impeller performance

Flow Properties and Geometrical Parameters	Value	Units
Total Temperature, $T_{01}$	296.4	[K]
Total Pressure, $P_{01}$	0.96	[bar]
Mass Flow Rate, $\dot{m}_1$	0.055	[kg/s]
Radius at Inducer Hub, $r_{1,hub}$	4.5	[mm]
Radius at Inducer Shroud $r_{1,shroud}$	12.9	[mm]
Impeller Shroud Clearance	0.0	[mm]
Rotations per Minute, $RPM$	$24e^4$	[-]
Pre-Whirl Angle at Inducer Hub	0.01	[deg]
Pre-Whirl Angle at Inducer Mid	0.01	[deg]
Pre-Whirl Angle at Inducer Shroud	0.01	[deg]
Impeller Back Sweep Angle, $\beta_2$	43.0	[deg]
Impeller Tip Radius, $r_2$	18.5	[deg]
Vaneless Diffuser Exit Radius, $r_3$	35.23	[mm]
Number of Blades, $z$	12	[-]
Length of Impeller, $L_B$	21	[mm]
Clearance between Impeller and Diffuser, $s$	0.5	[mm]
Roughness	$1e^{-2}$	[mm]
Impeller Blade Thickness At Eye	0.5	[mm]
Impeller Blade Thickness At Exit	0.5	[mm]
Inducer Inlet Angle at Hub, $\beta_{1,hub}$	45.5	[deg]
Inducer Inlet Angle at Mid, $\beta_{1,mid}$	55	[deg]
Inducer Inlet Angle at Tip, $\beta_{1,tip}$	64.5	[deg]

### 2.5.2. VANELESS DIFFUSER MODEL

The performance prediction for vaneless diffuser commences after predicting the actual flow properties at the outlet of the impeller. Due to the simplicity of the vaneless diffuser design, radius ( $r_3$ ) and axial width ( $b_3$ ) are the only geometrical parameter required to evaluate its performance. However for some diffusers the axial width is varied radially. In that case an additional angle is required to design the vaneless diffuser. For the MTT compressor, the vaneless diffuser axial width at the outlet ( $b_3$ ) is not equal to the axial width at the inlet ( $b_2$ ), due to a pinch. For simplicity, pinch is not considered for one-dimensional performance analysis. The geometrical parameter used to evaluate vaneless diffuser performance is shown in Table (2.1). Conservation of angular momentum (2.73); mass (2.74); stagnation enthalpy (2.75), the equation of state (2.70), and the isentropic relation (2.76) are utilized to determine the ideal flow properties at the outlet (station - 3) of the diffuser. The actual flow properties at the outlet (station - 3) of the vaneless diffuser are then determined by predicting losses using equations mentioned under Section (2.4.2).

$$r_2 C_{\theta 2} = r_3 C_{\theta 3} \quad (2.73)$$

$$\rho_2 A_2 C_{m2} = \rho_3 A_3 C_{m3} \quad (2.74)$$

$$h_2 + \frac{C_{m2}^2 + C_{\theta 2}^2}{2} = h_3 + \frac{C_{m3}^2 + C_{\theta 3}^2}{2} \quad (2.75)$$

$$\frac{T_{03}}{T_3} = \left[ \frac{\rho_{03}}{\rho_3} \right]^{\frac{1}{\gamma-1}} \quad (2.76)$$

### 2.5.3. VANED DIFFUSER MODEL

The evaluation of throat area at the vaned diffuser inlet is the single most important step while designing the vaned diffuser, as mentioned in Section (2.3.2). Equation (2.77), (2.78) and (2.79) [31] are utilized to determine the throat area ( $A_d^*$ ) at the vaned diffuser inlet.

$$\phi_{t1}^i = \frac{1}{M_{u2}} \frac{A_i^*}{D_2^2} \frac{\left[1 + \frac{\gamma-1}{2} \left(\frac{D_1}{D_2}\right)^2 M_{u2}^2\right]^{\frac{\gamma+1}{2(\gamma-1)}}}{[(\gamma-1)/2]^{\frac{\gamma+1}{2(\gamma-1)}}} \quad (2.77)$$

$$\phi_{t1}^d = \frac{1}{M_{u2}} \frac{A_d^*}{D_2^2} \frac{\left[1 + (\gamma-1)\lambda M_{u2}^2\right]^{\frac{\gamma+1}{2(\gamma-1)}}}{[(\gamma-1)/2]^{\frac{\gamma+1}{2(\gamma-1)}}} \quad (2.78)$$

$$\phi_{t1}^i = \phi_{t1}^d \quad (2.79)$$

The ideal and actual flow properties at the outlet (station - 4) of the vaned diffuser can be evaluated using equations mentioned under Section (2.5.2) and (2.4.3) respectively.

## 2.6. MODEL VERIFICATION AND VALIDATION

This section shows the numerical results of the MTT centrifugal compressor computed using one-dimensional performance analysis tool. The geometrical details of the compressor along with the inlet flow conditions can be found in Table (2.1). The performance of the MTT compressor is calculated for RPM varying from 220k up to 240k. RPM 220k is the best efficiency point and RPM 240k is the current operating point of the MTT compressor. Later, the one-dimensional results of MTT compressor are validated against the existing experimental results to determine the accuracy of the one-dimensional performance analysis tool. Finally, The significance of the pre-whirl and the vaned diffuser on the performance of the compressor is presented in this section.

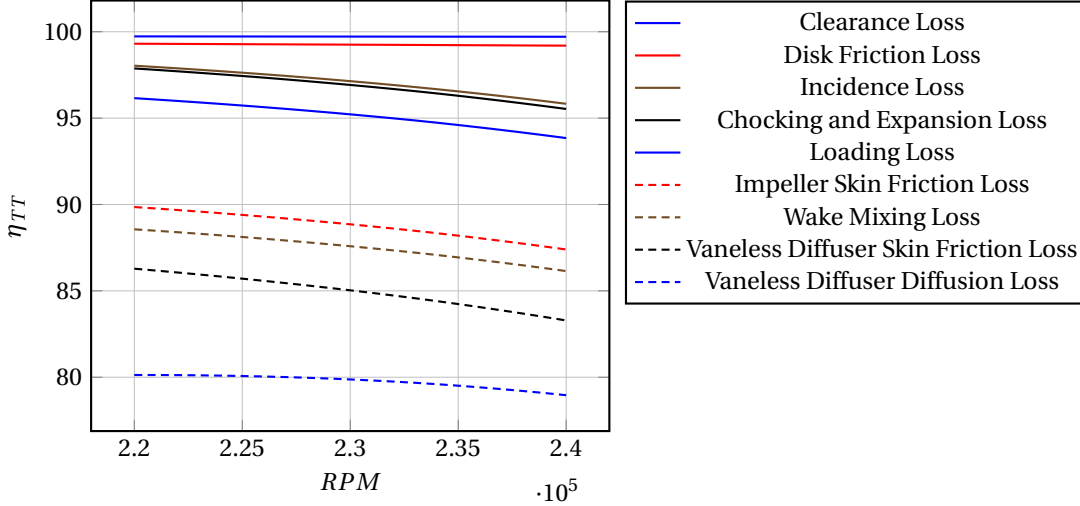


Figure 2.16: Performance of MTT Compressor for different RPM varying from 220k up to 240k

**Performance of MTT Compressor** The Total-to-Total efficiency of MTT compressor along with the losses are plotted for RPM varying from 220k up to 240k as shown in Figure (2.16). It can be observed that the impeller skin friction loss plays a dominant role in reducing compressor's performance followed with vaneless diffusion loss, vaneless skin friction loss, and incidence loss. Reduction in impeller's skin friction loss can be achieved by reducing the mean streamline length of the impeller. As discussed in Section (2.3.2), an increase in compressor efficiency can be achieved by incorporating a vaned diffuser instead of a vaneless diffuser at the expense of restriction in operating range. The significance of vaned diffuser on compressor's performance with respect to vaneless diffuser will be evaluated later in this section.

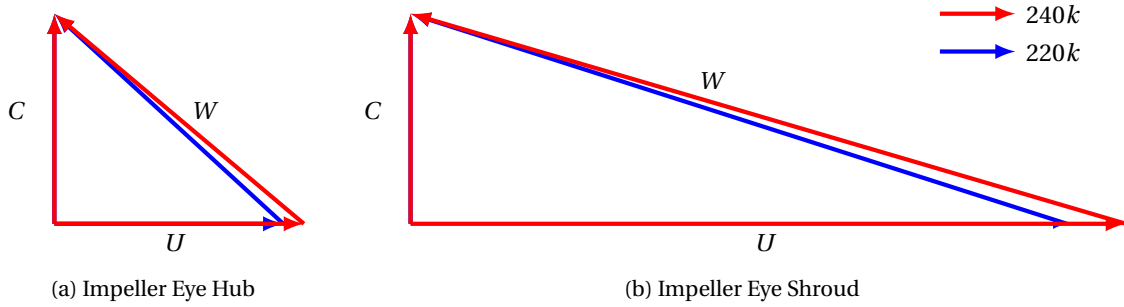


Figure 2.17: Velocity Triangles at impeller inlet for 220k and 240k RPM

The contribution of incidence loss in reducing compressor's performance at 220k RPM is lower when compared to 240k RPM. This scenario can be better understood from velocity triangles at impeller inlet for 220k and 240k RPM, as shown in Figure (2.17). Increase in RPM results in increasing the relative flow angle at the impeller inlet ( $\beta_1$ ), causing more incidence losses. In general, incidence losses occur when the compressor operates at off-design conditions, whereas for MTT compressor the contribution of losses due to incidence is significant at the design point. The primary reason for such a behaviour is due to the fact that MTT compressor uses an off the shelf impeller design. Improvement in performance can be achieved by incorporating inlet guide vanes at the compressor inlet. The flow physics of the inlet guide vanes and their significance on the performance of the MTT compressor will be discussed later in this section. All the other losses play a minor role in reducing the performance of the compressor. Nevertheless, the magnitude change of these losses for an optimised impeller will be evaluated in Chapter (3).

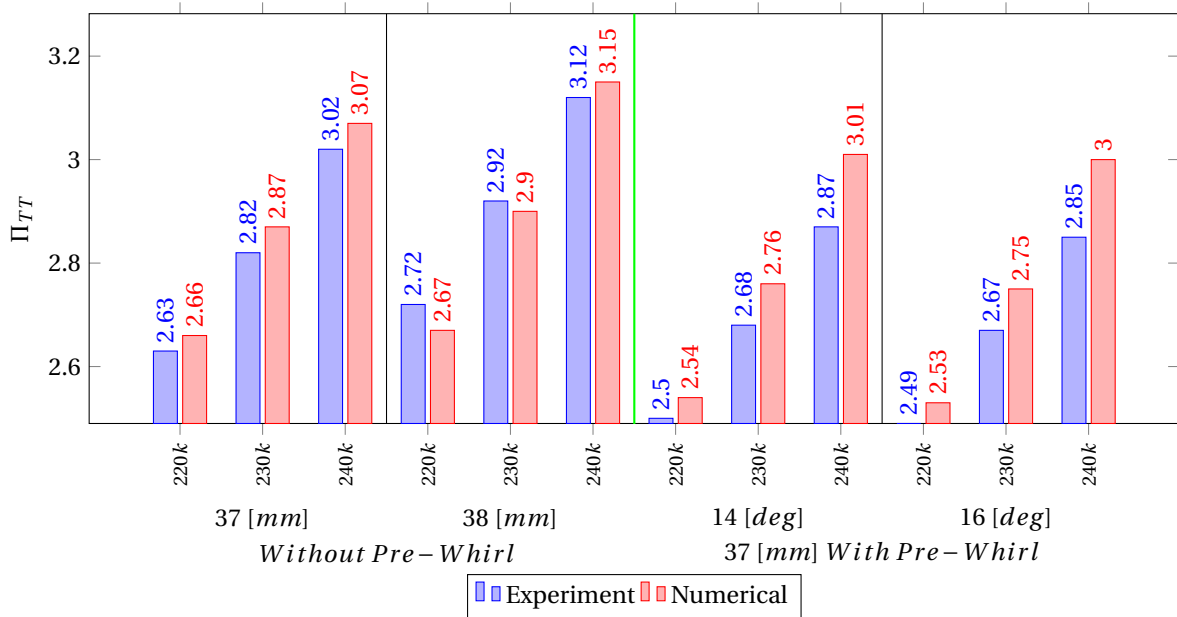


Figure 2.18: Comparison of the Stage Total-to-Total Pressure Ratio between Experimental and Numerical Results at 220k, 230k, and 240k rpm for Two different Impeller Design with and without Pre-Whirl

**Model Validation** Figure (2.18) and (2.19), shows the comparison of Total-to-Total pressure ratio and Total exit temperature between the experimental and numerical results, at 220k, 230k and 240k for two different impellers without pre-whirl and for one impeller with and without pre-whirl. The experimental results were obtained from MTT. The meridional shape of two impellers used for the analysis is shown in Figure (2.20).

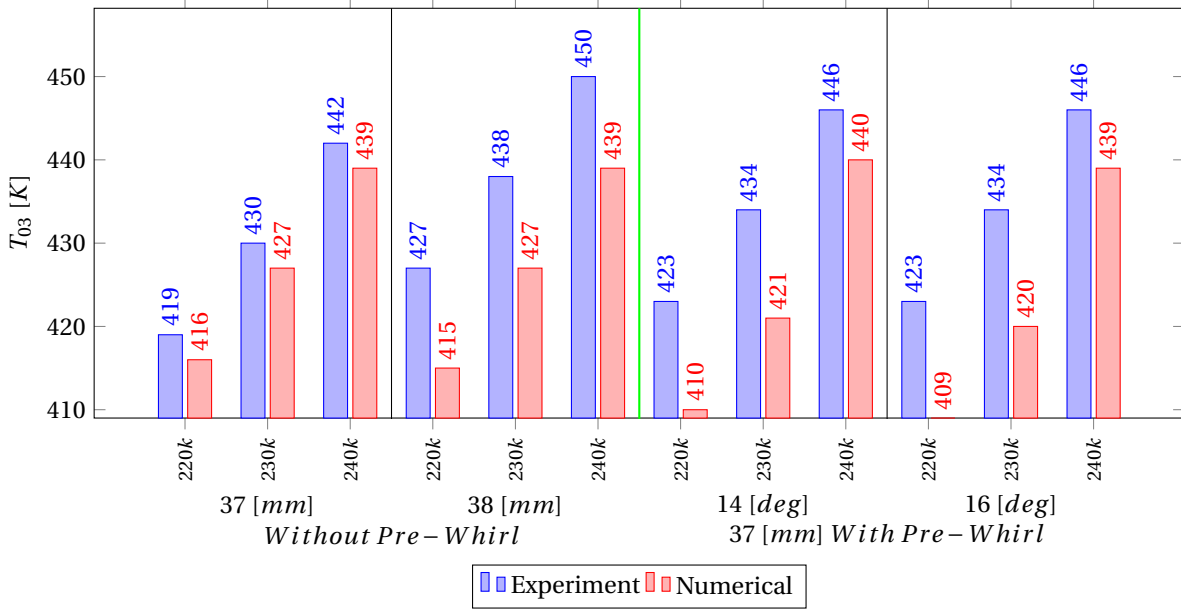


Figure 2.19: Comparison of the Stage Exit Total Temperature between Experimental and Numerical Results at 220k, 230k, and 240k rpm for Two different Impeller Design with and without Pre-Whirl

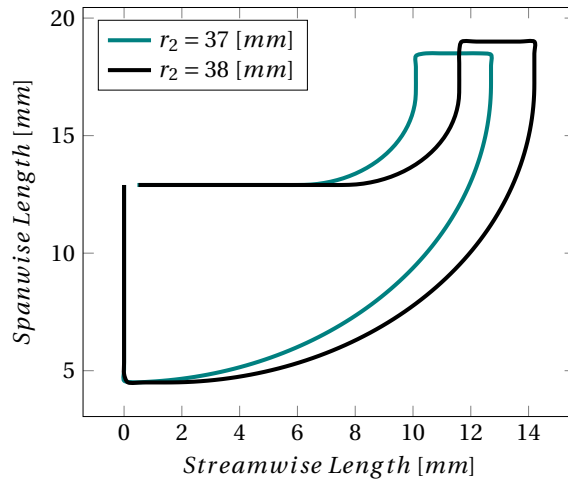


Figure 2.20: Meridional Shape of Impellers used for Experimental and Numerical Analysis

Table 2.2: Inlet Flow Properties at which Numerical and Experimental Results were Performed for two impeller without pre-whirl and for one impeller with pre-whirl

	Without Pre-Whirl		With Pre-Whirl (37[mm])		Units
	37 [mm]	38 [mm]	14 [deg]	16 [deg]	
Total Pressure	0.98	0.99	1.017	1.017	[bar]
Total Temperature	296	297	303	303	[K]

The inlet flow properties at which these experiments were performed is listed in Table (2.2). The numerical results were computed using one-dimensional model described under this Chapter. It can be observed that the one-dimensional performance prediction tool marginally over predicts pressure ratio when compared to experimental results. The maximum percentage difference in estimation of the pressure ratio in comparison to experimental results is  $\approx 5\%$ . The maximum percentage difference in estimation of the exit

total temperature in comparison to experimental results is  $\approx 3\%$ . It is important to mention that the experimental data has been obtained for the complete turbocharger compressor, whereas the 1D analysis and 3D analysis comprises of the impeller and the diffuser only. The volute has not been modelled for 1D and 3D analysis. The inclusion of volute in the performance prediction tool might further narrow the difference between the actual and the predicted values.

**Effect of Inlet Guide Vanes on Compressor Performance** The inlet guide vanes provide tangential velocity to the flow at the inlet resulting in either increasing or decreasing the inlet relative velocity. Providing a positive absolute tangential velocity (absolute tangential velocity along the direction of rotation) using inlet guide vanes is termed as positive pre-whirl. Negative pre-whirl produces an absolute tangential velocity in a direction opposite to that of the impeller's rotation. The variation in velocity triangles at the inlet of impeller hub due to positive and negative pre-whirl is shown in Figure (2.21). It can be observed that producing positive pre-whirl at the inlet of the impeller results in reducing relative flow angle at the inlet. This will increase the performance of the compressor by reducing losses due to incidence. On contrary, producing negative pre-whirl at the inlet of impeller increases the relative flow angle at the inlet. This may further deteriorate the performance of the compressor and might also lead to a stall.

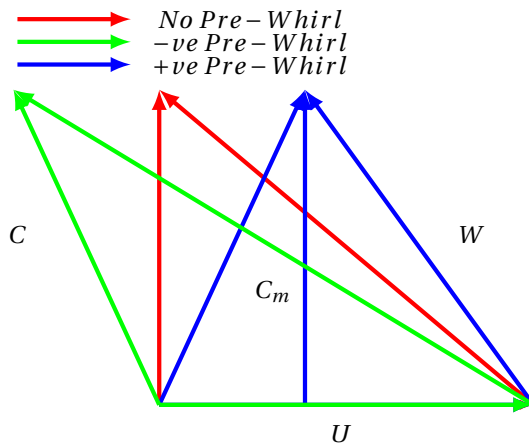


Figure 2.21: Velocity Triangle at Impeller Hub with a Positive and Negative Pre-Whirl of 25 [deg] for MTT Compressor at 240k RPM

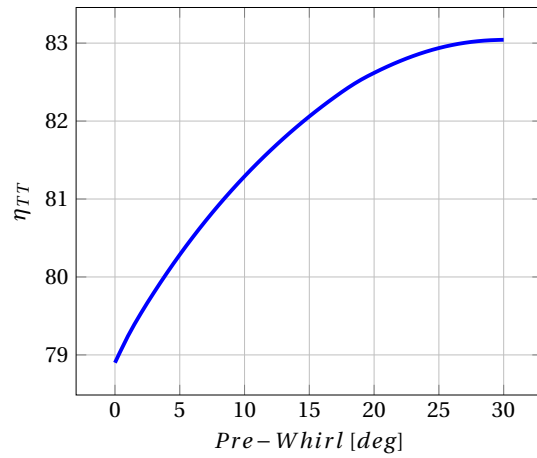


Figure 2.22: Variation in Total-to-Total Efficiency of MTT Compressor with Positive Pre-Whirl at 240k RPM

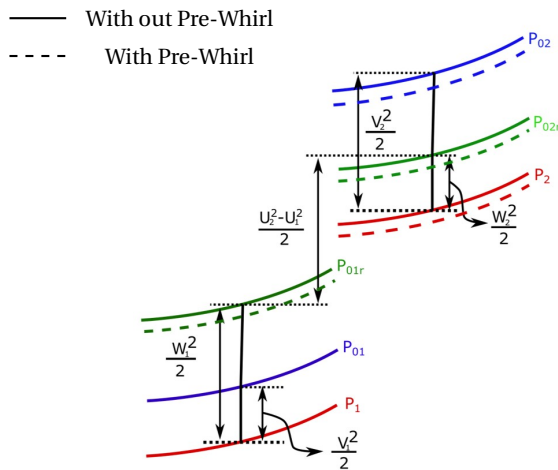


Figure 2.23: H-S Diagram of an Ideal MTT Compressor with and without Pre-Whirl

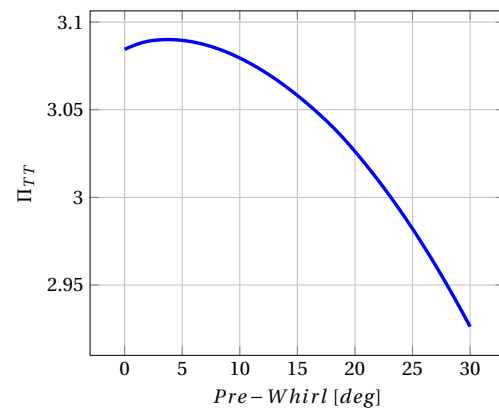
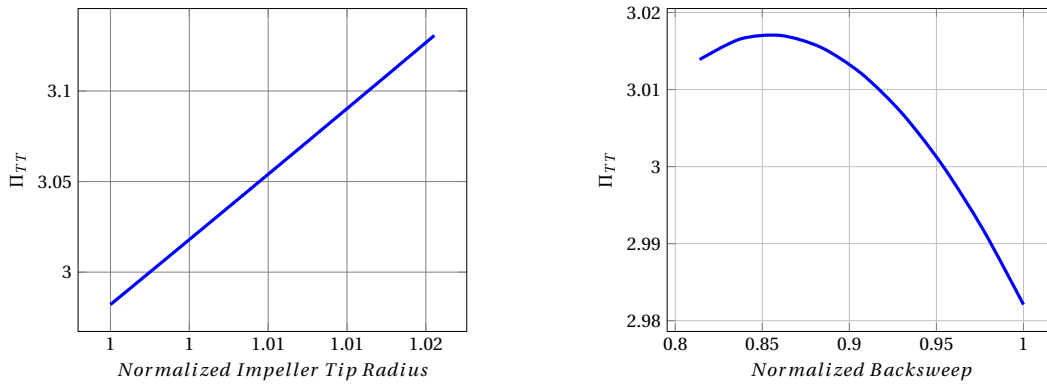


Figure 2.24: Variation in Total-to-Total Pressure Ratio of MTT Compressor with Positive Pre-Whirl at 240k RPM

The performance of MTT compressor operating at 240k RPM is analysed by providing a positive pre-whirl at impeller inlet. Figure (2.22) illustrate the change in Total-to-Total efficiency of MTT compressor

while varying pre-whirl from 0 to 30 [deg].  $\approx 5\%$  gain in Total-to-Total efficiency can be achieved for MTT compressor if a pre-whirl of 25 [deg] is applied at the inlet of the impeller. The only drawback associated with positive pre-whirl is the reduction in delivery pressure at the compressor exit. This phenomenon can be understood from Equation (2.8). Due to positive pre-whirl, the right-hand term  $U_1 C_{u1} / U_2^2$  in Equation (2.8) is no longer zero, resulting in reduced energy transfer from impeller on working fluid. Figure (2.23) illustrates the reduction in enthalpy rise across the compressor due to positive pre-whirl.  $\approx 2.5\%$  reduction in delivery pressure is observed for MTT compressor with a positive pre-whirl of 25[deg], as shown in Figure (2.24). The drawback due to positive pre-whirl can be shadowed by either increasing the impeller’s tip radius or by reducing the impeller’s back sweep.

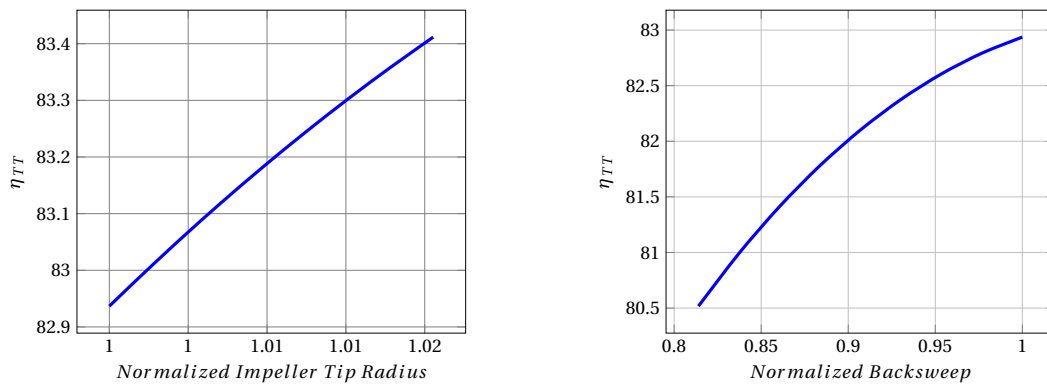
Figure (2.25) and (2.26), illustrates the impact of increasing impeller tip radius; decreasing impeller back sweep on  $\Pi_{TT}$  and  $\eta_{TT}$  of MTT compressor with a positive pre-whirl of 25 [deg] at inlet of compressor. The geometrical parameters impeller tip radius and impeller backsweep are normalized with existing design values, shown in Table (2.1). It can be observed from Figure (2.25), that the reduction in delivery pressure due to pre-whirl can be compensated by either increasing the impeller tip radius by  $\approx 1\%$  or by decreasing the impeller back sweep by  $\approx 8\%$ .



(a) Variation of  $\Pi_{TT}$  with increasing Impeller Tip Diameter (b) Variation of  $\Pi_{TT}$  with decreasing Back Sweep

Figure 2.25: Variation of  $\Pi_{TT}$  by either increasing impeller tip diameter or by decreasing backsweep for MTT compressor with 25 [deg] positive pre-whirl

Decreasing impeller back sweep has negative impact on compressor’s performance as shown in Figure (2.26b). The primary reason for such a behaviour is the increase in losses due to wake mixing at impeller exit. The performance of the compressor has increased gradually by changing impeller tip radius, as shown in Figure (2.26a).



(a) Variation of  $\eta_{TT}$  with increasing Impeller Tip Diameter (b) Variation of  $\eta_{TT}$  with decreasing impeller back sweep

Figure 2.26: Variation of  $\eta_{TT}$  by either increasing impeller tip diameter or by decreasing backsweep for MTT compressor with 25 [deg] positive pre-whirl

**Effect of Vaned Diffuser on Compressor Performance** The performance of MTT compressor with the vaneless diffuser and the vaned diffuser is evaluated in this paragraph. Figure (2.27) shows the schematic of channel shaped vaned diffuser used for the meanline analysis. To compare the performance of MTT compressor with a vaneless diffuser and with a vaned diffuser, the static pressure at the diffuser exit is kept constant for both the diffusers. As the vaneless diffusion process is considered less efficient, reducing the vaneless space ratio increases the efficiency of the compressor. However, the least possible vaneless space ratio for MTT compressor design is 1.10 due to geometrical constraints, hence the same was considered for one-dimensional analysis. Figure (2.28) illustrates the variation in MTT Compressor Efficiency for different vane divergence angle. It can be observed that the vaned diffuser performance poorly at low divergence angle due to increased wake-mixing loss at vaned diffuser exit. At high divergence angle ( $\theta_c > 5.5$  [deg]) [27], the possibility of flow separating from vane surface increases resulting in losses, which is not captured by the one-dimensional performance prediction tool. Figure (2.29) shows the variation in efficiency of MTT compressor with and without pre-whirl; with and without vaned diffuser. Vane divergence angle ( $\theta_c$ ) of 8 [deg] was considered for the analysis. It was observed that  $\approx 6\%$  increase in compressor efficiency was obtained by replacing vaneless diffuser with vaned diffuser in existing compressor assembly. However, a three dimensional analysis is performed in Chapter (5) to verify the meanline model results, as the one-dimensional model is incapable of predicting the losses due to flow separation across the vaned diffuser channel.

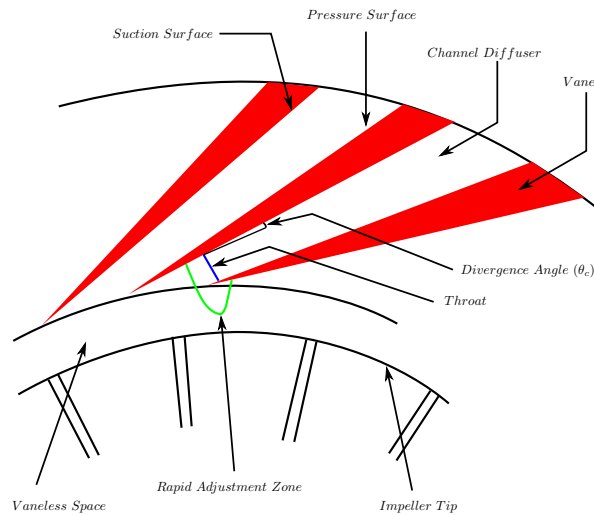


Figure 2.27: The schematic of Channel Shaped Vaned Diffuser

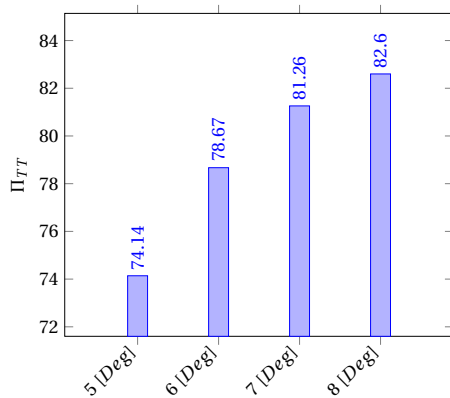


Figure 2.28: Variation in MTT compressor performance with different Divergence Angle ( $\theta_c$  for Vaned Diffuser)

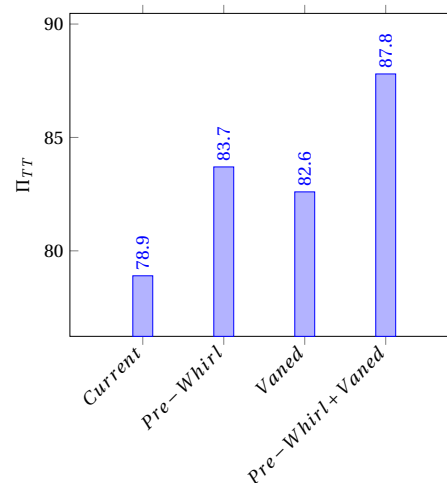


Figure 2.29: Efficiency of MTT compressor with and without pre-whirl; with and without vaned diffuser ( $\theta_c = 8$  [deg])

# 3

## MEAN LINE COMPRESSOR PERFORMANCE OPTIMIZATION

In this chapter, the optimisation of the impeller has been performed by coupling a gradient-based algorithm and an evolutionary algorithm with the meanline tool described in the previous chapter. The geometrical parameters namely the impeller hub radius, ratio of impeller shroud to tip radius, ratio of diffuser inlet to exit radius, and impeller blade back sweep angle have been selected as the design variables for optimisation of the compressor with a vaneless diffuser. In the case of optimising a compressor with vaned diffuser additional two geometrical parameters namely, the position of the vanes with respect to impeller tip and the vane divergence angle have been chosen for the optimisation. The maximisation of compressors' Total-to-Total and Total-to-Static efficiency for a user defined static pressure recovery have been chosen as an objective function.

### 3.1. INTRODUCTION

The most challenging step for a design engineer during a design process is to determine an optimum design satisfying all the design requirements (design constraints). An Optimum design is usually achieved through optimisation, a mathematical process that produces maximum or minimum value for a specified function while meeting all the design requirements. In the case of MTT centrifugal compressor optimisation, maximisation of compressor's performance or minimization of compressor's losses is the objective function and the optimisation constraints are the static pressure recovery and geometrical limitations.

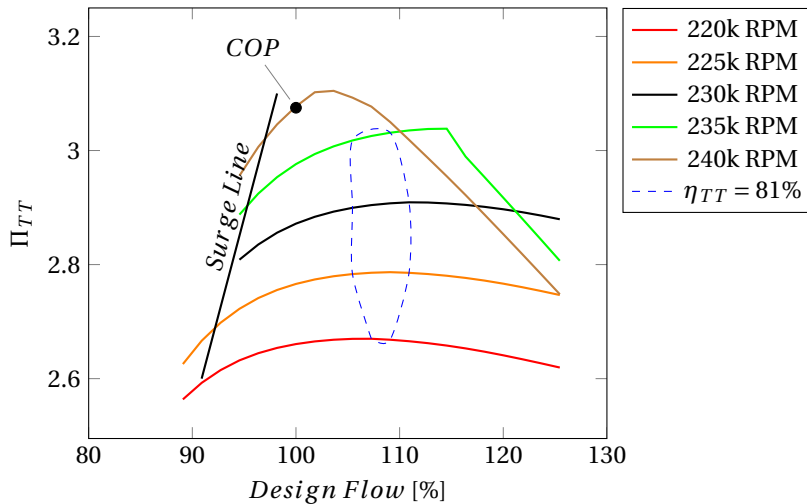


Figure 3.1: MTT Compressor Performance Map

Figure (3.1), shows the performance map of the existing MTT compressor. The operating range for which current MTT compressor provides the highest efficiency is represented using a blue dashed line. It can be ob-

served that the MTT current operating point (COP) is near surge line and far away from maximum efficiency region. Performing an optimisation on MTT compressor will allow to determine the compressor's geometrical parameters at which maximum efficiency can be achieved for COP.

Before presenting and discussing the results of the optimisation, an overview of the general optimisation problem is presented, followed by the optimisation techniques adopted in this work.

### 3.2. OPTIMISATION PROBLEM STATEMENT

In this section, the specification for the overall optimisation problem is presented. Initially, a general description of the formulation employed in optimisation process is given followed with the formulation of the optimisation problem for MTT compressor.

**Problem Statement** For optimisation of MTT compressor, user defined static pressure recovery is a constraint which has to be satisfied during the optimisation process. However, incorporating this criterion within the objective function has assisted in formulating the optimisation problem without an explicit declaration of the mentioned constraints. These kinds of optimisation problems are termed as unconstrained optimisation problems. Equation (3.1) up to (3.3) states the problem statement for unconstrained optimization.

$$\text{minimize} \quad f(x), \quad (3.1)$$

$$x_{p,min} \leq x_p \leq x_{p,max} \quad (3.2)$$

$$\text{where} \quad \mathbf{X} = \begin{Bmatrix} x_1 \\ x_2 \\ \cdot \\ \cdot \\ x_n \end{Bmatrix} \quad (3.3)$$

The above stated optimisation problem consider only one objective function, hence can be termed as single-objective optimisation formulation. However, some applications require simultaneous minimization of several objective functions  $f_i(x)$ , leading to a so-called multi-objective optimisation problem. In this case, conflict objective functions may exist, leading to a conundrum between two simultaneous minimizing or maximising functions. One of the simplest solutions to the above problem is the conversion of multi-objective optimisation problem into a single-objective one by considering a "pseudo-objective function"  $f(x)$  as the weighted sum of each individual objective function, as shown in Equation (3.4).  $w_i \geq 0$  are the weighting coefficients representing the importance of its objective function  $f_i(x)$ . It is usually assumed that the sum of objective functions is 1 [32].

$$f(x) = \sum w_i f_i(x) \quad (3.4)$$

For MTT compressor formulating an optimization problem with objective function as Total-to-Total efficiency or Total-to-Static efficiency results in obtaining an optimal candidate point which is dictated by bounds of design variable  $v_r$ . Thus, the optimisation problem for MTT compressor has two objective functions namely, Total-to-Total and Total-to-Static Efficiency. Hence, a multi-objective optimisation formulation was utilised. As both the objective functions are equally significant, a weighting coefficient of 0.5 was considered while formulating the optimisation problem.

**Design Vector** The set of quantities which can be viewed as variables in the design process is termed as design variables. The design variables are usually represented in a vector form known as Design Vector, as shown in Equation (3.3).

$$f(r_{1,hub}, r_{1,shroud}, r_2, r_3, N, \dot{m}, P_{01}, P_{03}, T_{01}, T_{03}, R, \gamma, \sigma) \quad (3.5)$$

The basic parameters that determine the performance of a centrifugal compressor with vaneless diffuser can be written in terms of a function as shown in Equation (3.5) [33]. MTT compressor operates on fluids obeying ideal gas law at a constant RPM of 240k and a mass flow rate of 0.055 [kg/s], hence the terms  $\dot{m}, N, R, \gamma$  in Equation (3.5) are neglected as design variables during the optimization process for MTT compressor with vaneless diffuser. As mentioned earlier, the optimisation is performed for a user defined static

pressure recovery, hence the terms  $P_{03}, T_{03}$  in Equation (3.5) cannot be considered as design variables for the optimisation. Unlike turbochargers, the variation of inlet flow properties for MTT compressor is meagre. Thus the terms  $P_{01}, T_{01}$  in Equation (3.5) can also be neglected as the design variables for the optimization process. The remaining terms in Equation (3.5) are valid design variables that are considered during the optimisation process of MTT compressor with a vaneless diffuser.

$\sigma$  in Equation (3.5) is a function of blade back sweep angle ( $\beta_2$ ), hence  $\sigma$  is replaced by  $\beta_2$  as a design variable. The number of design variables plays a significant role in computational time, thus considering the ratio of geometrical parameters assists in reducing the design variables to 4 instead of 5. Equation (3.6) and (3.7) shows the ratio of geometrical parameters considered as design variables for optimization. Equation (3.8) represents the design variables that were considered for optimisation of MTT compressor with vaneless diffuser in a vector form. In the case of a vaned diffuser, two additional parameters namely ratio of vaneless space and divergence angle ( $\theta_c$ ) were also considered.

$$\lambda_r = \frac{r_{1,shroud}}{r_2} \quad (3.6)$$

$$v_r = \frac{r_2}{r_3} \quad (3.7)$$

$$\mathbf{X} = \begin{Bmatrix} r_{1,hub} \\ \lambda_r \\ v_r \\ \beta_2 \end{Bmatrix} \quad (3.8)$$

The design variables mentioned in Equation (3.8) have different orders of magnitude, and most of the optimising algorithms are not numerically robust to accommodate such wide variation in the magnitude of the design variables. To prevent ill-conditioning, all the design variables are normalised such that they have similar magnitudes. Equation (3.9) shows the normalized design vector used for MTT compressor optimization.

$$\hat{\mathbf{X}} = \frac{\begin{Bmatrix} r_{1,hub} \\ \lambda_r \\ v_r \\ \beta_2 \end{Bmatrix}}{\begin{Bmatrix} r_{1,hub} \\ \lambda_r \\ v_r \\ \beta_2 \end{Bmatrix}} \quad (3.9)$$

**Bounds** As mentioned in Section (3.1), bounds are the limits within which the design variables are allowed to vary during the optimisation process. The range within which the  $r_{1,hub}$  must vary depends on the structural integrity of the impeller, hence its chosen based on the experience. For MTT compressor optimization the range of  $r_{1,hub}$  was varied from 85% to 115% with respect to existing  $r_{1,hub}$  dimension. The optimal range for  $\lambda_r$  and  $v_r$  are between (0.5 to 0.7) and (0.5 to 0.7) respectively [33]. Considering values below 0.57 for  $\lambda_r$  results in the formation of shock due to reduced inlet area, as we are dealing with micro compressors. Thus  $\lambda_r$  was allowed to vary from (0.57 to 0.7) during the optimisation process. The  $v_r$  was limited to vary between 0.5 to 0.5775 in order to achieve the same or lower exit dynamic head as of the existing MTT compressor design. Optimal back sweep angle ( $\beta_2$ ) varies with impeller's discharge pressure, thus a wide range (30 to 60 [deg]) was selected during the optimisation process.

Parameters	Lower Bound	Upper Bound	Units
$r_{1,hub}$	0.95	1.3	[mm]
$\lambda_r$	0.57	0.7	[-]
$\nu_r$	0.5	0.5775	[-]
$\beta_2$	30	60	[deg]
<i>Vaneless Space Ratio</i>	1.05	1.25	[-]
$\theta_c$	4	5.5	[deg]

Table 3.1: The allowable range for the design variables during the optimisation

Similar bounds were maintained for the mentioned design variable while optimising the compressor with the vaned diffuser. The optimum range for vaneless space ratio is 1.05 to 1.25 [19] [31], thus the same was utilized as bounds for optimisation. Vane divergence angle ( $\theta_c$ ) above 5.5 [deg] results in flow separation across the vaned diffuser channel [27]. As observed in Chapter (2) the one-dimensional performance prediction tool is incapable of predicting losses due to flow separation across vaned diffuser, thus  $\theta_c$  was allowed to vary from 4 to 5.5 [deg] during the optimization process. The bounds for the design variables used in this work is summarized in Table (3.1).

### 3.3. OPTIMIZATION TECHNIQUES

Generally, optimisation methods can be categorised as local or global. Local optimisation perturbs the design variables such that the direction followed leads to minimization or maximisation of the objective function. Local optimisation provides an optimal solution only when the optimum point is located in the neighbourhood of the initial candidate point, which is provided by the user. In the case of a global optimisation, a set of several designs are simultaneously compared to each other, combined and altered so that the objective function is either minimised or maximised. Unlike local optimisation, global optimisation provides an optimal solution regardless of the position of the initial candidate point provided by the user.

Another well-known classification of optimisation techniques is stochastic optimisation and deterministic optimisation. In stochastic optimisation, the design variables are randomly created and used, whereas in deterministic optimisation the design variables are created based on the gradient information about the objective function. Classical optimisation strategies (e.g., non-linear, linear geometric, quadratic and dynamic programming), which are used to determine the optimal solution are local, deterministic methods. These methods use differential calculus in determining the optimal points, which are then sought from initial solution in an iterative fashion.

On the other hand, there are some optimisation methods which are based on certain characteristic and behaviour of biological, molecular and the swarm of insects. These methods are generally global, stochastic, as they require only the objective function to be evaluated and not their derivatives. Some of them are the evolutionary algorithm, particle swarm optimisation and colony optimisation.

For MTT compressor, optimisation was performed using both, gradient based and stochastic optimisation techniques. "Limited memory Broyden-Fletcher-Goldfarb-Shanno" (L-BFGS-B) algorithm was utilised for gradient-based optimisation and for stochastic optimisation was performed using "Differential Evolution" algorithm. A brief overview of these algorithms is presented below.

**L-BFGS-B** L-BFGS-B approximates the BFGS algorithm using a limited amount of computer memory. L-BFGS-B is a class of hill climbing optimisation technique, where the optimal point is reached when the gradient is zero. The primary difference between L-BFGS-B and BFGS algorithms is the difference in storage of hessian matrix, which is utilised to search through variable space. BFGS stores a dense  $x \times x$  hessian matrix, whereas L-BFGS-B stores only a few vectors that represent the approximation implicitly.

**Differential Evolution** Differential evolution is a stochastic population method which is utilised for global optimisation problems. The algorithm mutates each candidate solution with other candidate solutions to create a trial candidate. There are several strategies available to determine the trial point. For current optimisation problem, "Best1Bin" strategy was utilised. In this strategy, two members are randomly chosen from the design space. Their difference is used to mutate the best member. A trial vector is constructed with randomly chosen parameters and with parameters from the best candidate or original candidate. If the trial candidate is better than the original candidate then the trial candidate replaces the original candidate. A similar process

occurs if the trial candidate is better than the best overall candidate, resulting in determining the optimum design candidate in the design space.

### 3.4. RESULTS OF THE OPTIMISATION

This section shows the numerical results of centrifugal compressor optimisation performed at MTT current operating point. The compressor optimisation and MTT compressor performance analysis were performed at International Standard Atmospheric (ISA) conditions. The initial design candidate point assumed for the optimisation process along with their bounds is listed in Table (3.2). Table (2.1) lists the other geometrical parameters used during the optimisation process. The capability of gradient based algorithm in determining the global optimal point for the current optimisation problem was evaluated by comparing the results with stochastic optimisation results. The variation in individual loss components for existing design and optimised design, along with the performance map for the optimised design is presented in this section. Finally, the robustness of the optimisation tool for the wide range of user design static pressure recovery is analysed.

	Value	Lower Bound	Upper Bound
$r_{1,hub}$	4.0 [mm]	0.95	1.3
$\lambda_r$	0.6 [-]	0.95	1.1667
$v_r$	0.525 [-]	0.95	1.1
$\beta_2$	43.0[deg]	0.7	1.375

Table 3.2: Initial Candidate Point along with their Bounds

**Gradient Based Algorithm vs Stochastic Algorithm** The Optimal design vector and the Total-to-Total efficiency achieved using a gradient based algorithm and a stochastic algorithm is listed in Table (3.3). It can be observed that both of these algorithms managed to provide similar optimal design vector except for the  $\beta_2$  design variable. The optimal candidate point provided by stochastic algorithm has lower  $\beta_2$ , resulting in a higher wake-mixing loss at impeller when compared to the optimal candidate point provided by the gradient-based algorithm. The magnitude of other loss components was identical for both the designs.

The gradient based algorithm required only 297 candidate points to determine the optimal compressor design, whereas the stochastic algorithm required 4808 in order to determine the optimal candidate. From these results, it can be inferred that the gradient-based algorithm is better suited for current optimisation problem than the stochastic algorithm. Quoc V. Le [34] came to a similar conclusion while performing optimisation for problems with a relatively small number of design variables. For the remainder of this section, all the results presented were obtained using a gradient-based algorithm.

	Stochastic Algorithm	Gradient Based Algorithm	Units
$r_{1,hub}$	0.00382	0.0038	[m]
$\lambda_r$	0.695	0.70	[-]
$v_r$	0.575	0.578	[-]
$\beta_2$	44.6	45.6	[deg]
$\eta_{TT}$	83.7	83.9	[%]

Table 3.3: Optimal Candidate Point for Stochastic Algorithm and Gradient Based Algorithm

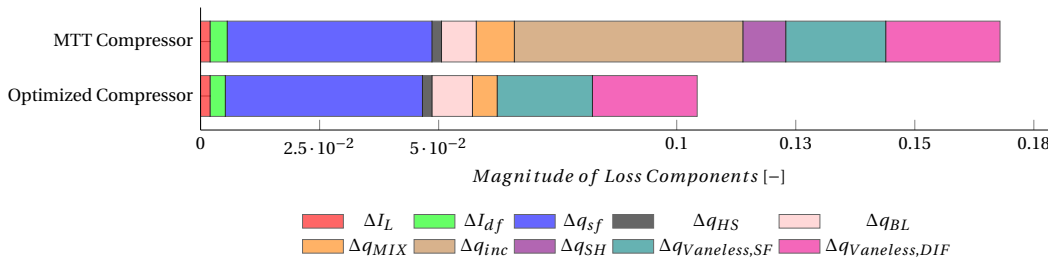


Figure 3.2: Variation in Different Loss Components for MTT Compressor and Optimized Compressor with Vaneless Diffuser

**Optimization of Compressor with Vaneless Diffuser** Figure (3.2) shows the variation in loss components between MTT compressor design and optimised compressor design. It can be observed that the magnitude of incidence; shock; and wake mixing loss component for MTT compressor design is significantly higher when compared to the optimised design. The magnitudes of other loss components were almost identical for both the designs. The meridional shape of MTT impeller and the optimised impeller is shown in Figure (3.3). Figure (3.4) compares the  $\eta_{TT}$  and  $\Pi_{TT}$  of MTT compressor with the optimised compressor. It can be observed that  $\approx 11\%$  increase in Total-to-Total efficiency can be achieved by replacing current MTT compressor with the optimised compressor. The total-to-total pressure ratio of the optimised compressor is  $\approx 4.8\%$  higher when compared to MTT existing compressor design. From the compressor's  $\eta_{TT}$  and CHP units'  $\eta_{el}$  relation discussed in Chapter (1), we can conclude that replacing the MTT compressor with the optimised compressor for MTT CHP unit will result in increasing the electrical efficiency of the CHP system by  $\approx 4.5\%$ .

Figure (3.5) shows the performance map of the optimized compressor. It can be observed that the current operating point (COP) lies on the high-efficiency region and far away from the surge region, thus achieving the objective of the optimisation process.

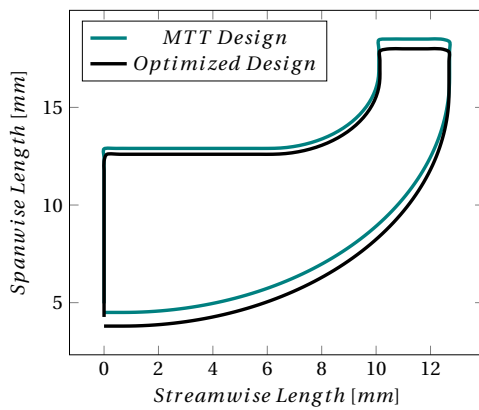


Figure 3.3: Meridional Shape of MTT Impeller and Optimized Impeller

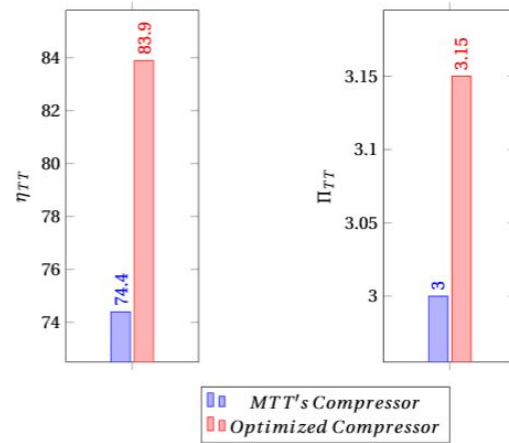


Figure 3.4: Comparison of  $\eta_{TT}$  and  $\Pi_{TT}$  between MTT Compressor and Optimized Compressor

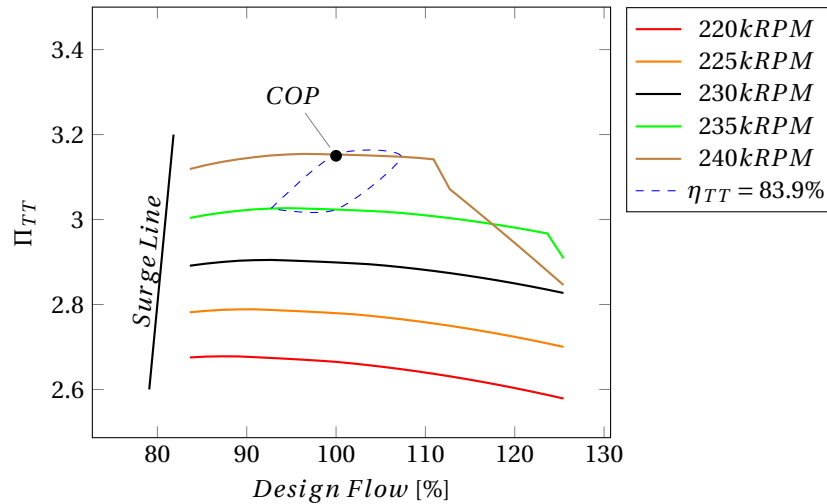


Figure 3.5: Optimised Compressor's Performance Map

**Optimization of Compressor with Vaned Diffuser** In this paragraph the performance of the Optimized compressor with a Vaned Diffuser (OCVD) will be compared with the performance of the Optimized Compressor with a Vane-Less Diffuser (OCVLD). Figure (3.6) summarizes the variation in magnitude of different

loss components for OCVD and OCVLD. Table (3.4) shows the initial and optimal candidate point for vaned diffuser optimization. It can be observed that the optimal of OCVD is similar to OCVLD except for the difference in blade back sweep angle. A scant reduction in losses in vaned diffuser assisted OCVD design to achieve same  $\Pi_{TT}$  with higher  $\beta_2$  angle when compared to OCVLD design. This resulted in reduced wake-mixing loss at impeller exit as shown in Figure (3.6). Figure (3.7) illustrates the variation in  $\Pi_{TT}$  and  $\eta_{TT}$  for OCVLD and OCVD. It can be observed that about 0.6% increase in efficiency can be achieved by replacing the OCVLD design with OCVD design.

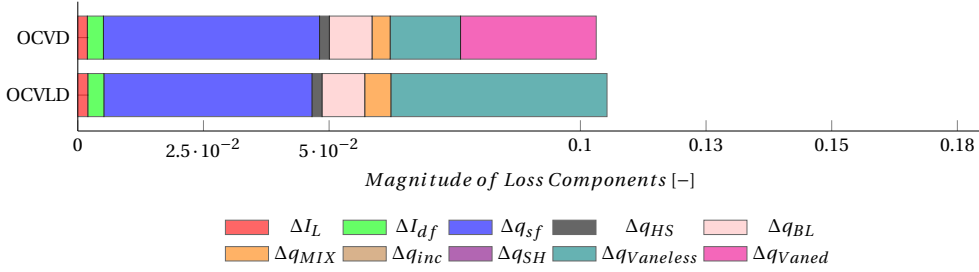


Figure 3.6: Variation in Different Loss Components for Optimized Compressor with Vaned Diffuser (OCVD) and Optimized Compressor with vane-Less Diffuser (OCVLD)

	Initial Candidate Point	Optimum Candidate Point	Units
$r_{1,hub}$	0.004	0.0038	[mm]
$\lambda_r$	0.6	0.7	[-]
$v_r$	0.525	0.578	[-]
$\beta_2$	43.0	49.22	[deg]
<i>Vaneless Space Ratio</i>	1.10	1.25	[-]
$\theta_c$	5.0	5.5	[deg]

Table 3.4: Initial and Optimal Candidate Point for compressor with vaned diffuser

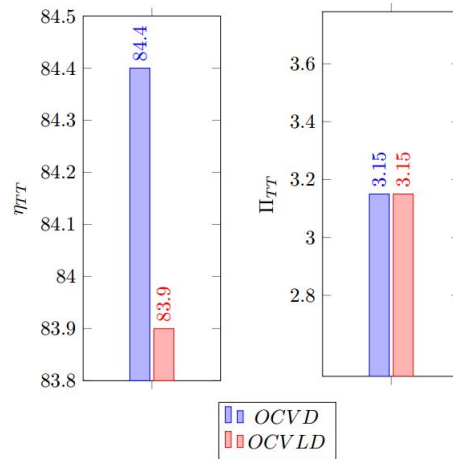


Figure 3.7: Variation in  $\eta_{TT}$  and  $\Pi_{TT}$  for OCVD and OCVLD Design



# 4

## 3D NUMERICAL ASSESSMENT OF THE COMPRESSOR WITH VANELESS DIFFUSER

*The flow properties within a centrifugal compressor can be evaluated using a three-dimensional Computational Fluid Dynamics (CFD) at a higher level than the one-dimensional mean-line analysis. This chapter presents the 3D CFD analysis of MTT compressor with and without pre-whirl. The 3D CFD analysis results were also compared with 1D mean-line analysis results to determine the accuracy of the one-dimensional performance prediction tool. Finally, the 3D CFD analysis of Optimised Compressor with vaneless Design (OCVLD) is presented in this Chapter.*

### 4.1. INTRODUCTION

Considerable progress in development and application of computational fluid dynamics (CFD) for turbomachinery applications has been made in recent years. Present day design process is incomplete without CFD. CFD numerically solves Navier-Stokes equation for applications involving fluid flow, heat transfer and other related phenomena by means of computer-based algorithms.

As described in Chapter (2), flow field within a centrifugal compressor is very complex and turbulent. Turbulence can be characterised as three-dimensional random fluctuations in the flow with velocity gradients existing in all three directions. Turbulence exhibits diffusive and dissipative properties. Diffusion leads to rapid mixing, whereas dissipation leads to increase in fluid's internal energy due to viscous shearing and vortex shedding. In addition, turbulent flows have a wide range of length scales.

The computational efforts required to solve all the turbulent length scales is far beyond present capabilities and for engineering purposes the mean properties of the turbulent flow are sufficiently enough. This gave rise to Reynolds-averaged Navier-Stokes (RANS) equation. In the Reynolds-averaged approach to turbulence, all the unsteadiness is averaged out [35]. However, this approach leads to a closure problem which is solved using empirical approximations i.e., Turbulence Models. The methodology followed during 3D CFD analysis, choice of turbulence model and 3D CFD results will be discussed in upcoming sections of this Chapter.

Table 4.1: Geometrical Parameter of MTT Compressor

Parameters	Value	Units
$r_{1,hub}$	4.5	[mm]
$r_{1,shroud}$	12.9	[mm]
$r_2$	18.5	[mm]
$r_3$	32.73	[mm]
$b_2$	2.6	[mm]
$b_3$	2.6	[mm]
$t$	0.5	[mm]

## 4.2. MODELLING OF COMPUTATIONAL DOMAIN

In order to perform an extensive 3D CFD analysis, various pre-processing steps like geometry creation, grid processing and solver setup has to be performed. This section presents all the pre-processing steps required to perform a 3D CFD analysis for MTT Centrifugal Compressor.

### 4.2.1. GEOMETRY

The geometry for the impeller and diffuser was designed using Ansys BladeGen. The geometrical dimensions (Table 4.1) were provided by MTT. Figure (4.1) and (4.2) shows the geometry of MTT impeller and MTT diffuser used to perform 3D CFD analysis. The thickness of the blades were kept constant along span-wise and stream-wise direction. Blades were designed with elliptical leading edge to resemble the actual shape of MTT impeller.

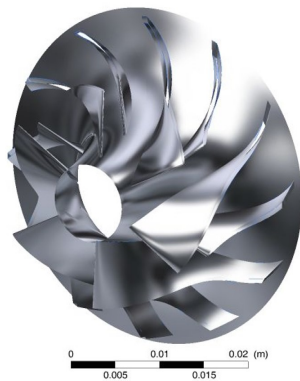


Figure 4.1: MTT Impeller



Figure 4.2: MTT Vaneless Diffuser

**Computational Fluid Domain** The computational fluid domain consists of an inlet duct, impeller and vaneless diffuser with interfaces between the stationary and rotating components, as shown in Figure (4.3). Due to the periodicity of the impeller, it was sufficient to model a full blade and a splitter blade to perform 3D CFD analysis. Table (4.2) lists the inlet and outlet boundary conditions used for CFD simulations.

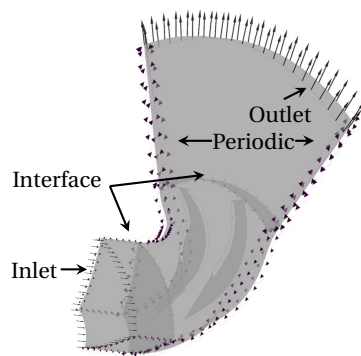


Figure 4.3: Computational Domain

Table 4.2: Boundary Conditions used to Evaluate the Performance of MTT Compressor

Parameters	Value	Units
Inlet Total Pressure	0.98	[bar]
Inlet Total Temperature	296.4	[K]
Inlet x Velocity Component	0.0	[-]
Inlet y Velocity Component	0.0	[-]
Inlet z Velocity Component	0.0	[-]
Exit Mass Flow Rate	0.055	[kg/s]
RPM	240k	[-]

### 4.2.2. GRID GENERATION

Ansys TurboGrid was utilized to generate a 3D structured grid using the H-Grid and C-Grid topologies. C-Grid topology assists in creating fine mesh around the blade. Conformal mesh was created across the interfaces to reduce the computational efforts [13]. Figure (4.4) and (4.5) shows the computational domain with structured mesh along the impeller and C-Grid around the leading edge of the impeller respectively. In order to resolve the viscous sublayer in the boundary layer the non-dimensional wall distance  $Y^+$  was maintained close to 1.

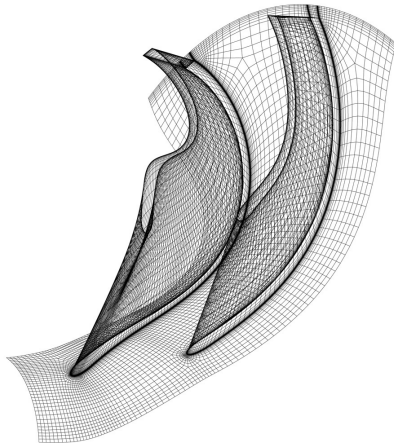


Figure 4.4: MTT Impeller with C-Grid and H-Grid Topology

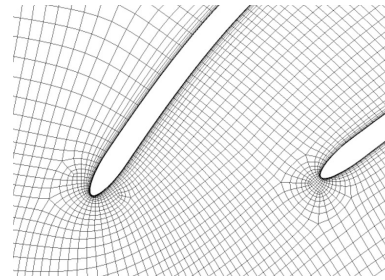


Figure 4.5: MTT Impeller Leading Edge with C-Grid Topology

### 4.2.3. NUMERICAL SOLVER

Commercial tool Ansys CFX 17.1 was utilized to perform the 3D CFD simulations. The discretised conservation equations were resolved using high resolution advection scheme. High resolution velocity pressure coupling algorithm was used to evaluate the mass flow rate. As discussed earlier, the turbulence models were developed based on empirical relations, thus a most suitable turbulence model representing the flow properties for the application has to be chosen. The two-equation models  $k-\epsilon$  and  $k-\omega$  are the widely used turbulence models. The  $k-\epsilon$  turbulence model has been very successful in a large variety of different flow situations, but it has a number of well known shortcomings. From the standpoint of compressor aerodynamics, its lack of sensitivity to adverse pressure gradient is quite disturbing. The  $k-\omega$  turbulence model yields more accurate results for boundary layers even with adverse pressure gradient; and for simulations with separated flows. Sensitivity to free stream boundary conditions is a major drawback for  $k-\omega$  model.

In order to overcome the shortcomings of the mentioned two equation turbulence models, Florian R. Menter developed a new version of  $k-\omega$  turbulence model named as Shear Stress Transport Model (SST). It was observed that SST model showed great agreement with experimental results for flow with adverse pressure gradient and was also independent of free stream values [36]. Bourgeois [37] performed an extensive research in evaluating various turbulence models for centrifugal compressor applications. He found that SST turbulence model was particularly appealing and showed satisfying results over the whole speed-line. Therefore for this thesis, The RANS  $k-\omega$  SST turbulence model was utilized to perform the 3D CFD analysis.

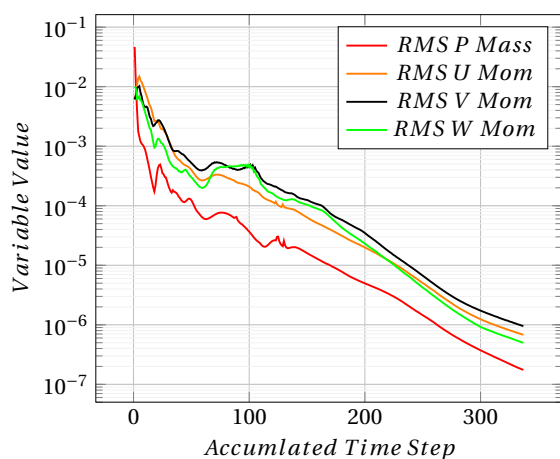
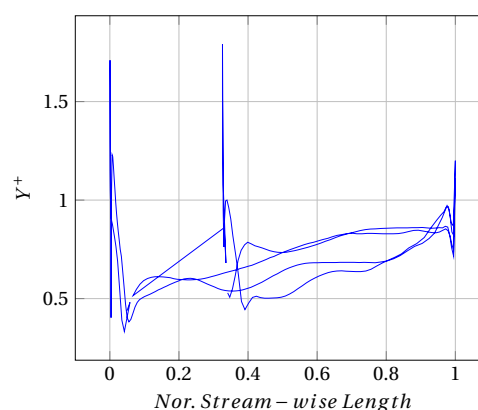


Figure 4.6: RMS Residuals trend for Mass and Momentum observed during 3D CFD analysis of MTT compressor

Figure 4.7: Variation of  $Y^+$  along the Normalised Stream-wise Length of the Impeller Blade [Both Full and Splitter]

The convergence criteria, where the RMS residuals reach below  $1e^{-6}$  was utilized. Figure (4.6) shows the trend of RMS mass and momentum residuals obtained while simulating MTT compressor without pre-whirl,

similar trend was observed for all the results presented in this chapter.

#### 4.2.4. GRID SENSITIVITY ANALYSIS

A numerical method is said to be convergent in terms of mesh resolution if the solution of the discretized equations tends to the exact solution of the differential equation as the grid spacing tends to zero [35]. Five different grid sizes varying from 0.15 million to 0.88 million were evaluated to achieve grid convergence. The  $Y^+ \approx 1$  was maintained for grid size above 0.475 million. The variation of  $Y^+$  along the length of the blade is shown in Figure (4.7). The variation of  $\Pi_{TT}$  and  $\eta_{TT}$  for various grid size is shown in Figure (4.8) and (4.9) respectively. It was observed that the variation in  $\Pi_{TT}$  and  $\eta_{TT}$  for grid size above 0.475 million is 0.14% and 0.02% respectively. Thus a grid size ranging from 0.475 million up to 0.5 million and  $Y^+ \approx 1$  was utilised for all the simulations presented in this chapter.

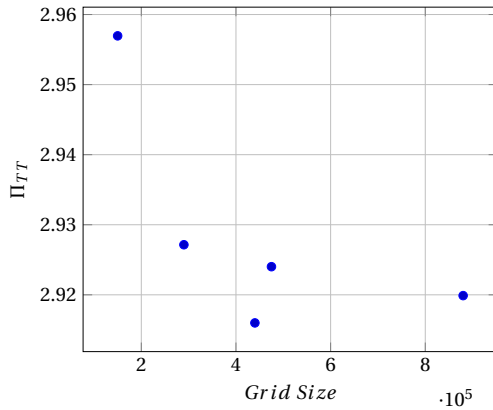


Figure 4.8: Variation in  $\Pi_{TT}$  with respect to Grid Size for MTT Compressor

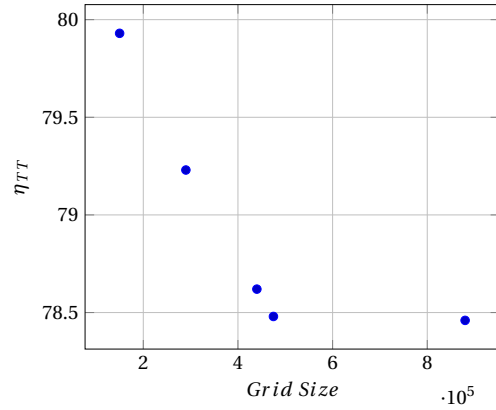


Figure 4.9: Variation in  $\eta_{TT}$  with respect to Grid Size for MTT Compressor

### 4.3. RESULTS

Initially, the flow behaviour within MTT compressor is presented followed with the performance of MTT compressor with positive pre-whirl at the compressor inlet. Then the three-dimensional CFD results are compared with one-dimensional and experimental results to evaluate the prediction accuracy of the 1D and 3D CFD analysis. Finally, the 3D CFD results of optimised compressor design (OCVLD) and its performance with existing MTT scroll are discussed.

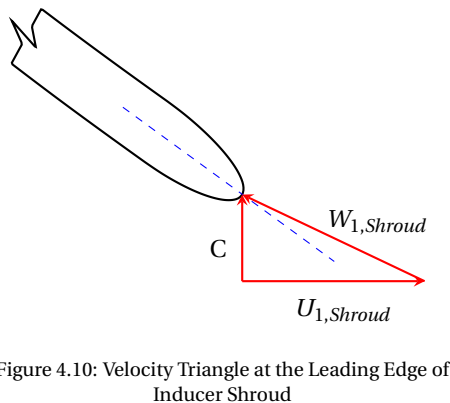


Figure 4.10: Velocity Triangle at the Leading Edge of Inducer Shroud

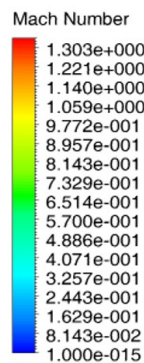


Figure 4.11: Blade-to-Blade Relative Mach Number contour of MTT Impeller near Shroud

**MTT Compressor without pre-whirl** The boundary conditions used for the analysis is listed in the Table (4.2). The mediocre performance of MTT compressor was attributed to the incidence at the leading edge of the inducer by one-dimensional performance prediction tool. The results from 3D CFD analysis were no different. Figure (4.10) shows the difference in relative flow angle and the blade angle at the inducer inlet shroud. The incidence at the leading edge of the inducer leads to rapid acceleration of the flow resulting in flow separation at shock foot as shown in Figure (4.11).

In order to reduce the incidence and rapid flow acceleration at the inducer inlet, a positive pre-whirl is necessary as discussed in Chapter (2). The performance of MTT compressor with pre-whirl is evaluated using 3D CFD techniques and the results are presented in next paragraph.

**MTT Compressor with Pre-Whirl** 3D CFD analysis was performed for MTT compressor with three different positive pre-whirl angles 14 [deg], 20 [deg] and 25 [deg]. Significant reduction in shock strength was observed by varying the positive pre-whirl angle from 14 [deg] to 25 [deg] as shown in Figure (4.12).

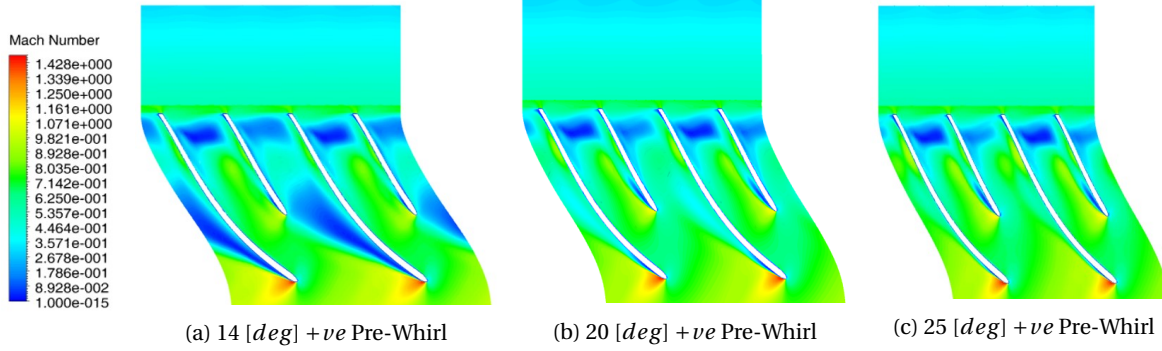


Figure 4.12: Blade-to-Blade Relative Mach Number contour for MTT Compressor near Shroud for different Positive Pre-whirl Angles at Inlet

$\approx 5\%$  increase in compressors  $\eta_{TT}$  was achieved by providing a positive pre-whirl of 25 [deg] at the compressor inlet. However, the  $\Pi_{TT}$  across the compressor was reduced by  $\approx 2.5\%$ . A similar trend in variation of  $\eta_{TT}$  and  $\Pi_{TT}$  was predicted by one-dimensional performance prediction tool.

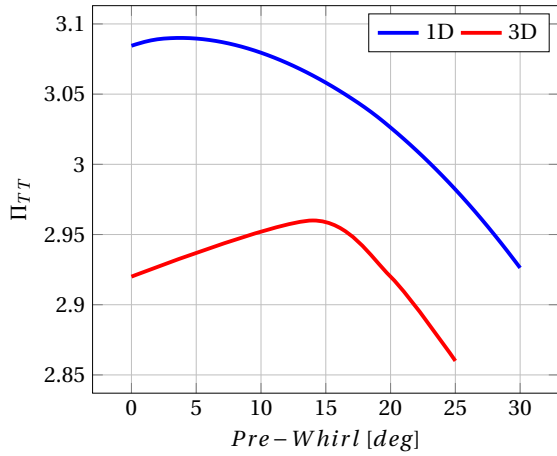


Figure 4.13: Variation in Total-to-Total Pressure Ratio of MTT Compressor with Positive Pre-Whirl at 240k RPM

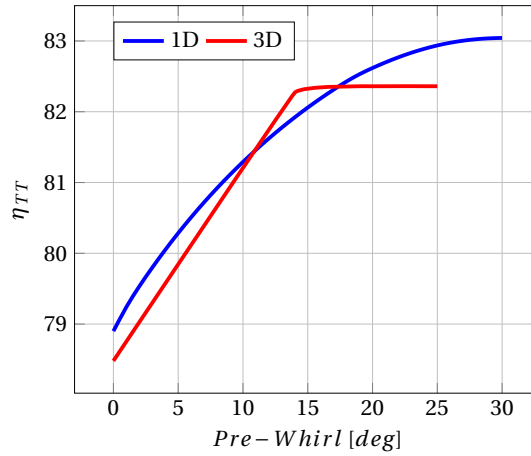


Figure 4.14: Variation in Total-to-Total Efficiency of MTT Compressor with Positive Pre-Whirl at 240k RPM

The variation in  $\eta_{TT}$  and  $\Pi_{TT}$  predicted by 1D and 3D analysis for MTT compressor with different positive pre-whirl at impeller inlet is shown in Figure (4.13) and (4.14) respectively. It can be observed that the  $\eta_{TT}$  predicted by the 1D model is in close agreement with the 3D results up to a pre-whirl of 14[deg]. Beyond 14[deg], the  $\eta_{TT}$  predicted by 3D analysis is almost constant, whereas 1D model showed gradual increase up to 25[deg]. Nevertheless, the increase in  $\Delta\eta_{TT}$  of the compressor with and without pre-whirl predicted using 1D and 3D analysis is almost constant. The maximum offset in the prediction of  $\eta_{TT}$  between 1D and 3D analysis was just 0.7%.

There is a significant difference in prediction of  $\Pi_{TT}$  by 1D model and 3D analysis. It can be observed that the 1D model predicts a slight increase in  $\Pi_{TT}$  from 0 deg up to 4 deg of pre-whirl followed with a gradual and steep descend. Whereas the 3D model predicts a steep increase in  $\Pi_{TT}$  from 0 deg up to 14 deg of pre-whirl followed with steep descend. The primary reason behind the increase in  $\Pi_{TT}$  with pre-whirl is due to the fact

that the rate of reduction of loss components is higher when compared to the rate of reduction of work input. The maximum difference in prediction of  $\Pi_{TT}$  between 1D model and 3D analysis is  $\approx 5\%$ . Over prediction of losses due to shock by SST turbulence model is a possible reason for the difference in prediction of  $\Pi_{TT}$  between 1D and 3D analysis.

**Validation of 1D and 3D results with Experimental Data** Figure (4.15) and (4.16) compares the  $\Pi_{TT}$  and  $T_{03}$  predicted by 1D and 3D analysis with experimental results. The boundary conditions at which the analysis were performed is shown in Table (4.3). It is important to mention that the experimental data has been obtained for the complete compressor, whereas the 1D analysis and 3D analysis comprises of the impeller and the diffuser only. The volute has not been modelled for 1D and 3D analysis. This is one of the primary reasons for variation in prediction of  $\Pi_{TT}$  and  $T_{03}$  by 1D and 3D analysis when compared to the experimental results.

Table 4.3: Boundary Conditions used during 1D, 3D and Experimental Analysis to determine MTT Compressor's Performance

Parameters	0 [deg] Pre-Whirl	14 [deg] Pre-Whirl	Units
Inlet Total Pressure	0.98	1.017	[bar]
Inlet Total Temperature	296.4	303	[K]
Inlet X Component	0.0	0.0	[-]
Inlet y Component	0.0	0.2419	[-]
Inlet z Component	0.0	0.9703	[-]
Exit Mass Flow Rate	0.055	0.055	[kg/s]
RPM	240k	240k	[-]

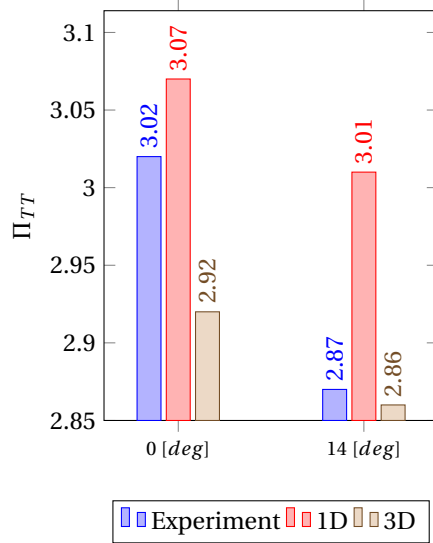


Figure 4.15: Comparison of the Total-to-Total Pressure Ratio between Experimental, 1D and 3D Results at 240k rpm for MTT Compressor with and without Pre-Whirl

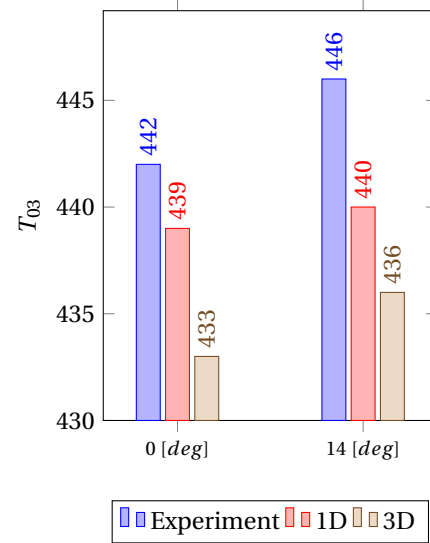


Figure 4.16: Comparison of the Exit Total-to-Total Temperature between Experimental, 1D and 3D Results at 240k rpm for MTT Compressor with and without Pre-Whirl

Other possible reasons for difference in 3D CFD analysis and experimental results are the numerical errors and the steady-state simulation with the SST turbulence model. Nevertheless, it can be observed that the maximum difference in prediction of  $\Pi_{TT}$  and  $T_{03}$  by 3D analysis is  $\approx 3\%$  and  $\approx 2\%$  respectively, when compared to experimental results.

**Optimized Compressor with Vaneless Diffuser (OCVLD)** The optimized compressor with vaneless diffuser design (OCVLD) obtained from 1D optimization tool is evaluated using 3D CFD analysis. Default values suggested by Ansys BladeGen was utilized for all the unknown geometrical parameters. Figure (4.17) compares the shape of optimized full and splitter blade with existing MTT design.

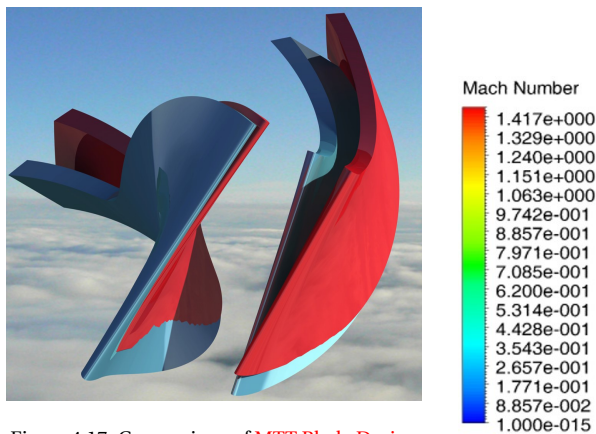


Figure 4.17: Comparison of MTT Blade Design with Optimized Blade Design

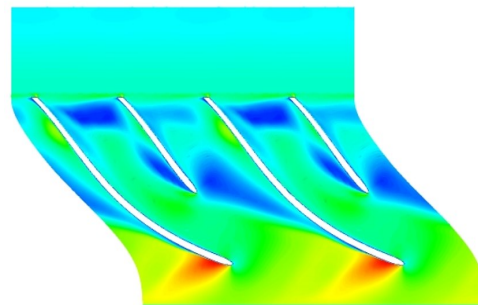


Figure 4.18: Blade-to-Blade Relative Mach Number Contour of Optimized Impeller near Shroud

The boundary conditions used to analyse MTT compressor without pre-whirl was utilized for analysing the optimized compressor design. Figure (4.18) shows the blade-to-blade relative mach number variation near the shroud for the optimized compressor design. It can be observed that the wake region has been significantly reduced for optimized compressor when compared to the existing MTT compressor. The optimized compressor has a weak shock followed by a separation bubble. Further refinement in meridional shape and impeller blade shape is necessary to enhance the performance. Nevertheless, the optimized compressor showed 5% increase in  $\eta_{TT}$  when compared to the MTT compressor for the same  $\Pi_{TT}$ . MTT needs to redesign the existing compressor scroll to accommodate the optimized impeller, because the shroud radius of the optimized impeller is 0.3 mm shorter than the existing impeller design.

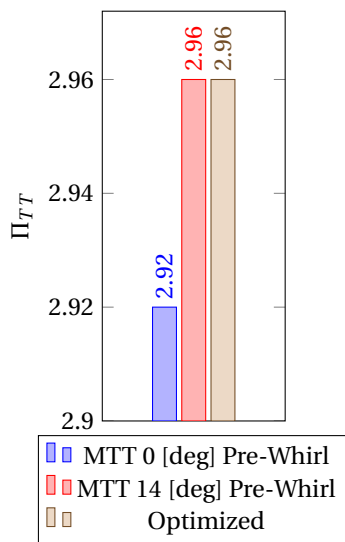


Figure 4.19: Comparison of  $\Pi_{TT}$  between MTT Compressor without Pre-whirl, MTT Compressor with Pre-Whirl and Optimized Compressor

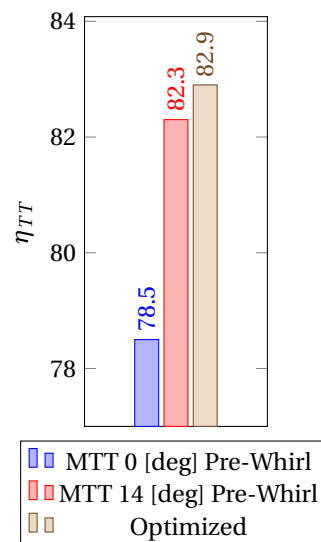


Figure 4.20: Comparison of  $\eta_{TT}$  between MTT Compressor without Pre-whirl, MTT Compressor with Pre-Whirl and Optimized Compressor

The  $\Pi_{TT}$  and  $\eta_{TT}$  of the MTT compressor with and without pre-whirl and of the optimized compressor obtained using 3D CFD analysis is shown in Figure (4.19) and (4.20) respectively. It can be observed that the  $\Pi_{TT}$  and  $\eta_{TT}$  of the MTT compressor with 14 [deg] pre-whirl is approximately equal to the  $\Pi_{TT}$  and  $\eta_{TT}$  of the optimized compressor design. Thus, from above observation we can conclude that the most cost effective option for MTT is to provide a pre-whirl at compressor inlet instead of incorporating the optimized impeller design because incorporating optimized impeller design requires redesign of compressor scroll which is comparatively costlier.



# 5

## DESIGN AND 3D NUMERICAL ASSESSMENT OF COMPRESSOR WITH VANED DIFFUSER

*In this chapter, the influence of the vaned diffuser on the performance of the MTT compressor is determined. Firstly, a brief description of the three main categories of the vaned diffuser along with the important design parameters is presented. The methodology followed during the design and the analysis of the vaned diffuser is described. Finally, the 3D CFD results of the three main categories of the vaned diffuser are presented.*

### 5.1. INTRODUCTION

There are broadly two types of diffusers used for centrifugal compressor namely, Vaneless Diffuser and Vaned Diffuser. Vaneless diffusers are used for applications where maximum operating range and minimum cost are the prime design requirements, whereas vaned diffusers are used for applications where maximum static pressure rise and efficiency are the prime design requirements.

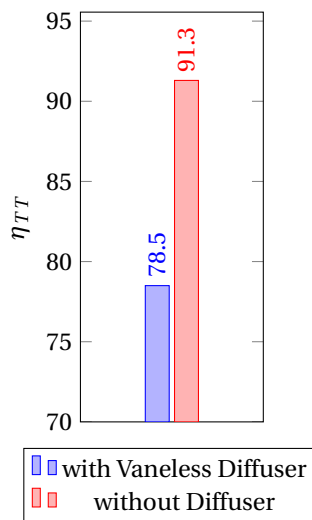


Figure 5.1: Comparison of  $\eta_{TT}$  between MTT Compressor with Vaneless Diffuser and without Diffuser

Figure (5.1) shows the Total-to-Total efficiency of MTT centrifugal compressor with vaneless diffuser and without diffuser obtained using 3D CFD analysis for inlet boundary conditions,  $P_{01} = 0.98$  [bar] and  $T_{01} = 296.4$  [K].  $\approx 60\%$  increase in losses takes place by incorporating a vaneless diffuser as observed in Figure (5.1). Though losses are directly proportional to the amount of deceleration of the fluid, the vaneless diffusion process is generally accepted as less efficient due to increased skin friction loss [19]. The feasibility of enhancing MTT compressor performance at the expense of the operating range is evaluated in this chapter by replacing the vaneless diffuser in the MTT compressor with a vaned diffuser.

The subsequent sections of this chapter address the different types of vaned diffuser followed with their most important design parameters. Subsequently, the methodology followed to design the vaned diffuser for MTT compressor is described. Finally, the methodology and the results of the 3D CFD analysis for MTT centrifugal compressor with a vaned diffuser is presented.

## 5.2. VANED DIFFUSER

The fluid through a vaneless diffuser takes a logarithmic path resulting in high frictional losses. Figure (5.2) shows the flow traces for MTT vaneless diffuser. The flow path across the vaneless diffuser can be reduced at an expense of static delivery pressure by reducing the vaneless diffuser exit radius ( $r_3$ ). However, by providing better guidance to the flow in the diffusing passage using vanes, the length of the flow path can be reduced without reducing the static delivery pressure, resulting in reduced frictional losses. Boyce [30] states that at the design point replacing the vaneless diffuser with a vaned diffuser will assist in increasing the compressor's efficiency by  $\approx 4\%$ . The nomenclature generally used for all types of a vaned diffuser is shown in Figure (5.3).

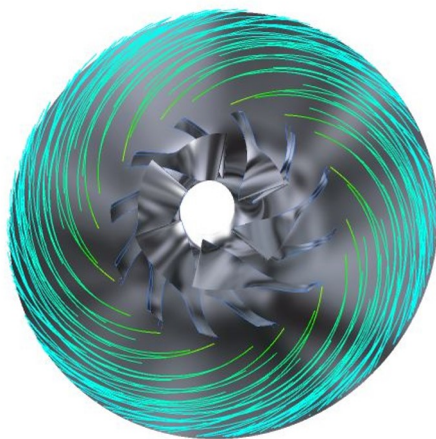


Figure 5.2: Flow Path Traces Across MTT Vaneless Diffuser

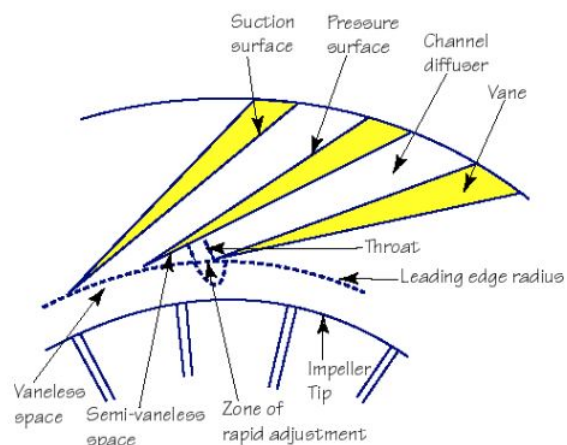


Figure 5.3: The Geometry and Nomenclature of Vaned Diffuser

The vaned diffuser can be classified into three types namely, Channel Diffuser, Airfoil Type Vaned Diffuser and Low-Solidity Vaned Diffuser. The performance and geometrical characteristics of different diffuser categories are summarised in Table (5.1).

**Channel Diffuser (CD)** The channel diffusers are used by a large number of turbomachinery companies due to its low cost and good performance [38] [39]. The starting point for the design of the channel diffuser is often the selection of the geometrical parameter namely divergence angle ( $2\theta_c$ ), the area ratio (AR) and the length-to-width ratio (LWR). Yoshinaga [40] suggested the optimal divergence angle for straight-channel vaned diffuser is in range of 8 to 10 [deg], whereas Aungier [27] suggested the optimal divergence angle must be less than 11 [deg]. Figure (5.3) shows the schematic of channel diffuser.

**Airfoil Shaped Vaned Diffuser (ASVD)** Figure (5.4) shows the MTT compressor with an airfoil shaped vaned diffuser. The airfoil shaped vaned diffuser can provide sufficient pressure rise at a smaller diffuser outer diameter when compared to channel shaped vaned diffuser [19]. However, the curvature of the vanes leads to complex design and increased manufacturing cost when compared to the channel shaped vaned diffuser. The operating range of airfoil shaped vaned diffuser is higher when compared to channel shaped vaned diffuser [41].

**Low Solidity Vaned Diffuser (LSVD)** In low solidity vaned diffuser the vanes are positioned far apart to purposely avoid the existence of throat. Solidity is defined as the ratio of vane chord to vane pitch. The performance and operating range of LSVD are in between vaneless diffuser and airfoil or channel type diffuser. Figure (5.5) shows the MTT compressor with LSVD.

Table 5.1: Performance and Geometrical Characteristics of Different Diffuser Categories

Diffuser Types	Operating Range	Cost	Efficiency	Static Pressure Rise	Diffuser Exit Radius
Vaneless	High	Low	Moderate	Low	High
Channel Diffuser	Low	Moderate	High	High	Low
ASVD	Low	High	Very High	High	Very Low
LSVD	Moderate	High	Moderate	Moderate	Moderate



Figure 5.4: MTT Impeller with 13 Vanes Airfoil Shaped Vaned Diffuser



Figure 5.5: MTT Impeller with 20 Vanes Airfoil Shaped Low-Solidity Vaned Diffuser

### 5.3. VANED DIFFUSER DESIGN PARAMETERS

Regardless of the type of vaned diffuser, nine geometrical parameters play a significant role in determining the performance of the vaned diffuser. They are vaneless space ratio, throat blockage, incidence angle, vane leading edge shape, vane number, divergence angle, length-to-width ratio, area ratio, and vane profile. The throat area for the MTT compressor is calculated using one-dimensional performance prediction tool. The area ratio and the length-to-width ratio is suggested by one-dimensional performance prediction tool for the user defined static delivery pressure. As these three geometrical parameters are constant for MTT compressor, their influence on the performance of vaned diffuser will not be addressed in this section. The essential features of all the other geometrical parameter along with their values for MTT compressor is described in this section.

**Divergence Angle** The significance of divergence angle on performance of channel diffuser was evaluated by many researchers [42] [43][44]. Their common conclusion was that having a small divergence angle ( $2\theta_c$ ) resulted in reduced static pressure recovery due to blockage. Clements [45] observed that increasing the channel diffuser with divergence angle of  $2\theta_c = 12$  produced 4% higher pressure recovery coefficient when compared to channel diffuser with divergence angle of  $2\theta_c = 4$ . Aungier [27] observed abrupt deterioration in channel diffuser performance for  $2\theta_c > 11$ .

On the contrary, the one-dimensional tool discussed in Chapter (2) predicted better performance for divergence angle ( $2\theta_c$ ) above 11 [deg]. Therefore, for MTT compressor with channel diffuser the divergence angle was varied from 11 [deg] to 21 [deg] and its performance is evaluated using 3D CFD analysis.

**Vaneless Space Ratio** The flow unsteadiness at the exit of the impeller is reduced across the vaneless space due to better mixing of circumferential distortions. The vaneless space ratio usually varies from 1.05 to 1.25. Decreasing the vaneless space ratio beyond 1.05 will result in increased vibration and noise levels [19].

Rogers [38] evaluated the performance of the centrifugal compressor with channel diffuser for four different vaneless space ratio namely 1.035, 1.125, 1.180 and 1.215. He observed that maximum compressor effi-

ciency was achieved with a vaneless space ratio of 1.125. The losses within the diffuser apparently increased when the vaneless space ratio departed from optimum value of 1.125.

Ziegler [46] studied the impeller-diffuser interaction for different vaneless space ratios through laser-2-focus velocimeter measurements. He varied the vaneless space ratio from 1.04 to 1.18 for two different vane setting angles. He observed that the total pressure loss is two points better for vaneless space ratio of 1.04 when compared to 1.18. He recommended using small vaneless space ratio for applications with narrow operating range [47].

Figure (5.6) shows the variation in Total-to-Total efficiency of MTT Compressor with channel diffuser for different channel numbers and vaneless space ratios using one-dimensional performance prediction tool for inlet conditions  $P_{01} = 0.98$  [bar] and  $T_{01} = 296.4$  [K]. It can be observed that the maximum efficiency is achieved at vaneless space ratio of 1.10 for a channel diffuser with 20 vanes and divergence angle of 22 [deg]. Reducing the vaneless space ratio below 1.10 is geometrically infeasible for MTT compressor. For channel diffusers with a divergence angle of 11 [deg] and the number of vanes greater than 11, the influence of vaneless space ratio on performance is negligible.

Therefore, from above observations, a vaneless space ratio of 1.10 was utilised for designing MTT vaned diffuser.

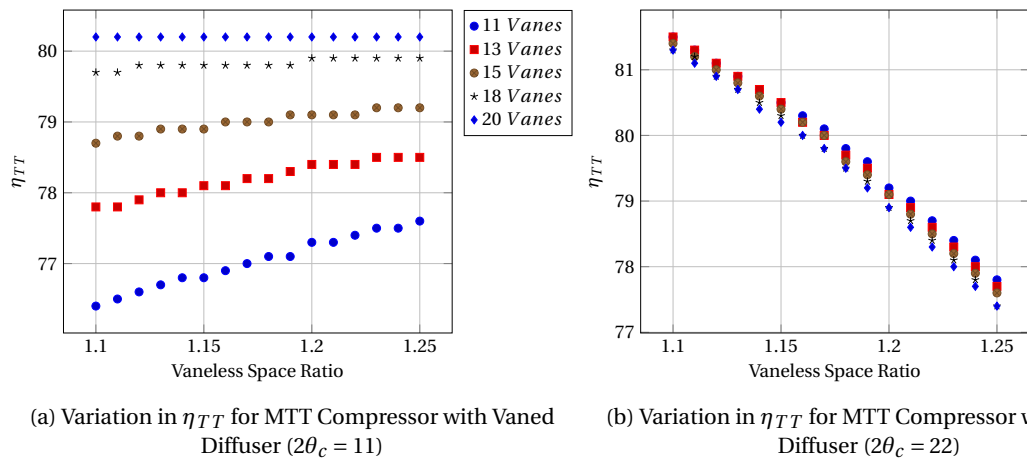


Figure 5.6: Variation in  $\eta_{TT}$  for MTT Compressor with Vaned Diffuser Analyzed using One-Dimensional Performance Prediction Tool

**Vane Number** The vane numbers or channel numbers ( $Z_D$ ) play a predominant role in determining the diffuser size and efficiency. Large vane numbers assist in gradual diffusion, however, the losses due to skin friction and blockage may overcome the advantages of gradual diffusion. Boyce [30] suggested that the number of vanes should be less than the number of impeller blades ( $Z_I$ ) to avoid the possibility of vane channel getting blocked by impeller wake. The preferred choice of Aungier [27] was  $Z_D = Z_I \pm 1$  and satisfying the criterion  $10 \leq Z_D \leq 20$ . Rodgers [38] evaluated the performance of vaned diffuser for different vane number while keeping the throat area constant. He observed that the number of vanes did not affect the performance of the vaned diffuser as long as the throat area was kept constant.

The throat area for MTT vaned diffuser is calculated using one-dimensional performance prediction tool as explained in Chapter (2). Since the throat is situated at the inlet of a channel, the number of vanes within a channel diffuser can be modified without varying the throat area. The performance of MTT compressor with a channel diffuser was evaluated for two different vane numbers 13 and 20. The choice of the vane numbers was motivated from the observation of Aungier and Figure (5.6). The same number of vanes were utilised to evaluate the performance of MTT compressor with an LSVD using 3D CFD techniques. In the case of an airfoil shaped vaned diffuser, the number of vanes is fixed for a given airfoil profile, vaneless space ratio and throat area.

**Vane Profile** Dean [14] and Rodgers [38] observed that the vane profile had negligible difference in vaned diffuser performance. However, Kmecl [48] [49] and Smith [50] proved that using proper aerodynamic profile assisted in increasing the performance of the vaned diffuser. For MTT compressor, the performance of the channel diffuser and the airfoil shaped vaned diffuser is evaluated using 3D CFD techniques.

**Vane Leading Edge Shape** Casartelli [51] modified the leading edge shape of a circular arc vaned diffuser and performed numerical and experimental analysis to evaluate its performance. He observed that the vane with elliptical leading edge performed better when compared to the vane with a semi-circular leading edge. Bammert [52] observed that staggering the vanes from hub to shroud (i.e., twisted vane) resulted in increasing the operating range of the vaned diffuser along with its performance.

For MTT compressor, the performance of channel diffuser with a semi-circular leading edge is evaluated using 3D CFD analysis. The performance of MTT compressor with an elliptical leading edge is not evaluated due to its lower operating range. The performance of MTT compressor with twisted vanes is not evaluated in this thesis.

**Incidence Angle** The vane leading edge incidence angle is an important parameter governing the performance of the vaned diffuser. Rodgers observed a very small change in channel diffuser performance for the incidence of  $+5 [deg]$ . Boyce [30] suggested that the diffuser vane should be set at an incidence angle of  $-4 [deg]$  to accommodate the variations in fluid angle at the leading edge of the vane.

Though MTT compressor operates at constant RPM and mass flow rate, the variation in inlet conditions alters the vaned diffuser inlet flow angle. The absolute flow angle at the inlet of vaned diffuser for inlet conditions  $P_{01} = 0.8 [bar]$  and  $T_{01} = 263 [K]$  is  $\approx 60 [deg]$ , whereas for  $P_{01} = 1.1 [bar]$ ,  $T_{01} = 313 [K]$  is  $\approx 66 [deg]$ . Figure (5.7) shows the variation in vaned diffuser inlet flow angles for both the cases. In order to accommodate the inlet flow angle variations an airfoil with blunt leading edge (NACA 23012) was selected as the vane profile for airfoil shaped vaned diffuser and LSVD.

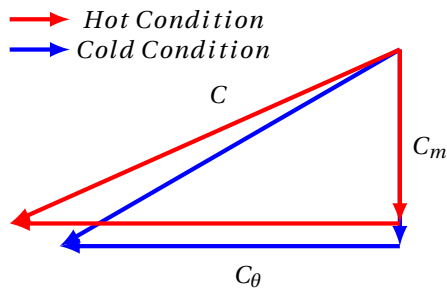


Figure 5.7: Variation in Velocity Triangle at Vaned Diffuser Inlet for Two Different Inlet Conditions



Figure 5.8: MTT Impeller with 20 Vanes Channel Diffuser

## 5.4. NUMERICAL MODEL

In order to perform an extensive 3D CFD analysis, various pre-processing steps like geometry creation, grid processing and solver setup has to be performed. This section presents all the pre-processing steps required to perform a 3D CFD analysis for MTT Centrifugal Compressor with a vaned diffuser.

### 5.4.1. GEOMETRY

The geometry for the impeller and diffuser was designed using Ansys BladeGen. The geometrical dimensions (Table 4.1) were provided by MTT. CATIA V5 was utilised to create the geometry of the vaned diffuser. Figure (5.8), (5.4) and (5.5) shows the geometry of channel diffuser, airfoil shaped vaned diffuser and LSVD designed for MTT compressor. The various geometrical parameters utilized to design the vaned diffuser is shown in Table (5.2).

Table 5.2: Geometrical Parameter of MTT Vaned Diffuser

Parameters	CD	ASVD	LSVD	Units
Vaneless Space Ratio	1.10	1.10	1.10	[-]
Number of Vanes, ( $Z_D$ )	13,20	13	13,20	[-]
Incidence Angle	0.0	0.0	0.0	[-]
Throat Area	173	173	NA	[ $mm^2$ ]
Area Ratio	0.6	0.6	0.6	[-]
Divergence Angle, ( $2\theta_c$ )	11, 15, 18, 21	NA	NA	[deg]

#### 5.4.2. GRID GENERATION

Ansys ICEM CFD meshing tool was utilised to create a structured grid using H-Grid, O-Grid and C-Grid topologies. Figure (5.9) and (5.10) shows the grid along the vanes of a channel and an airfoil shaped vaned diffuser respectively. As similar blocking strategy was utilised for all the vaned diffuser designs, mesh sensitivity analysis was not performed. The non-dimensional wall distance,  $Y^+$  was maintained below 5, the equiangle skewness was maintained below 0.75 and the 3x3x3 determinant was maintained above 0.75 for all the results presented in this chapter.

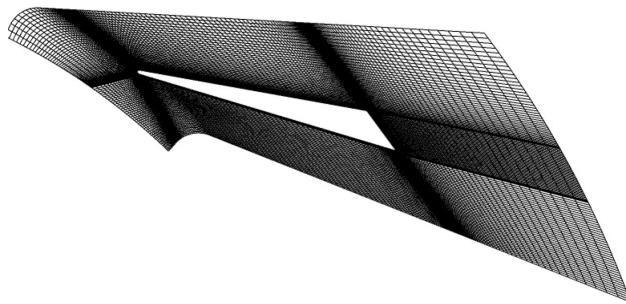


Figure 5.9: Grid Along Channel Diffuser for MTT Compressor

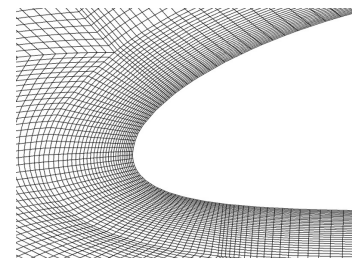


Figure 5.10: Grid Along the Leading Edge of Airfoil Shaped Vaned Diffuser

#### 5.4.3. SOLVER

Commercial tool Ansys CFX 17.1 was utilised to perform the 3D CFD simulations for MTT Compressor with Vaned Diffuser. As described in Chapter (4), RANS  $k-\omega$  SST turbulence model was utilized to perform the 3D CFD analysis. The convergence criteria, where the RMS residuals reach below  $1e^{-5}$  was utilised.

### 5.5. RESULTS

3D CFD analysis for MTT compressor with different vaned diffuser designs was performed for inlet boundary conditions,  $P_{01} = 0.98$  [bar] and  $T_{01} = 296.4$  [K]. Initially, The performance of MTT compressor with three different types of the vaned diffuser is presented in this section. Followed, The 1D analysis results for channel diffuser is validated against 3D CFD results to determine the prediction accuracy of the 1D model. Finally, the performance of the vaned diffuser with positive pre-whirl at compressor inlet is shown.

#### 5.5.1. CHANNEL SHAPE VANED DIFFUSER

The performance of MTT compressor with five different configurations of channel diffuser was analysed using 3D CFD analysis. The five configuration can be categorised using two geometrical parameters namely divergence angle and vane number.

**Constant Divergence Angle** The performance of channel diffuser for two different vane number at constant divergence angle ( $2\theta_c = 11$  [deg]) was evaluated. Figure (5.11) and (5.12) shows the Mach number contour for channel diffuser with 13 vanes and 20 vanes respectively. It can be observed that increasing the vane numbers reduces the wake region at an expense of increased skin friction.

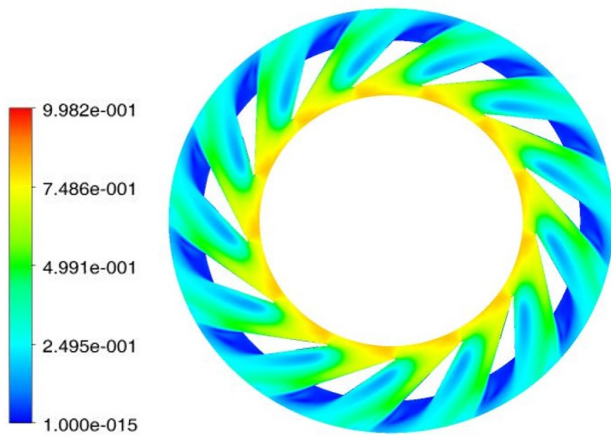


Figure 5.11: Mach Number Contour Across 13 Vane Channel Diffuser with Divergence Angle of 11 [deg] at Mid-Span

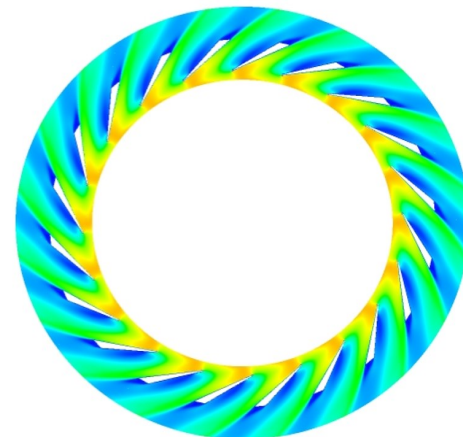


Figure 5.12: Mach Number Contour Across 20 Vane Channel Diffuser with Divergence Angle of 11 [deg] at Mid-Span

**Constant Vane Number** The performance of the 13 vane channel diffuser with four different divergence angle namely 11, 15, 18 and 21 [deg] was evaluated using 3D CFD analysis. Figure (5.11), (5.13), (5.14) and (5.15) shows the Mach number contours at mid-span along the vanes with divergence angle of 11, 15, 18 and 22 [deg] respectively. It can be observed that the increase in divergence angle reduces the wake region at the trailing edge of the vane but leads to flow separation along the vane's pressure side.

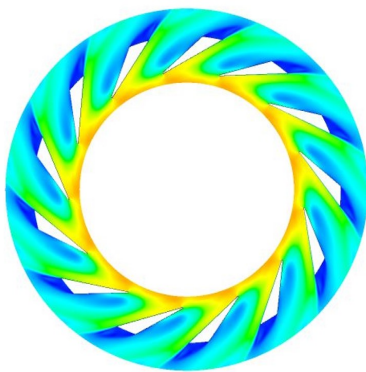


Figure 5.13: Mach Number Contour at Mid-Span Across 13 Vanes Channel Diffuser with divergence angle of 15 [deg]

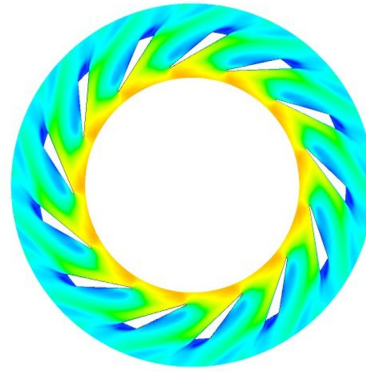


Figure 5.14: Mach Number Contour at Mid-Span Across 13 Vanes Channel Diffuser with divergence angle of 18 [deg]

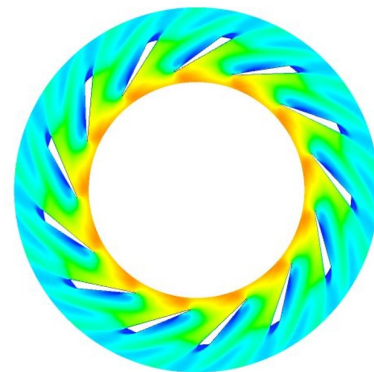


Figure 5.15: Mach Number Contour at Mid-Span Across 13 Vanes Channel Diffuser with divergence angle of 21 [deg]

Figure (5.16) shows the  $\eta_{TT}$  of MTT compressor with five different channel diffuser designs. It can be observed that the 13 vanes channel diffuser with a divergence angle of 11 [deg] performance better when compared to all the other variants.

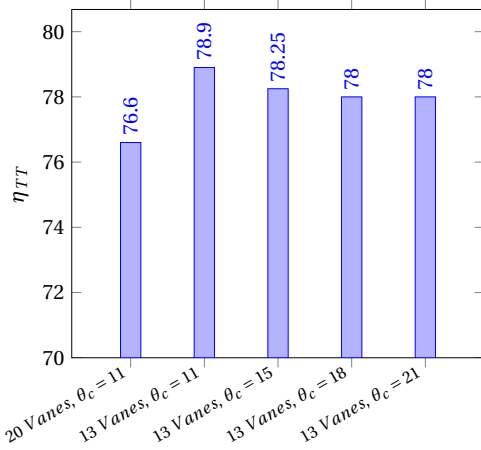


Figure 5.16: Performance of MTT Compressor for Five Different Channel Diffuser Configurations

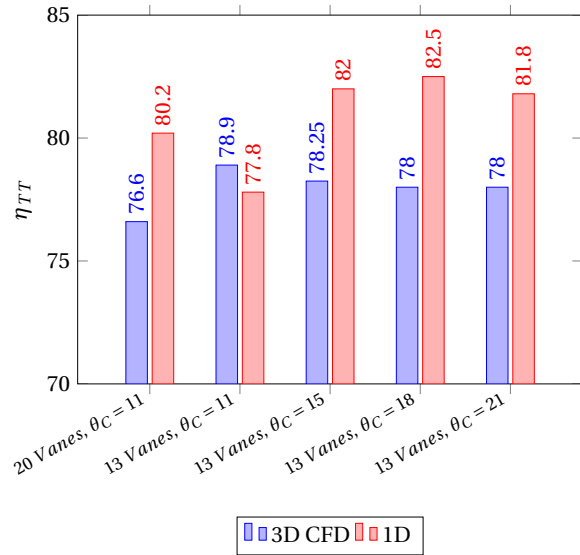


Figure 5.17: Performance of MTT Compressor for Five Different Channel Diffuser Configurations

**Validation of 1D results with 3D CFD results** Figure (5.17) compares the  $\eta_{TT}$  of MTT compressor with vaned diffuser predicted using one-dimensional performance prediction tool and 3D CFD analysis. It can be observed that for cases with flow separation along the channel, the performance prediction of the 1D tool is inaccurate when compared to 3D CFD results. The possible reason for the difference in results of 1D analysis and 3D CFD analysis is the incapability of the 1D model to evaluate losses due to the boundary layer separation. The maximum difference in  $\eta_{TT}$  predicted using 1D analysis and 3D CFD results is  $\approx 5\%$ .

### 5.5.2. AIRFOIL SHAPED VANED DIFFUSER

As discussed in Section (5.3), an airfoil with blunt leading edge was selected to accommodate the variation in the inlet flow angle at the vaned diffuser inlet for different operating conditions. Figure (5.18) shows the Mach number contour of the airfoil shaped vaned diffuser at the mid-span. It can be observed that the region of wake has been reduced comprehensively for airfoil shaped vaned diffuser when compared to channel diffuser. Figure (5.19), compares the  $\eta$  of MTT compressor with channel diffuser and MTT compressor with an airfoil shaped vaned diffuser. It can be observed that  $\approx 1\%$  increase in  $\eta_{TT}$  can be achieved by replacing the channel diffuser with an airfoil shaped vaned diffuser for MTT compressor.

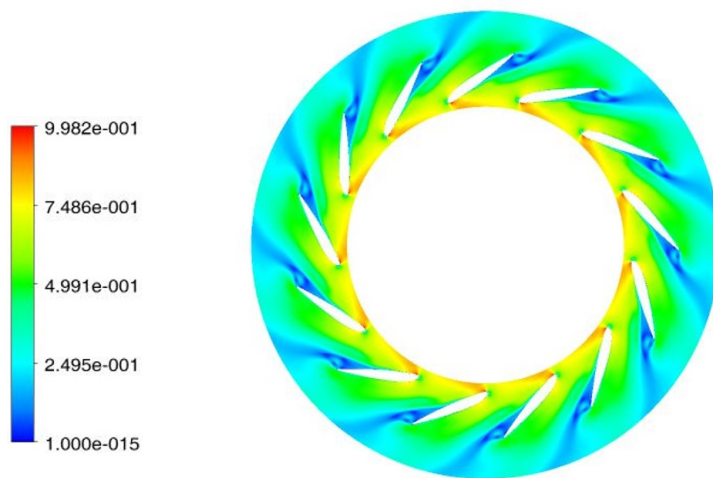


Figure 5.18: Mach Number Contour Across 13 Vane Channel Diffuser at Mid-Span

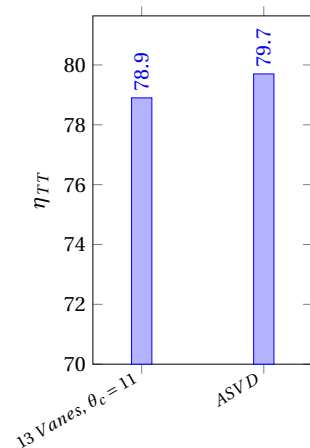


Figure 5.19: Comparison of MTT Compressor Performance with Channel Diffuser and with Airfoil Shaped Vaned Diffuser

### 5.5.3. LOW SOLIDITY AIRFOIL SHAPED VANED DIFFUSER (LSVD)

Figure (5.20) and (5.21) shows the Mach number contour for airfoil shaped low solidity vaned diffuser at the mid-span. It can be observed that the region of the wake is lower for 13 vanes LSVD when compared to 20 vanes LSVD. As the distance travelled by the flow across the low solidity vaned diffuser is comprehensively lower when compared to a vaneless diffuser, the performance of the compressor is increased as shown in Figure (5.22). However, for the LSVD with 20 vanes, the advantages due to the shorter flow path is alleviated by the losses due to the skin friction from vanes resulting in poor performance. As discussed in Section (5.2), the performance of the 13 vanes LSVD is between the vaneless diffuser and the 13 vanes ASVD.

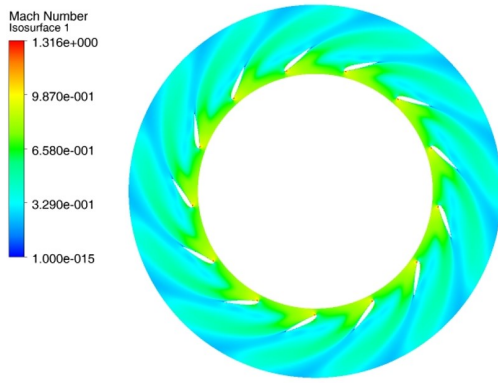


Figure 5.20: Mach Number Contour Across 13 Airfoil Shaped Low Solidity Vaned Diffuser at Mid-Span

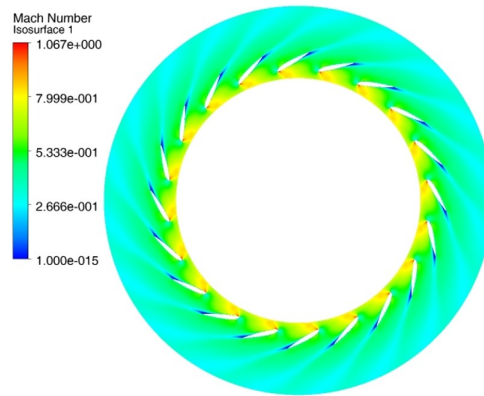


Figure 5.21: Mach Number Contour Across 20 Airfoil Shaped Low Solidity Vaned Diffuser at Mid-Span

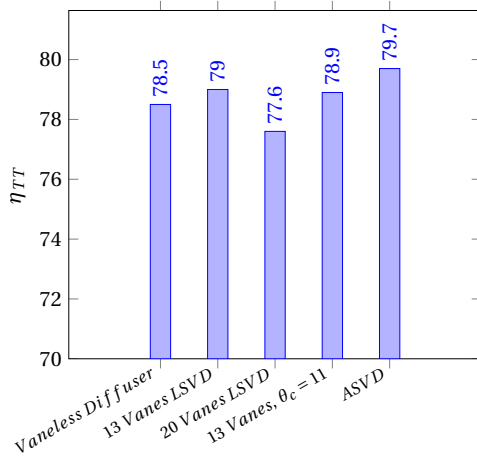


Figure 5.22: Comparison of MTT Compressor's Performance with Different Diffuser Configurations

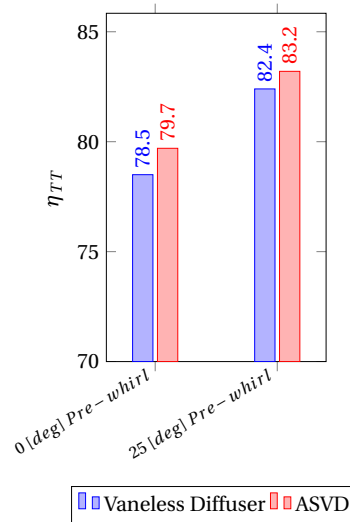


Figure 5.23: Comparison of MTT Compressor's Performance with Vaneless Diffuser and with Airfoil Shaped Vaned Diffuser for 0 [deg] Pre-whirl and 25 [deg] Pre-whirl

### 5.5.4. EFFECT OF PRE-WHIRL ON MTT COMPRESSOR FLUID-DYNAMIC PERFORMANCE

The performance of MTT compressor with vaneless diffuser and with vaned diffuser is finally analysed with and without positive pre-whirl at the compressor inlet. It can be observed that replacing the vaneless diffuser with airfoil shaped vaned diffuser and providing a positive pre-whirl of 25 [deg] at compressor inlet results in increasing the performance of the MTT compressor by  $\approx 5\%$ , as shown in Figure (5.23). From the compressor's  $\eta_{TT}$  and CHP units'  $\eta_{el}$  relation discussed in Chapter (1), the vaneless diffuser with airfoil shaped vaned diffuser and providing a positive pre-whirl of 25 [deg] at compressor inlet results in increasing the electrical efficiency of the MTT CHP system by  $\approx 2.2\%$ .



# 6

## CONCLUSIONS AND RECOMMENDATIONS

Distributed generation (DG) is one of the options for a more efficient and sustainable use of fossil fuels as energy source. Among the various technologies which are currently proposed for DG, micro combined heat and power could play a significant role because of its compact size, a small number of moving parts and lower noise, leading to reduced environmental impacts during energy conversion.

In this study, the recuperated micro gas turbine developed by the Dutch company Micro Turbine Technology B.V. (MTT) has been utilised as an illustrative example. The MTT micro turbine delivers electrical and thermal power output up to 3 and 15 kW, respectively, and will be primarily applied in micro CHP units for domestic dwellings. The MTT micro gas turbine compressor consists of a commercial off-the-shelf automotive turbocharger impeller to reduce manufacturing cost. However, adopting the turbocharger impeller for micro gas turbine applications mostly results in operating the compressor at off-design conditions, thus reducing its performance. A cycle study of the MTT recuperated micro gas turbine has been carried out in order to assess the impact of the centrifugal compressor performance on the system performance. The analysis proved that the system net electrical conversion efficiency can increase by about 0.4% for every 1% increase in the compressor isentropic efficiency.

In line with the objectives of this research as stated in Chapter 1, the main conclusions of the work presented in this thesis are summarized as follows:

- The incidence at the inlet of the impeller played a significant role in reducing the performance of the MTT compressor. The adoption of turbocharger impeller for MTT compressor was the primary reason for the reduction in MTT compressor performance. However, the losses due to incidence were mitigated at the expense of pressure ratio by providing a positive pre-whirl at the impeller inlet. The losses in MTT compressor was further mitigated by replacing a vaneless diffuser with a vaned diffuser.
- Optimisation of MTT compressor with a vaneless diffuser (OCVLD) was performed to determine the significance of other geometrical parameters on MTT compressor performance. Apart from the blade angle at impeller inlet, radius at inducer hub, radius at inducer tip, radius at impeller tip and the diffuser type also played a substantial role in reducing the performance of the MTT compressor. However, incorporating OCVLD or OCVD designs are not cost effective options for MTT as a new compressor scroll has to be designed to accommodate the optimised impeller.
- Thus, The most cost effective option for the MTT compressor is to incorporate pre-whirl and vaned diffuser with existing turbocharger impeller. Approx. 2.2% increase in electrical efficiency for MTT CHP unit can be achieved by incorporating a positive pre-whirl of 25 [deg] and an airfoil shaped vaned diffuser.

### 6.1. RECOMMENDATIONS

The work described in this thesis left many open issues of interest for future research activities:

- The inlet pipe located upstream of the impeller, as well as the volute, have to be included in the mean-line analysis, in order to achieve a better insight on the flow field and of their mutual influence.

- The performance prediction of MTT compressor with a vaned diffuser at vane divergence angle ( $\theta_c$ ) above 5.5 [deg] is not satisfactory. The primary reason for the poor prediction is the incapability of the meanline model to evaluate losses due to flow separation within the vane channel. Thus, modeling flow separation loss across vane channel at higher vane divergence angle is necessary to increase the prediction accuracy of the 1D meanline tool.
- Unsteady CFD investigations of the best-vaned diffuser can be performed to analyze the impeller-vaned diffuser interaction.
- A "multi-point" vane shape optimisation has to be carried out in order to optimise the vaned diffuser for a wider range of operating conditions.

## BIBLIOGRAPHY

- [1] E. Eurostat, *Energy, transport and environment indicators-2016 edition*, (2016).
- [2] E. E. Directive, *Directive 2012/27/eu of the european parliament and of the council of 25 october 2012 on energy efficiency, amending directives 2009/125/ec and 2010/30/eu and repealing directives 2004/8/ec and 2006/32*, Official Journal, L **315**, 1 (2012).
- [3] P. Fraser, *Distributed generation in liberalised electricity markets*, in *International symposium on distributed generation: power system and market aspects* (2002) pp. 1G–12.
- [4] M. Olivero, *Evolution of a centrifugal compressor: From turbocharger to micro gas turbine applications* (Doctoral Thesis, Technical University of Delft, Netherlands, 2012).
- [5] N. Strachan and A. Farrell, *Emissions from distributed vs. centralized generation: The importance of system performance*, Energy Policy **34**, 2677 (2006).
- [6] E. Directive, *8/EC. The promotion of cogeneration based on a useful heat demand in the internal energy market*, Tech. Rep. (Directive 2004/8/EC of 11 February 2004 from the European Parliament and of the Council, and amending Directive 92/42/EC. L 52/50 Official Journal of the European Union EN, 21 February, 2004).
- [7] R. Lee, *Combined heat and power in a carbon-constrained world*, Proceedings of the Institution of Civil Engineers-Energy **163**, 31 (2010).
- [8] R. Beith, *Small and micro combined heat and power (CHP) systems: advanced design, performance, materials and applications* (Elsevier, 2011).
- [9] S. M. C. Ang, *Model-based design and operation of fuel cell systems*, Ph.D. thesis, UCL (University College London) (2012).
- [10] A. F. El-Sayed, *Aircraft propulsion and gas turbine engines* (CRC Press, 2008).
- [11] W. Visser, S. Shakariyants, M. De Later, A. H. Ayed, and K. Kusterer, *Performance optimization of a 3kw microturbine for chp applications*, in *ASME Turbo Expo 2012: Turbine Technical Conference and Exposition* (American Society of Mechanical Engineers, 2012) pp. 619–628.
- [12] W. Visser, S. Shakariyants, and M. Oostveen, *Development of a 3 kw microturbine for chp applications*, Journal of Engineering for Gas Turbines and Power **133**, 042301 (2011).
- [13] A. Javed, *Developing Generic Design Expertise for Gas Turbine Engines: Robust Design of a Micro Centrifugal Compressor*, Ph.D. thesis, TU Delft, Delft University of Technology (2014).
- [14] R. Dean, *On the unresolved fluid dynamics of the centrifugal compressor*, Advanced Centrifugal Compressors , 1 (1971).
- [15] D. Eckardt, *Flow field analysis of radial and backswept centrifugal compressor impellers. i-flow measurements using a laser velocimeter*, in *Performance Prediction of Centrifugal Pumps and Compressors* (1979) pp. 77–86.
- [16] B. Lakshminarayana, *Turbine cooling and heat transfer*, Fluid Dynamics and Heat Transfer of Turbomachinery , 597 (1996).
- [17] D. Eckardt, *Detailed flow investigations within a high-speed centrifugal compressor impeller*, Journal of Fluids Engineering **98**, 390 (1976).

- [18] M. Johnson and J. Moore, *The influence of flow rate on the wake in a centrifugal impeller*, in *ASME 1982 International Gas Turbine Conference and Exhibit* (American Society of Mechanical Engineers, 1982) pp. V001T01A018–V001T01A018.
- [19] N. A. Cumpsty, *Compressor aerodynamics* (Longman Scientific & Technical, 1989).
- [20] C. Rodgers, *Static pressure recovery characteristics of some radial vaneless diffusers*, *Canadian aeronautics and space journal* **30**, 42 (1984).
- [21] E. Morishita, *Centrifugal compressor diffusers*, (1982).
- [22] W. Stiefel, *Experiences in the development of radial compressors*, *Advanced radial compressors* (1972).
- [23] R. H. Aungier, *Mean streamline aerodynamic performance analysis of centrifugal compressors*, *TRANSACTIONS-AMERICAN SOCIETY OF MECHANICAL ENGINEERS JOURNAL OF TURBOMACHINERY* **117**, 360 (1995).
- [24] D. Sturge and N. Cumpsty, *Two-dimensional method for calculating separated flow in a centrifugal impeller*, *Journal of Fluids Engineering* **97**, 581 (1975).
- [25] J. W. Daily and R. E. Nece, *Chamber dimension effects on induced flow and frictional resistance of enclosed rotating disks*, *ASME J. basic eng* **82**, 217 (1960).
- [26] R. Nece and J. Daily, *Roughness effects on frictional resistance of enclosed rotating disks*, *Journal of Basic Engineering* **82**, 553 (1960).
- [27] R. H. Aungier, *Centrifugal compressors: a strategy for aerodynamic design and analysis* (American Society of Mechanical Engineers, 2000).
- [28] S. Lieblein, *Loss and stall analysis in compressor cascades*, (1959).
- [29] X. Gong and R. Chen, *Total pressure loss mechanism of centrifugal compressors*, *Mechanical engineering research* **4**, 45 (2014).
- [30] M. P. Boyce, *Centrifugal compressors: a basic guide* (PennWell Books, 2003).
- [31] M. Casey and D. Rusch, *The matching of a vaned diffuser with a radial compressor impeller and its effect on the stage performance*, *Journal of Turbomachinery* **136**, 121004 (2014).
- [32] A. Konak, D. W. Coit, and A. E. Smith, *Multi-objective optimization using genetic algorithms: A tutorial*, *Reliability Engineering & System Safety* **91**, 992 (2006).
- [33] A. Whitfield and N. C. Baines, *Design of radial turbomachines*, (1990).
- [34] J. Ngiam, A. Coates, A. Lahiri, B. Prochnow, Q. V. Le, and A. Y. Ng, *On optimization methods for deep learning*, in *Proceedings of the 28th International Conference on Machine Learning (ICML-11)* (2011) pp. 265–272.
- [35] J. H. Ferziger, M. Peric, and A. Leonard, *Computational methods for fluid dynamics*, (1997).
- [36] F. R. Menter, *Two-equation eddy-viscosity turbulence models for engineering applications*, *AIAA journal* **32**, 1598 (1994).
- [37] J. A. Bourgeois, R. J. Martinuzzi, E. Savory, C. Zhang, and D. A. Roberts, *Assessment of turbulence model predictions for an aero-engine centrifugal compressor*, *Journal of Turbomachinery* **133**, 011025 (2011).
- [38] C. Rodgers, *The performance of centrifugal compressor channel diffusers*, in *ASME 1982 International Gas Turbine Conference and Exhibit* (American Society of Mechanical Engineers, 1982) pp. V001T01A003–V001T01A003.
- [39] F. Kano, N. Tazawa, and Y. Fukao, *Aerodynamic performance of large centrifugal compressors*, in *ASME 1982 International Gas Turbine Conference and Exhibit* (American Society of Mechanical Engineers, 1982) pp. V001T01A009–V001T01A009.

- [40] H. Mishina, F. Koseki, and H. Nishida, *Aerodynamic performance of a centrifugal compressor with vaned diffusers*, *Journal of Fluids Engineering* **102**, 487 (1980).
- [41] S. Deniz, E. M. Greitzer, and N. A. Cumpsty, *Effects of inlet flow field conditions on the performance of centrifugal compressor diffusers: Part 2—straight-channel diffuser*, in *ASME 1998 International Gas Turbine and Aeroengine Congress and Exhibition* (American Society of Mechanical Engineers, 1998) pp. V001T01A112–V001T01A112.
- [42] J. Carlson, J. Johnston, and C. Sagi, *Effects of wall shape on flow regimes and performance in straight 2-dimensional diffusers*, *JOURNAL OF BASIC ENGINEERING* **89**, 151 (1967).
- [43] S. J. Kline, D. E. Abbott, and R. W. Fox, *Optimum design of straight walled diffusers* (Department of Mechanical Engineering, Stanford University, 1958).
- [44] P. Runstadler Jr and F. Dolan, *Further data on the pressure recovery performance of straight-channel, plane-divergence diffusers at high subsonic Mach numbers*, *Journal of Fluids Engineering*, 373 (1973).
- [45] W. Clements and D. Artt, *The influence of diffuser channel geometry on the flow range and efficiency of a centrifugal compressor*, *Proceedings of the Institution of Mechanical Engineers, Part A: Power and Process Engineering* **201**, 145 (1987).
- [46] K. U. Ziegler, H. E. Gallus, and R. Niehuis, *A study on impeller-diffuser interaction: part i—influence on the performance*, in *ASME Turbo Expo 2002: Power for Land, Sea, and Air* (American Society of Mechanical Engineers, 2002) pp. 545–556.
- [47] K. U. Ziegler, H. E. Gallus, and R. Niehuis, *A study on impeller-diffuser interaction: part ii—detailed flow analysis*, in *ASME Turbo Expo 2002: Power for Land, Sea, and Air* (American Society of Mechanical Engineers, 2002) pp. 557–568.
- [48] T. Kmecl and P. Dalbert, *Optimization of a vaned diffuser geometry for radial compressors: Part i—investigation of the influence of geometry parameters on performance of a diffuser*, in *ASME 1999 International Gas Turbine and Aeroengine Congress and Exhibition* (American Society of Mechanical Engineers, 1999) pp. V001T03A064–V001T03A064.
- [49] T. Kmecl, R. ter Harkel, and P. Dalbert, *Optimization of a vaned diffuser geometry for radial compressors: Part ii—optimization of a diffuser vane profile in low solidity diffusers*, in *ASME 1999 International Gas Turbine and Aeroengine Congress and Exhibition* (American Society of Mechanical Engineers, 1999) pp. V001T03A061–V001T03A061.
- [50] V. Smith, *A review of design practice and technology of radial compressor diffusers*, in *MECHANICAL ENGINEERING*, Vol. 92 (ASME-AMER SOC MECHANICAL ENG 345 E 47TH ST, NEW YORK, NY 10017, 1970) p. 61.
- [51] E. Casartelli, A. Saxer, and G. Gyarmathy, *Numerical flow analysis in a subsonic vaned radial diffuser with leading edge redesign*, in *ASME 1997 International Gas Turbine and Aeroengine Congress and Exhibition* (American Society of Mechanical Engineers, 1997) pp. V001T03A035–V001T03A035.
- [52] K. Bammert, M. Jansen, and M. Rautenberg, *On the influence of the diffuser inlet shape on the performance of a centrifugal compressor stage*, in *ASME 1983 International Gas Turbine Conference and Exhibit* (American Society of Mechanical Engineers, 1983) pp. V001T01A005–V001T01A005.